

**THE EVOLUTION OF TOTAL LIGHTNING AND RADAR
REFLECTIVITY CHARACTERISTICS OF TWO MESOSCALE
CONVECTIVE SYSTEMS OVER HOUSTON, TEXAS**

A Thesis

by

CHARLES LEE HODAPP

Submitted to the Office of Graduate Studies of
Texas A&M University
in partial fulfillment of the requirements for the degree of

MASTER OF SCIENCE

December 2007

Major Subject: Atmospheric Sciences

**THE EVOLUTION OF TOTAL LIGHTNING AND RADAR
REFLECTIVITY CHARACTERISTICS OF TWO MESOSCALE
CONVECTIVE SYSTEMS OVER HOUSTON, TEXAS**

A Thesis

by

CHARLES LEE HODAPP

Submitted to the Office of Graduate Studies of
Texas A&M University
in partial fulfillment of the requirements for the degree of

MASTER OF SCIENCE

Approved by:

Chair of Committee,	Larry D. Carey
Committee Members,	Richard E. Orville Courtney Schumacher Hongxing Liu
Head of Department,	Richard E. Orville

December 2007

Major Subject: Atmospheric Sciences

ABSTRACT

The Evolution of Total Lightning and Radar Reflectivity Characteristics of Two Mesoscale Convective Systems over Houston, Texas. (December 2007)

Charles Lee Hodapp, B.S., Texas A&M University

Chair of Advisory Committee: Dr. Larry Carey

Two mesoscale convective systems (MCSs) passed over the Houston Lightning Detection and Ranging (LDAR) network on 31 October 2005 and 21 April 2006. As the MCSs traverse the LDAR network, the systems slowly mature with a weakening convective line and a developing stratiform region and radar bright band. The intensification of stratiform region precipitation, including the bright band, is thought to play an important role in stratiform lightning structure, charge structure, and total lightning production of MCSs. The stratiform areas quadruple in size and the mean reflectivity values increase substantially by ~ 6 dB. As the stratiform region matures, VHF source density plots show a lightning pathway that slopes rearward and downward from the back of the convective line and into the stratiform region. At early times for both MCSs, the pathway extends horizontally rearward 40 to 50 km into the stratiform region at an altitude of 9 to 12 km. Near the end of the analysis time period, the pathway slopes rearward 40 km and downward through the transition zone before extending 40 to 50 km in the stratiform region at an altitude of 4 - 7 km. The sloping pathway likely results from charged ice particles advected from the convective line by storm relative

front-to-rear flow while the level pathway extending further into the stratiform region is likely caused by both charge advection and local in-situ charging.

As the stratiform region matures, the stratiform flash rates double and lightning heights decrease. The percentage of lightning flashes originating in the stratiform region increases significantly from 10 - 20% to 50 - 60%. Overall, the number of positive cloud-to-ground flashes in the stratiform region also increases. Between both MCSs, 60% of the positive CGs originated in the convective or transition regions. Both in-situ charging mechanisms created by the development of the mesoscale updraft and charge advection by the front-to-rear flow likely contribute to the increased electrification and lightning in the stratiform region.

ACKNOWLEDGEMENTS

I would like to thank Dr. Larry Carey, Dr. Richard Orville, Dr. Courtney Schumacher, and Dr. Hongxing Liu for being on my advisory committee and their availability and assistance. My deepest gratitude is extended to Dr. Carey. His continuous guidance, support, and expertise helped make this thesis possible. I would also like to thank all my co-workers. Special thanks to Brandon Ely, Veronica McNear, and Shane Motley for their programming assistance and also Nathan Clements, Chris McKinney, and Amber Reynolds for their collaborative efforts. I also gratefully acknowledge that the scientific research and operation of the Houston LDAR II network is supported by the National Science Foundation (ATM-0442011 and ATM-0321052). In addition I would like to thank the generosity of the airports, school districts, and colleges around Houston who have donated land use, electricity, and Internet connections to enable the real-time operation of the lightning network. To all my friends and family who have always been there for me, thank you!

TABLE OF CONTENTS

	Page
ABSTRACT	iii
ACKNOWLEDGEMENTS	v
TABLE OF CONTENTS	vi
LIST OF FIGURES.....	viii
LIST OF TABLES	xiv
1. INTRODUCTION.....	1
1.1 Lightning	1
1.1.1 Thunderstorm Electrification	2
1.1.1.1 Inductive Charging Mechanism	2
1.1.1.2 Non-Inductive Charging Mechanisms	5
1.1.1.3 Other Charging Mechanisms.....	9
1.1.2 Thunderstorm Charge Structure	10
1.1.2.1 The Lightning Flash	11
1.2 Mesoscale Convective Systems (MCSs).....	14
1.2.1 Organizational Modes	15
1.2.2 Kinematic and Microphysical Processes of MCSs	19
1.3 Electrical Properties of MCSs	23
1.3.1 MCS Charge Structure	23
1.3.2 MCS Lightning.....	29
1.4 Objective	33
2. DATA AND METHODOLOGY	35
2.1 Radar Data.....	35
2.1.1 Radar Reflectivity	36
2.1.2 Analysis Techniques	38
2.1.2.1 Partitioning the Data.....	39
2.1.2.2 Contoured Frequency by Altitude Diagrams (CFADs).....	41
2.1.2.3 Rainfall Totals	42
2.2 Lightning Detection and Ranging Network	44
2.2.1 VHF Source Density Plots	46
2.2.2 Flash Algorithm.....	48
2.3 National Lightning Detection Network.....	50

	Page
3. RESULTS	54
3.1 2005 October 31 LLTS MCS	54
3.1.1 Radar Reflectivity	55
3.1.2 Total Lightning.....	64
3.1.2.1 Lightning Detection and Ranging (LDAR).....	64
3.1.2.2 NLDN.....	75
3.2 2006 April 21 LLTS MCS	84
3.2.1 Radar Reflectivity	85
3.2.2 Total Lightning.....	92
3.2.2.1 Lightning Detection and Ranging (LDAR).....	92
3.2.2.2 National Lightning and Detection Network (NLDN)	99
4. DISCUSSION	110
5. CONCLUSIONS.....	117
REFERENCES.....	120
VITA	128

LIST OF FIGURES

FIGURE	Page
1.1	Depicting selective ion capture of (a) collision between an uncharged water drop polarized in an electric field and a negative ion and (b) deflection of a positive ion from an uncharged polarized drop..... 4
1.2	Induction charging of rebounding particles. 4
1.3	The polarity of charge gained by graupel as a function of temperature and liquid water content for Takahashi (1978) and Saunders et al. (1991) laboratory experiments..... 7
1.4	Depiction of the thunderstorm tripole charge structure 8
1.5	Conceptual model of the storm structure for updraft and non-updraft regions of a convective thunderstorm..... 12
1.6	Diagram showing the various processes involved in a negative CG lightning flash. 14
1.7	Schematic of the evolution of three convective modes seen in PRE-STORM program..... 17
1.8	Idealized depiction of squall line formation..... 17
1.9	Schematic depicting (a) symmetric and (b) asymmetric types of leading line-trailing stratiform MCS precipitation organization (from Houze et al. 1990). 18
1.10	Conceptual model of a mature leading line trailing stratiform MCS viewed in a vertical cross section normal to the convective line..... 20
1.11	A conceptual model of the charge structure of mature leading line trailing stratiform MCSs..... 28

FIGURE	Page
1.12 A 30-min, line-normal vertical composite of radar reflectivity (dBZ, contours every 5 dBZ) and VHF lightning source density ($\text{km}^{-3} \text{h}^{-1}$, shaded as shown) through a mature leading line, trailing stratiform MCS over the DFW region on 16 June 2002 from 0609 to 0639 UTC.	31
1.13 Conceptual model of the kinematic and precipitation structure of a mature leading-line, trailing-stratiform (LLTS) mesoscale convective system (MCS) that is viewed in a vertical cross-section oriented perpendicular to the convective line (i.e., parallel to its motion)(Carey et al. 2005).	32
2.1 WSR 88D volume coverage pattern 21 (VCP 21).	37
2.2 WSR-88D volume coverage pattern 11 (VCP 11).	37
2.3 An example of subjective partitioning of the 21 April 2006 MCS.	42
2.4 The location of a lightning source based on the time of arrival technique.	45
2.5 A network consisting of 3 direction finding sensors determine the location of a lightning strike.	51
3.1 NEXRAD reflectivity images of the 31 October MCS at a) 08:00 UTC, b) 12:00 UTC, c) 16:00 UTC, and d) 20:00 UTC.	54
3.2 Composite reflectivity images for four different times during the lifetime of the 31 October MCS.	56
3.3 Time series plot of the mean reflectivities (dBZ) in three equally sized areas of the stratiform region	57
3.4 Contoured frequency by altitude diagrams (CFADs) and mean profiles of radar reflectivity for the 31 October MCS a) stratiform and b) convective regions for 22:43 UTC (solid) and 23:32 UTC (dashed).	59
3.5 Time series of mean reflectivities at all elevations for the a) stratiform and b) convective regions of the 31 October MCS.	61

FIGURE	Page
3.6 Time series plot of the mean stratiform and convective reflectivities of the 31 October MCS at a height of 4.3 km.	63
3.7 Time series plot of the radar derived rainfall totals that fell under the 31 October MCS convective and stratiform regions during the time span of each volume scan.	64
3.8 VHF source density (color filled) and composite radar reflectivity (contoured) line normal vs. vertical cross-section plots for 4 different times during the evolution of the 31 October 2005 MCS.	65
3.9 Plot of VHF lightning sources (color coded with respect to time) and composite reflectivity associated with a representative flash that occurred on 31 October at 22:38 UTC.	68
3.10 Same as Fig. 3.9 except for a representative flash that originated in the convective region and propagated rearward and downward through the stratiform region.	69
3.11 Time series plot of the 31 October MCS stratiform flash rate during ten minute intervals centered on the radar volume scan times.	71
3.12 Time series plot of the percentage of stratiform flashes originating in the 31 October MCS analysis domain (convective, transition, or stratiform regions).	71
3.13 Time series plot of the mean flash extent for stratiform flashes originating in both the 31 October MCS stratiform and convective regions.	72
3.14 Time series plot of the mean number of VHF sources that compose flashes in both the 31 October stratiform and convective regions.	73
3.15 Time series plot of the mean flash heights of stratiform flashes originating in both the 31 October MCS stratiform and convective regions.	74

FIGURE	Page
3.16 Time series plot of the flash rate and the IC:CG ratio in the 31 October MCS over a ten minute time span centered on the radar volume scan time.....	76
3.17 Time series plot of the CG flash rate and the percent of positive CGs occurring over a ten minute time period in the 31 October MCS stratiform region.	76
3.18 Same as Fig. 3.17 except for in the 31 October convective region.....	77
3.19 Time series plot of the 31 October MCS stratiform and convective CG peak currents.....	77
3.20 Same as Fig. 3.9 except with a +CG flash originating from the convective line at 23:02 UTC.....	82
3.21 Same as Fig. 3.9 except with a + CG flash originating in the stratiform region at 23:42 UTC.....	83
3.22 NEXRAD reflectivity images of the 21 April MCS at a) 06:00 UTC, b) 08:00 UTC, c) 10:00 UTC, and d) 12:00 UTC.....	84
3.23 Composite reflectivity images for four different times during the lifetime of the 21 April MCS.	86
3.24 Contoured frequency by altitude diagrams (CFADs) and mean profiles of radar reflectivity for the 21 April MCS a) stratiform and b) convective regions for 11:09 UTC (solid) and 12:41 UTC (dashed).	87
3.25 Time series of mean reflectivities at all elevations for the 21 April MCS a) stratiform and b) convective regions.....	89
3.26 Time series plot of the mean stratiform and convective reflectivities of the April 21 MCS at a height of 4.3 km.....	91
3.27 Time series plot of the radar derived rain mass that fell under the 21 April MCS convective and stratiform regions during the time span of each volume scan.....	92

FIGURE	Page
3.28 VHF source density (color filled) and composite radar reflectivity (contoured) line normal vs. vertical cross-section plots for 4 different times during the evolution of the 21 April MCS.	93
3.29 Plot of the VHF lightning sources (color coded with respect to time) and composite reflectivity associated with a representative flash that occurred on 21 April at 11:09 UTC.....	95
3.30 Same as Fig. 3.29 except for a representative flash that originated in the convective region and propagated rearward and downward through the stratiform region.....	96
3.31 Time series plot of the 21 April MCS stratiform flash rate occurring over ten minute intervals centered on the radar volume scan times.	98
3.32 Time series plot of the percentage of the 21 April MCS stratiform flashes originating in the analysis domain (convective, transition, or stratiform regions).....	98
3.33 Time series plot of the mean flash extent of stratiform region flashes originating in both the 21 April MCS stratiform and convective regions.....	100
3.34 Time series plot of the mean number of VHF sources that compose stratiform region flashes originating in both the 21 April MCS stratiform and convective regions.	100
3.35 Time series plot of the mean flash heights of stratiform flashes originating in both the 21 April MCS stratiform and convective regions.	101
3.36 Time series plot of the flash rate and the IC:CG ratio in the 21 April MCS stratiform region over a ten minute time span centered on the radar volume scan time.	101
3.37 Time series plot of the CG flash rate and percent of positive CGs occurring over a ten minute time period in the 21 April MCS stratiform region.	103

FIGURE		Page
3.38	Same as Fig. 3.37 except for in the 21 April MCS convective region.....	103
3.39	Time series plot of the mean stratiform and convective CG peak currents during the 21 April MCS.....	104
3.40	Same as Fig. 3.29 except with a +CG flash originating from the convective line at 12:52 UTC.....	108
3.41	Same as Fig. 3.29 except with a +CG flash originating from the stratiform region at 12:49 UTC.....	109

LIST OF TABLES

TABLE		Page
1.1	Weather related deaths per year from 1959 -1994 and 1994 deaths and injuries.....	2
3.1	Summary of flash statistics for the 31 October MCS stratiform region positive CG flashes that originated in stratiform (top) and non-stratiform regions (bottom).....	79
3.2	Summary of flash statistics for stratiform region positive CG flashes that originated in the 21 April MCS stratiform (top) and non-stratiform regions (bottom).....	106

1. INTRODUCTION

1.1 Lightning

Lightning has captured the curiosity and imagination of the general public and scientists throughout history. In some cultures, the luminous bolts were thought to be thrown down from the skies by ancient gods (Prinz 1977). In the last couple of centuries, scientists have studied what lightning is and possible causes of the electrical discharge. Today, lightning may be defined as a self-propagating electrical discharge resulting from the buildup of positive and negative space charge (Uman 1986).

Lightning is the number two killer of all weather related phenomenon, preceded only by flash and river flooding (Curran et al. 2000) (Table 1.1). Although lightning is reported to produce fewer damages than other weather events (Curran et al. 2000), there may be underreporting of lightning injuries, deaths, and damage to National Oceanic and Atmospheric Administration's (NOAA's) storm reports (e.g., Holle et al. 1996, Lopez et al. 1993). Therefore, lightning could cause similar, or exceed, damages caused by other weather phenomenon. Lightning has fascinated people for ages, but is a very destructive phenomenon.

Table 1.1: Weather related deaths per year from 1959 -1994 and 1994 deaths and injuries. Order is by 30-yr death rate then by 1994 deaths. Adapted from Curran et al. (2000).

Weather type	30-yr deaths per year	1994 deaths	1994 injuries
Flash flood	139	59	33
River flood		32	14
Lightning	87	69	484
Tornado	82	69	1067
Hurricane	27	9	45
Extreme temperature		81	298
Winter weather		31	2690
Thunderstorm wind		17	315
Other high wind		12	61
Fog		3	99
Other		6	59
Total		388	5165

1.1.1 Thunderstorm Electrification

Electrification within thunderstorms occurs when hydrometers of opposite polarity are separated within the cloud. This process is not fully understood and many theories have been proposed to try and explain it, primarily inductive and non-inductive charging.

1.1.1.1 Inductive Charging Mechanism

One theory is the inductive charging process, which relies on a pre-existing electric field to polarize hydrometeors. The electric field is induced by a positive charge region in the highly conductive upper atmosphere, a net negative charge on the earth's surface, and a less conductive part of the atmosphere between through which current flows. The fair weather electric field is $\sim -100 \text{ Vm}^{-1}$ near the earth's surface

(MacGorman and Rust 1998). There are two dominant methods that are considered responsible for inductive charging: 1) Wilson's selective ion capture mechanism (Wilson 1929) and 2) rebounding collisions of two polarized hydrometeors (Sartor 1954). Wilson's mechanism involves hydrometeors that are polarized by the electric field whose drift velocity must be faster than the drift velocity of ions. As shown in Fig. 1.1, negative ions are captured by the underside of the hydrometeor and positive ions, if their motion is slower than the hydrometeor fall speed, are not captured. If the positive ion's motion is faster than the hydrometeor fall speed, it is captured on the top of the hydrometeor and the net charge of the hydrometeor would be neutralized. This method is unlikely to produce electrified storms, in the absence of other charging mechanisms, because fair weather ion densities are too small in a storm cell's lifetime (e.g., MacGorman and Rust 1998).

The other inductive method is a particle-particle collision process. Precipitating hydrometeors are polarized by the electric field as well as cloud particles. As these particles collide, charge is transferred from the bottom of the falling precipitating particle to the cloud particle and the opposite charge is transferred from the cloud particle to the precipitating particle as shown in Fig. 1.2. Charge separation occurs as a result of particle sedimentation due to the force of gravity. The larger, negatively charged precipitating particles have terminal velocities which cause them to fall out of the cloud, while the smaller, positively charged cloud particles remain suspended or move upward in updrafts (e.g., MacGorman and Rust 1998). There are limitations, however, to the inductive mechanism. In order to strengthen the existing electric field,

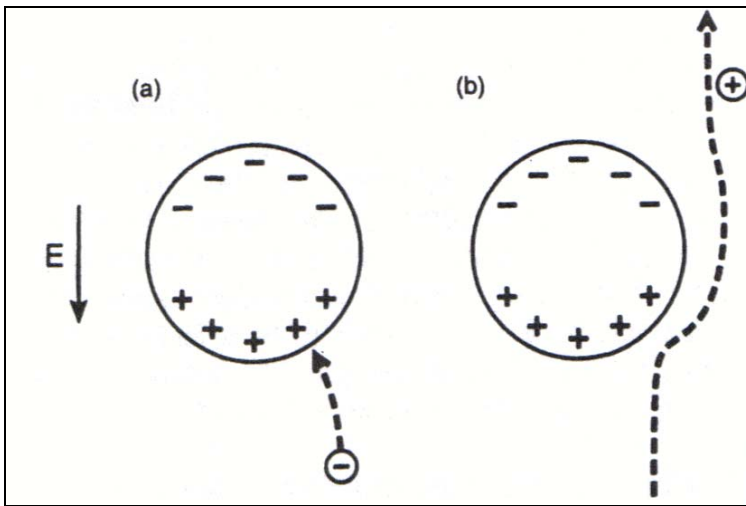


FIG. 1.1: Depicting selective ion capture of (a) collision between an uncharged water drop polarized in an electric field and a negative ion and (b) deflection of a positive ion from an uncharged polarized drop. Adapted from MacGorman and Rust (1998).

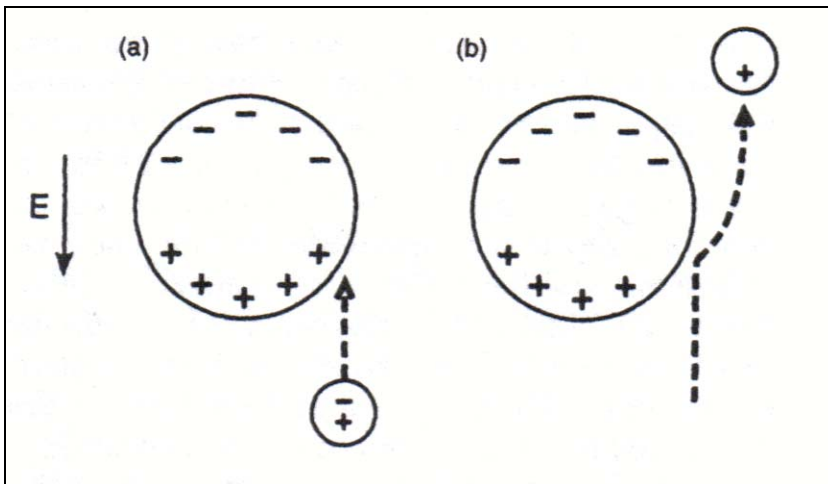


FIG. 1.2: Induction charging of rebounding particles. Adapted from MacGorman and Rust (1998).

colliding particles must separate with positively charged particles moving to a positive charge region and negatively charged particles moving to a negative charge region.

Also, the conductivity of the colliding particles must be great enough so that charge may be transferred during the time of contact (e.g., MacGorman and Rust 1998). Research has shown that this process can only be effective when the electric field is much greater than the fair weather electric field, thus suggesting that the electric field must already be increased by some other method for this process to be a viable contributor to storm electrification (Aufdermaur and Johnson 1972).

1.1.1.2 Non-Inductive Charging Mechanisms

The non-inductive charging (NIC) mechanisms, which involve rebounding collisions between ice particles, are the most widely accepted theory for cloud electrification. Unlike the inductive charging mechanisms, NIC processes transfer charge without the effects of the electric field (Saunders 1993). Many lab experiments have supported this theory (e.g., Takahashi 1978, Gaskell and Illingworth 1980, Jayaratne et al. 1993). As small ice crystals collide and rebound from larger ice particles (i.e., graupel or hail) in the presence of super-cooled water, the graupel takes on a negative charge while the ice crystals take on a positive charge. Differential sedimentation of the oppositely charged ice particles produces an electric dipole with positive charge at the top of the thunderstorm and a layered negative charge region below. Takahashi (1978) found that the amount of charge and sign deposited on the large ice particle depend on the temperature and liquid water content of the cloud where the collision occurs. Many studies have supported Takahashi (1978); however, more

parameters were also found to affect the sign and amount of charge deposited, such as: the size of the ice crystals colliding with graupel, impact velocity, and contaminants in the water droplets (e.g., Keith and Saunders 1990). The results from Takahashi (1978) and Saunders et al. (1991) on the effect of polarity on cloud water content and temperature are broadly consistent (Fig. 1.3). They conclude that if rebounding collisions occur below the charge reversal temperature, which is a function of liquid water content, then the charge transfer reverses, with graupel taking on a positive charge and the rising ice crystals taking on a negative charge. This non-inductive charging mechanism is thought to cause the 'classical' tripolar cloud charge structure (Fig. 1.4). Above the charge reversal temperature (-10°C to -20°C), negative (positive) charge is transferred to graupel (ice crystals) creating a main negative and upper positive charge layers while below the reversal temperature, graupel acquires positive charge and creates the lower positive charge region (e.g., Jayaratne et al. 1983).

One possible theory explaining the transfer of charge during collisions involves differences in quasi-liquid water layers on colliding particles. As the particles collide, mass transfers from the thicker to the thinner quasi liquid layers. Mass also tends to flow from warmer surfaces to colder surfaces and high curvature to low curvature particles. Therefore, when particles collide, negative charge and mass will transfer from the thicker quasi liquid layer to the thinner one. As these particles separate, the warmer highly curved particle becomes positively charged while the cooler less curved particle becomes negatively charged (Baker and Dash 1994).

Another theory is contact potential charging where the charging of graupel is based on its riming growth rate. At temperatures below the charge reversal temperature, graupel is negatively charged because droplets freeze fast to its surface and produces a contact potential difference between it and a colliding ice crystal. At higher temperatures, droplets do not freeze as fast and graupel surface growth is enhanced inducing positive charge transfer upon contact (Saunders et al. 1993).

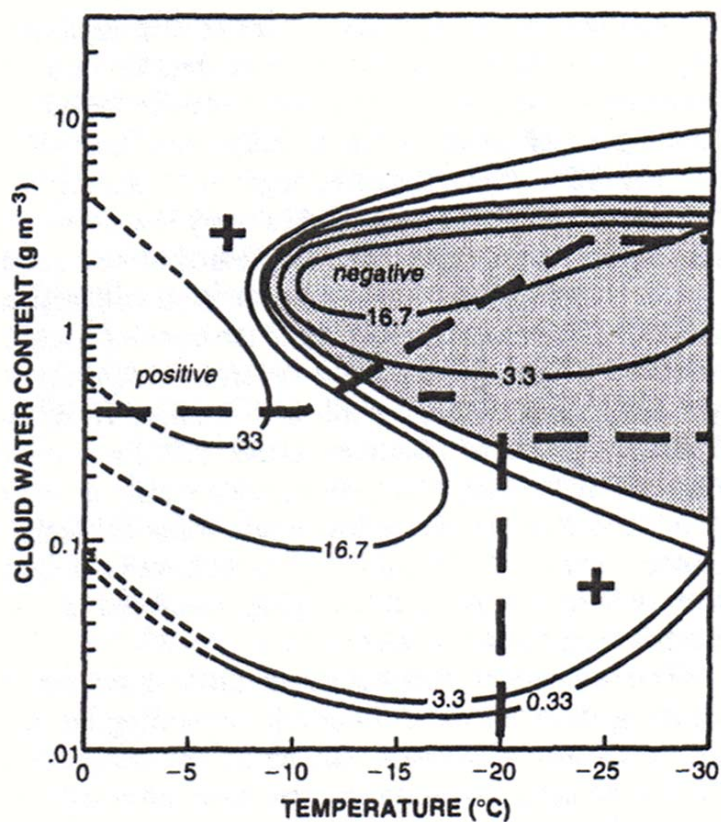


FIG. 1.3: The polarity of charge gained by graupel as a function of temperature and liquid water content for Takahashi (1978) and Saunders et al. (1991) laboratory experiments. Bold dashed lines are the results from Saunders et al. (1991) experiments while the solid contours labeled with charge (fC) values gained by graupel are from the Takahashi (1978) experiments with shading indicating negative charge. Adapted from MacGorman and Rust (1998).

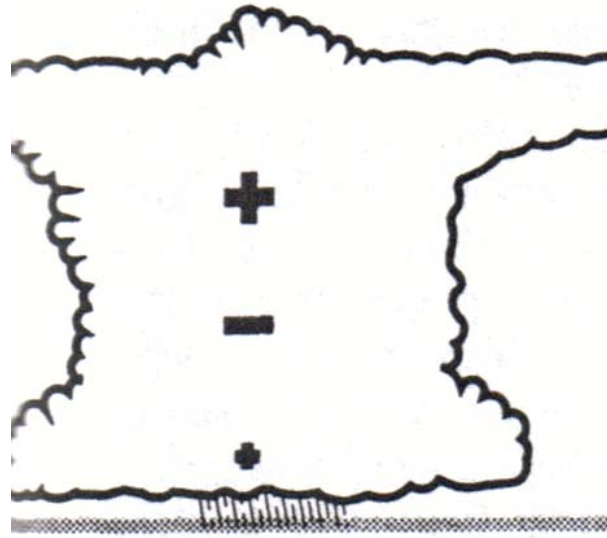


FIG. 1.4: Depiction of the thunderstorm tripole charge structure. The thunderstorm dipole is made up of the main negative and upper positive charge regions. The addition of the lower positive charge region accounts for the tripole structure. Adapted from MacGorman and Rust (1998).

Also, since water freezes from the outside in, there is a temperature difference between the outside shell and the inner side of the shell. This difference in temperature causes a thermoelectric effect, which creates a positive charge on the outside shell and a net negative charge on the inside of the shell due to the diffusion of higher mobility H^+ ions into colder ice (Wallace and Hobbs 1977). Due to the expansion of water as it freezes, ice splinters may break off from the outside shell as the droplets freeze completely on the hailstone. The ice splinters will carry away a net positive charge and leave the hailstone with a net negative charge (Wallace and Hobbs 1977). Also, collisions may break off positive carrying splinters, leaving a larger negatively charged ice particle. This theory may contribute to the explanation of the upper positive and

main negative regions. Below the reversal temperature, these charging could be reversed due to longer freeze times. It is more likely that the positive graupel charging below the reversal temperature is caused by one of the other theories (Saunders 1993).

1.1.1.3 Other Charging Mechanisms

Although the NIC mechanism by rebounding collisions, along with the inductive charging process once the electric field is strong, is thought to produce the thunderstorm tripole charge structure, there is another charging processes that may play a role in screening layers and also the lower positive charge region: the convective charging mechanism (e.g., Williams and Lhermitte 1983). The fair weather electric field provides an abundant source of positive space charge near the surface of the earth as positive ions flow from the ionosphere toward the surface. Once an updraft forms, the positive space charge is advected upward into the storm. Negative charge, produced by cosmic rays, is attracted to the top of the cloud by the advected positive charge and attaches to cloud particles along the cloud boundary. Cooling by entrainment produces downdrafts along the sides of the cloud that advect the negative charge downward along the edges and toward cloud base. This negative charge at the base of the cloud induces positive corona by the generation of positive ions by positive point discharge, which in turn produces additional positive charge at the base of the cloud, fueling the process. The mechanism was ruled out as a cause for total cloud electrification by Chauzy and Soula (1999) (among others) who found that the total charge produced was comparable to that of a single flash. They did note however, that the corona charge transported to the base of the cloud could contribute to the lower positive charge region.

Melting can also induce charging in a thunderstorm (Simpson 1909, Drake 1968), although the effects are seen more in stratiform precipitation (e.g., Shepherd et al. 1996). If the electric field is positive at 0°C, then the upper side of the drops will induce a positive charge. As the drop breaks, the fragments coming off the top of the drop will be positively charged and the remaining drop will be negatively charged, creating a positive melting layer. As a precipitation particle, inductively charged in a positive electric field, melts, it sheds positively charged droplets, creating a positive charge layer while the negatively charged larger particles fall to the ground (Simpson 1909). Drake's mechanism is a non-inductive melting mechanism. As the particle melts, it would shed negatively charged particles regardless of the electric field, creating a negatively charged layer near the melting level as the positively charged particles fall to the ground (Drake 1968).

1.1.2 Thunderstorm Charge Structure

The electric tripole structure discussed earlier with the upper main positive region, main negative region, and lower positive region is the general electrical structure of thunderstorms. However, it is understood that more complex vertical electrical charge structures exist in thunderstorms (Fig. 1.5) (Stolzenburg et al. 1998b). In their studies of several different storm types (New Mexican thunderstorms, MCS convective cells, and supercells), Stolzenburg et al. (1998b) indicate a negative charge region located near the top of the thunderstorms in addition to the tripole structure in the updraft region of thunderstorms. Also, they found six separate charge regions exist outside the updrafts and concluded that other charge mechanisms, such as those listed above, not

just the NIC mechanism of rebounding collisions of ice particles, contributed to these charge structures.

1.1.2.1 The Lightning Flash

When the potential difference between two separated charge regions exceeds the electrical breakdown or breakeven field (which is less than the electrical breakdown field due to a sustained electron avalanche) (e.g., MacGorman and Rust 1998), a lightning flash occurs. There are two types of lightning flashes: 1) Cloud to ground (CG) flashes, flashes with a ground contact point; and 2) intracloud (IC) flashes, flashes that occur either within the confines of a thundercloud, between thunderclouds, or between a thundercloud and air. IC flashes usually dominate ordinary convective storms with common IC/CG ratios of 5 or 10 to 1 (Krehbiel 1986). As the storms increase in intensity, IC:CG ratios also increase (Williams 2001). IC flashes often occur before CG flashes with a possibility of 10 or more IC flashes preceding the first CG flash (e.g., Williams 1989). CG lightning often occurs between the main negative charge region and the ground and IC flashes occur between oppositely charged regions, such as the upper positive and main negative charge regions (Shao and Krehbiel 1996). Although IC flashes do not affect objects or persons on the ground, they do affect the safety of vehicles that pass through electrified clouds such as aircraft and spacecraft. IC discharges are composed of two stages; an early or active stage and a late or final stage. The first stage consists of a bidirectional streamer with the positively charged segment propagating into the negative region and transferring negative charge through the flash origin point to the negatively charged segment of the streamer propagating through the

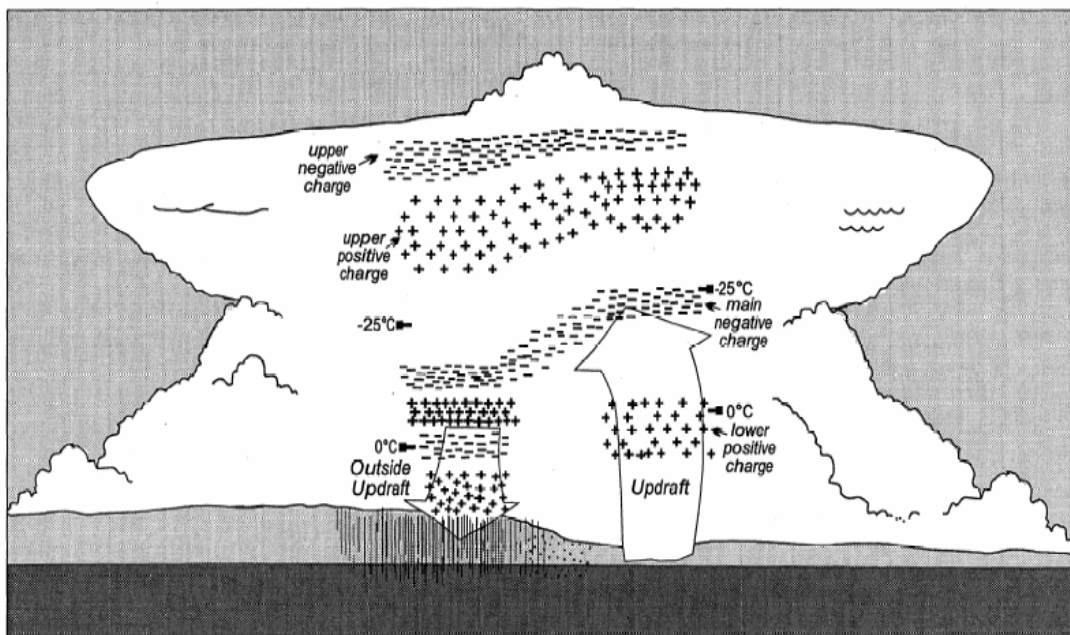


FIG. 1.5: Conceptual model of the storm structure for updraft and non-updraft regions of a convective thunderstorm. Shown is the tripole electrical structure plus an additional upper negative charge layer in the updraft region. Also shown are the 6 charge layers found in non-updraft regions of convection. The height levels (indicated by temperature levels), relative charge density (indicated by densities of plus and minus signs), and relative strengths of updrafts and downdrafts (indicated by arrow size) may vary depending on convective type of storm. Adapted from Stolzenburg et al. (1998b).

positive region. The second stage of this flash begins once this connection between the positive and negative regions is lost. Then negative charge is fed to the flash origin point from other sources in the negative region (Rakov and Uman 2003).

Even though IC flashes usually dominate storms, more studies have focused on CG flashes due to their destructive force, safety implications, and the availability of geo-location measurements. Once the electrical breakdown point is reached, the following processes occur as summarized from Rakov and Uman (2003). A CG flash is initialized

by a step leader moving intermittently toward the ground carrying either positive or negative charge. Branching may occur as the leader attempts to find the path of least resistance. As the stepped leader approaches ground to within ~50 m, an upward leader of opposite charge is initiated due to the increased electric field near the surface and propagates upward to connect to the stepped leader in the attachment process. Once the connection is made, the stepped leader is effectively grounded and the return stroke is initialized. The return stroke lowers the charge originally deposited on the stepped leader to the ground, usually on the order of tens of coulombs. If additional charge is available at the top of the lightning channel, subsequent strokes could occur. Subsequent strokes are indicated by a dart leader, which may not be branched because the heated and less dense path created by the previous stroke is the path of least resistance. However, if the time differential between the previous stroke and dart leader is ever in excess of 100 milliseconds, the air would have sufficiently cooled and a stepped leader will once again be formed with branching in order to find the most favorable path. These processes are also shown in (Fig. 1.6).

There are four types of CG lightning: downward negative lightning, downward positive lightning, upward negative lightning, and upward positive lightning (Rakov and Uman 2003, MacGorman and Rust 1998). Flashes that lower negative charge to the ground (downward negative lightning) make up 90% of CG flashes in ordinary thunderstorms (Orville and Huffines 2001). Positive CG dominated storms are rare, with only 15% of warm season severe storms in the U.S. producing predominately positive CG flashes (Carey et al. 2003). Positive CGs are thought to be responsible for

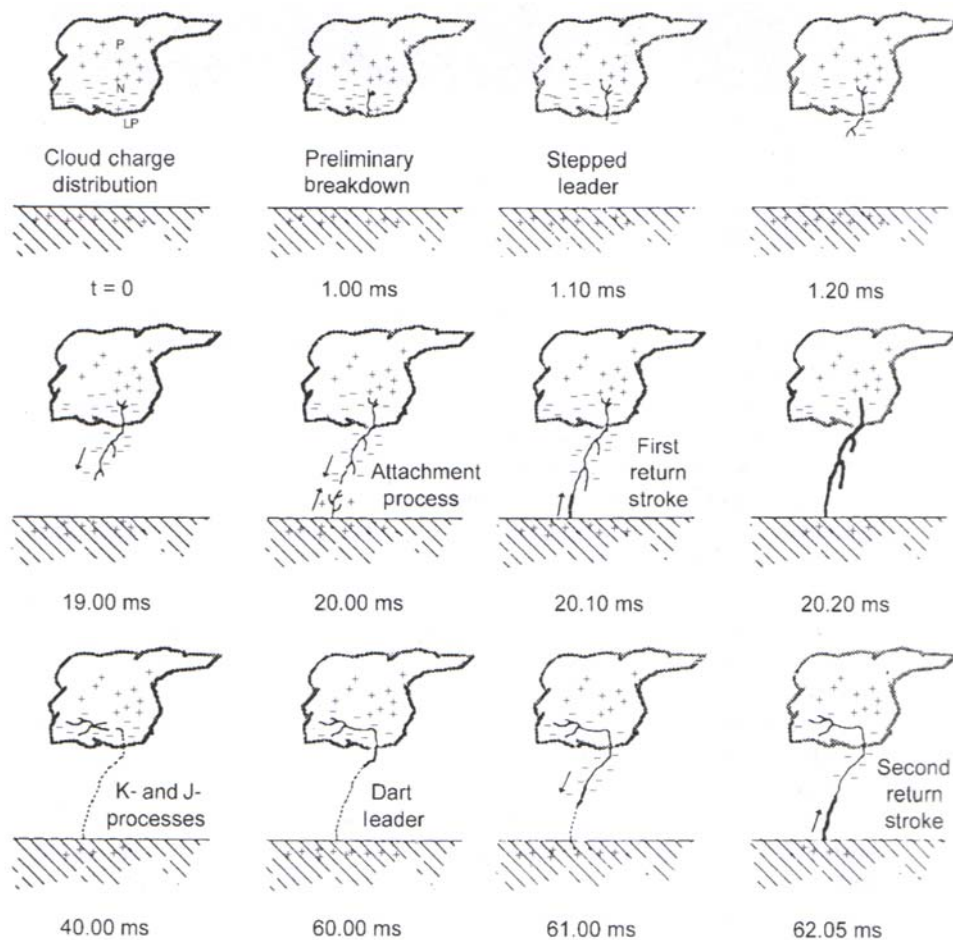


FIG. 1.6: Diagram showing the various processes involved in a negative CG lightning flash. Adapted from Uman (1987).

forest fires and the majority of lightning damage seen due to their longer continuing current (Rust et al. 1985).

1.2 Mesoscale Convective Systems (MCSs)

Mesoscale convective systems (MCSs) are the largest of the thunderstorms that contain regions of both convective and stratiform precipitation under one cloud complex. They may span $\sim 100 \text{ km}$ in a horizontal direction and have lifetimes of approximately

10 hours (Zipser 1982, Houze 2004). Because of their size and long lifetimes, they account for a large proportion of precipitation in both the tropics and midlatitudes. They are responsible for 30-70% of U.S. warm season rainfall (Fritch et al. 1986). MCSs often contain severe weather in the form of damaging winds, hail, and tornadoes and additionally pose a flash flooding threat (Maddox 1983, Houze et al. 1990). Not only do MCSs produce severe weather, they are also prolific producers of lightning and contain a significant fraction of warm season CG lightning in the central U.S. (Goodman and MacGorman 1986).

1.2.1 Organizational Modes

Blanchard (1990) studied different organizational modes of MCSs that occurred in springtime over Oklahoma. He found that spatial characteristics of MCSs may be grouped into three convective modes: linear convective systems, occluding convective systems, or chaotic convective systems (Fig 1.7). The linear convective system consists of a series of convective cells that converge to form a linear structure and a region of stratiform precipitation with a transition zone, or reflectivity trough, between. Occluding MCSs result from the merging of one convective line typically situated east-west along a stationary boundary with another convective line that is typically organized north-south along an advancing trough. The third pattern involves dispersed convective cells that never organized into a linear structure. The linear MCS is the most prevalent (68%) of these patterns, followed by chaotic convective systems (24%) and occluded convective systems (8%) (Blanchard 1990).

The most prevalent mode of MCS, linear MCSs, develops by one of four processes: broken line, back building, broken areal, or embedded areal (Fig. 1.8) (Bluestein and Jain 1985). The broken line process occurs when several discrete cells form simultaneously and join into a linear structure through expansion or by newer cells developing between the older cells. Back building lines result from newer cells developing upstream, relative to storm motion, from older cells and then merging with the older cells. Linear MCSs that develop from a broken areal configuration start from a chaotic displacement of convective cells which eventually organize into a linear structure. The last development classification for an MCS is the embedded areal process in which a convective line forms within a region of stratiform precipitation (Bluestein and Jain 1985).

As linear MCSs mature, they tend to develop one of three types of stratiform regions: trailing, leading, or parallel (Parker and Johnson 2000). The first type, trailing stratiform MCS, includes a leading convective line with maximum reflectivities followed by a transition zone made up of lower reflectivities and then by a secondary maximum of reflectivity (stratiform region) (Houze et al. 1990). In the second case, leading stratiform MCSs, the convective lines are preceded by the stratiform region. A transition may or may not be present in this case. The third case, MCSs with parallel stratiform regions, are seen when the stratiform region moves parallel to the line and often to the left of the convective lines motion (Parker and Johnson 2000).

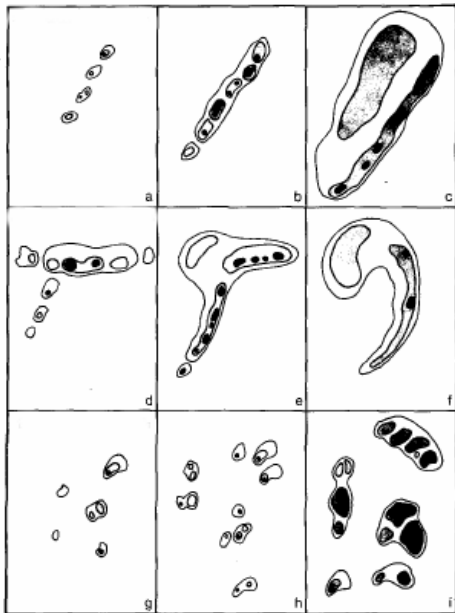


FIG. 1.7: Schematic of the evolution of three convective modes seen in PRE-STORM program. The three modes are: (a-c) linear convective systems, (d-f) occluding convective systems, and (g-i) chaotic convective systems. Adapted from Blanchard (1990).

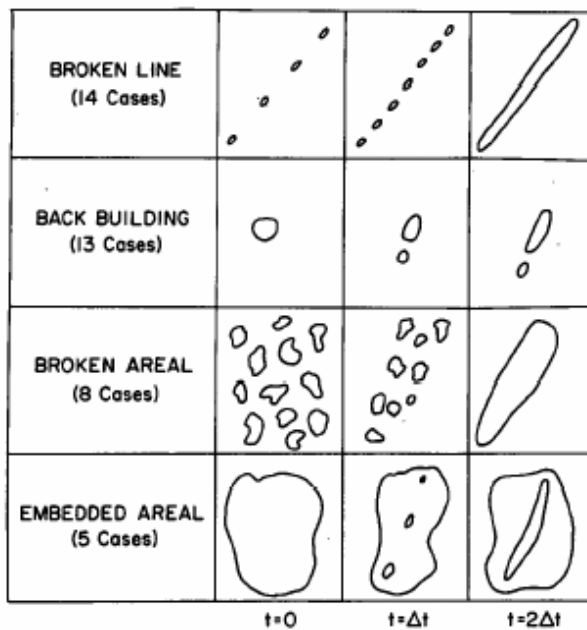


FIG. 1.8: Idealized depiction of squall line formation. Adapted from Bluestein and Jain (1985).

Not only did Parker and Johnson (2000) find the trailing stratiform type to be the most prevalent (58%) of the cases they studied, they also found that most MCSs evolve into trailing stratiform MCSs as they mature. Houze et al. (1990) also found that a majority (two thirds) of the total number (63) of MCSs they studied over Oklahoma had a leading convective line followed by a trailing stratiform region. They further dissect the leading line, trailing stratiform (LLTS) into symmetric and asymmetric MCSs (Fig. 1.9). The symmetric case exhibits a homogeneous convective line with a stratiform region centered directly behind it. The asymmetric case involves a convective line with stronger cells on its southern, southwestern, or western end and the stratiform region that is usually located on the opposite side of the line toward its northern, northeastern, or eastern ends. Asymmetric MCSs are typically the dissipating and final stages of MCSs (Loehrer and Johnson 1995).

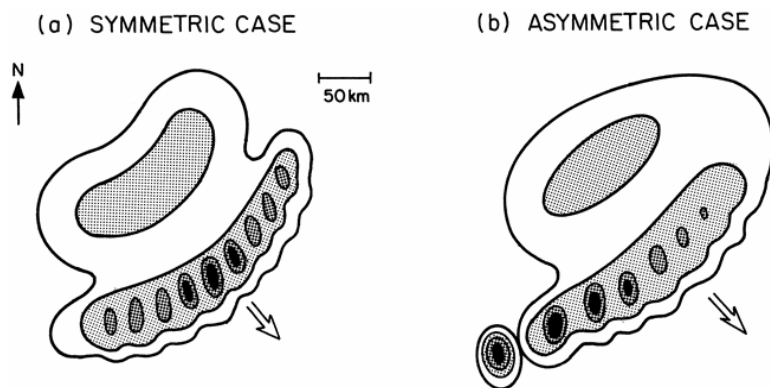


FIG. 1.9: Schematic depicting (a) symmetric and (b) asymmetric types of leading line-trailing stratiform MCS precipitation organization (from Houze et al. 1990). Large vector indicates direction of system motion. Levels of shading denote increasing radar reflectivity, with most intense values corresponding to convective-cell cores. Adapted from Houze et al. (1990).

1.2.2 Kinematic and Microphysical Processes of MCSs

A conceptual model of a line normal cross-section of a mature leading-line trailing stratiform (LLTS) MCS showing the three main regions of a LLTS MCS (convective, transition zone, and stratiform) and the kinematic processes that take place within each region is shown in Fig. 1.10. The formation of the convective line typically begins when warm, moist air is forced over cooler, denser air by a lifting mechanism (e.g., cold front). Updrafts created along this boundary form new convective cells. As the convective cells mature and congeal together, the convective line forms and begin to take on the characteristics as stated in Houze (1990). These characteristics include the leading convective line having slight arc shape, convex toward the leading edge, with a generally northeast to southwest orientation. The line consists of a series of elongated intense reflectivity cells oriented 45-90° to the line connected by echoes of moderate reflectivity. The elongated cells produce a large reflectivity gradient and the appearance of a jagged leading edge along the line. A weaker reflectivity gradient is seen toward to the rear of the line. The convective line moves normal to line orientation at speeds typically greater than 10 m s^{-1} (Houze 1990).

In response to strong (order 10 m s^{-1}) vertical motions in the mature cells, the heaviest precipitation develops and falls in the convective region. The low level downdrafts created by falling rain and hail (precipitation loading) and evaporation descends to the ground and spreads out underneath the convective region. Evaporative cooling of this air produces the surface cold pool that advances ahead of the convective line. As the cold pool strengthens, smaller, lighter particles are carried farther aloft and

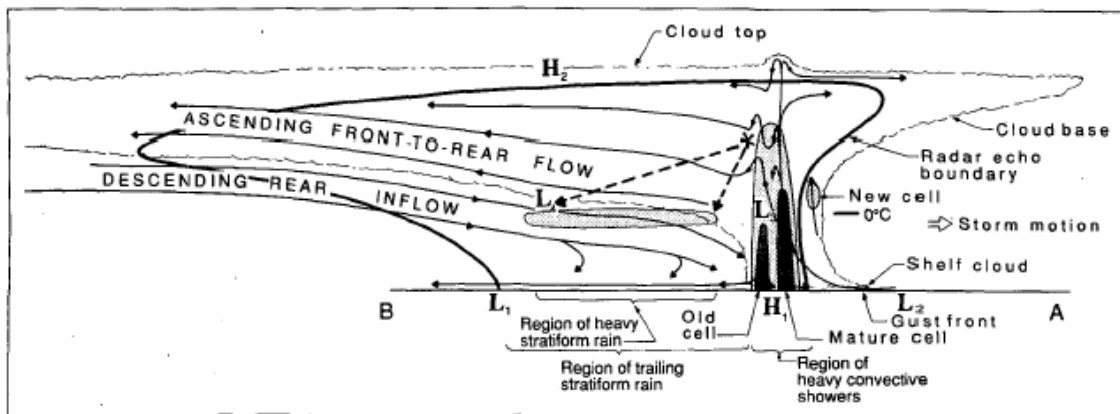


FIG. 1.10: Conceptual model of a mature leading line trailing stratiform MCS viewed in a vertical cross section normal to the convective line. See text for further explanation. Adapted from Houze et al. (1989).

swept rearward into the stratiform region by the storm-relative front-to-rear flow (Houze 1989).

Rutledge et al. (1988) found typical storm-relative front-to-rear flow speeds of 20 m s^{-1} . A meso-low (Fritsch and Chappel 1980) develops ahead of the advancing cold pool as it provides another lifting mechanism in which new cells may develop, regenerating the line (L_2 , Fig. 1.10). A meso-high (Fujita 1955), in addition to the surface cold pool, is also created at low levels by the low level downdrafts (H_1 , Fig 1.10). Also, latent heating due to condensation and freezing of water particles creates a small hydrostatic low at the base of the most intense updrafts (L_3 , Fig 1.10). Mature cells are followed by older dissipating cells which are characterized by an updraft core and downdraft at mid to upper levels. As these cells dissipate they are carried rearward by the storm-relative front-to-rear flow (Houze 1989).

The convective region is followed by a reflectivity trough (i.e., transition zone) caused by deep subsidence, which inhibits particle growth. The subsidence is seen through all levels and is made up of dynamically-driven upper level downdrafts that follow the upper level updrafts of the mature and dissipating cells, and also a low-level downdraft created by melting and evaporative cooling. These two downdrafts create a net region of downward motion (Biggerstaff and Houze 1993, Houze 1993). The subsidence at midlevels results in less ice particle growth via deposition and aggregation than seen in the stratiform region following, and therefore results in the reflectivity minimum between the convective and stratiform regions (Biggerstaff and Houze 1993). Also, Yeh et al. (1991) suggested that the reflectivity minimum was due to precipitation sizes being half as large as those found in the trailing stratiform region.

LLTS MCSs have a stratiform region consisting of a large area ($> 10^4 \text{ km}^2$) of a secondary maximum of reflectivity (20 – 40 dBZ) separated from the convective region by a low reflectivity channel (Biggerstaff and Houze 1991, Houze 1990). The stratiform region is composed of ice particles that are carried rearward from the convective line by the ascending front-to-rear flow. As these smaller particles fall through the stratiform region and the broad and relatively weak mesoscale updraft (order 0.1 to 1 m s^{-1}), they grow by deposition and aggregation, and begin to melt near the height of the 0°C isotherm. Once the melting level is reached, melting ice aggregates generate enhanced reflectivity (i.e., known as the radar bright band) (e.g., Biggerstaff and Houze 1991). The bright band occurs because ice develops an outer coating of water as it melts which increases its reflectivity. Also, as the particle melts, it becomes more aerodynamic and

has a faster terminal velocity than the snow above. This decreases the particle number density and therefore decreases the reflectivity in regions below the melting level. These processes produce a layer of enhanced reflectivity near and just below the melting level, thus creating the radar bright band (e.g., Rinehart 2004). A relative increase in precipitation is found under the bright band compared to surrounding areas (Rutledge and Houze 1987). The strongest mesoscale updrafts normally occur in the front of the radar bright band and decrease rearward through the stratiform region (Houze 1993).

Below the radar bright band and in the lower stratiform region is a characteristic mesoscale downdraft created by evaporation, melting, and sublimation (e.g., Smull and Houze 1985). Enhancing the downdraft is a relatively dry, sinking air mass that enters the system through the rear and is sometimes labeled the rear inflow jet. The jet usually enters the rear of the system at upper levels and slowly descends through the melting layer into lower levels before making its way to the rear of the convective line. A notch in the rear stratiform cloud deck is a visible sign of the rear inflow as the precipitation is eroded away by the dry mid-level air (Smull and Houze 1985). The rear inflow jet is generated by a combination of horizontal buoyancy gradients (Weisman 1992) and line end effects (Skamarock et al. 1994). Below the rear inflow jet at the rear of the system, a wake low (not shown in Fig 1.10) is created by subsidence warming of dry air (Fujita 1955). A meso-low (Brown 1979) (L4, Fig 1.10) is created near the melting level by the warm buoyant rising air above the rear inflow jet and sinking air below it. A meso-high is found above the entire mesoscale cloud system (H2, Fig 1.10).

1.3 Electrical Properties of MCSs

1.3.1 MCS Charge Structure

The charge structure of MCS convective regions seen observationally and in models resembles the structure described for thunderstorms shown by Fig. 1.5. Stolzenburg et al. (1998a) used 16 electric field soundings from multiple MCSs to infer the charge structure of MCS convective regions. In the updraft regions, a lower positive charge region from 2 to 6 km is found, above which resided a negative layer between 6 and 8 km. Above the main negative region is an upper positive region followed by a negative charge layer from 11-12 km. The upper negative charge region is inferred to be caused by a screening layer while the three lower charge layers are thought to be due to non-inductive charging mechanisms. Electric field change measurements indicate that most of the lightning takes place between the upper positive and main negative charge layers (Stolzenburg 1998a).

Two additional charge layers are found outside the updraft regions (Stolzenburg 1998a). The lowest layer, near cloud base, contains a positive charge. Above this layer is a shallow ($z < 0.5$ km) negative layer. A positive layer, above the negative layer, is found at 4-6 km followed by yet another negative charge region. Just like the previously discussed updraft charging layers, there is an upper positive charge followed again by an upper negative charge above the main negative charge layer. The charge magnitudes in the non-updraft regions are larger and the charge depth generally smaller than those from the updraft portions of the MCS convective region. The main difference between the two different regions in the convective line lies in the charge layers beneath the main

negative charge region. In the non-updraft regions, there is a negative charge layer sandwiched between two positive layers below the main negative charge layer (Stolzenburg et al. 1998a). The additional two charging layers in the non-updraft regions may indicate prevalent charging mechanisms other than ice-ice collisional non-inductive charging, such as non-inductive melting charging (Drake 1968) and inductive charging (Stolzenburg 1998b).

The transition zone lies behind the convective region of the MCS in a region of subsidence and lower reflectivity values. Schuur et al. (1991) found very similar charge regions in the transition zone as those found by Stolzenburg et al. (1998a) in non-updraft convective regions, except for the lowest positive charge region. The absence of the lower positive charge region is likely due to the absence of lower precipitation particles in the transition zone. Schuur et al. (1991) proposed that advection of charge from the convective regions contributed to the charge structure since all the charge layers were found in the front-to-rear flow. They also suggested screening layers could contribute to the upper and lower charge layers, while in-situ charging could contribute to internal charge layers because reflectivity contours of the transition zone are consistent with graupel fallout speeds and the charge layers are consistent with the inverted dipole theory.

Stratiform charging processes are not as well understood as those in the convective region and transition zone. Marshall and Rust (1993) found two types of vertical electrical structures in stratiform regions in MCSs. The first (type A) structure consists of four main alternating polarity charge regions with the lowest charge of

negative polarity. The type A structure also has a fifth charge region at cloud top with negative polarity. Their second (type B) electrical structure had fewer charge regions with just the four main charge layers. Another difference between the two types of electrical structure is the opposite polarities near the melting level. In a study of electrification of symmetric and asymmetric MCSs, Schuur and Rutledge (2001) noted that the type A (B) structure was most likely associated with a symmetric (asymmetric) MCS. Once again, there are two theories used to explain the charged layers. One theory is in-situ charging, where local kinematic and microphysical processes within the stratiform region produce the charge structure. Candidate in-situ charging mechanisms include the ice-ice collisional non-inductive charging process, which requires the presence of supercooled water, small ice crystals, and larger ice particles such as aggregates or graupel (e.g., Rutledge et al. 1990). Another potential in-situ charging process is melting charging (Simpson 1909, Drake 1968) near the bright band of the stratiform region (e.g., Shepherd et al. 1996). The other theory is charge advection, where positive charge, typically resident on small ice particles from the top of the convective clouds, is advected by the storm-relative front-to-rear flow into the stratiform region (e.g., Rutledge and MacGorman 1988).

Stolzenburg et al. (1994) found that charge layers tend to follow the descending slope of reflectivity contours from upper levels in the convective region rearward into the stratiform regions. They found that the uppermost positive layer could be correlated to 25-30 dBZ contours and the densest negative layer to the 35 dBZ contour. The

negative layer at cloud top is thought to be a screening layer. Charge advection is thought to be the primary cause of these layers in the upper stratiform region.

They also noted, along with Schuur and Rutledge (2000a) and Shepherd et al. (1996), that the melting level is associated with the densest positive charge (similar to type A structure seen by Marshall and Rust (1993)) near 4 km. Candidate mechanisms responsible for the positive layer seen near the melting level are inductive charging by drop breaking, melting, and non-inductive charging. If the electric field is positive at 0°C, then the upper side of the drops will induce a positive charge. As the drop breaks, the fragments coming off the top of the drop are positively charged and the remaining drop is negatively charged via the inductive melting mechanism, creating a positive melting layer. Since the positive layer is found at the melting level, melting charging (Simpson 1909, Drake 1968) is also considered. The Simpson (1909) inductive melting mechanism is the likely cause for a positive charge layer near the melting level because of the positive electric field in that region. The positive electric field is normally seen in electric field soundings due to the negative charge layer right above the melting level (Stolzenburg et al. 1994). The non-inductive melting mechanism of Drake (1968) is less likely to produce the charge structure seen near the melting level because it would always result in a negative charge at that level. The melting mechanism could account for the observed charge structure at the melting level in the stratiform region as opposed to the convective region because aggregates shed particles easier than rimed graupel (Shepherd et al. 1996). The collisions between precipitation and ice cloud particles could induce a positive charge on the precipitation particles and negative charge on the

cloud particles via ice-ice NIC mechanism. This may help to explain the negative charge region seen above the melting level; however, the question remains on how the falling positively charged precipitation particles would be related to the melting level since they would continue to fall to the earth (Stolzenburg 1994, Shepherd et al. 1996).

The negative charge region beneath the bright band corresponds to the 40 dBZ contour, except in places of stronger precipitation. The negative charge layer is either a screening layer or produced by negatively charged precipitation from the drop breaking mechanism. Since the negative charge is not seen in high precipitation, it is likely that the layer is formed by screening (Stolzenburg et al. 1994). The charge region below the cloud is positive and is likely due to positively charged precipitation (e.g., Moore and Vonnegut 1977) or by positive ions discharged from the ground (e.g., Standler and Winn 1979). A conceptual model of mature MCSs that encompasses the previously discussed convective, transition zone, and stratiform regions' charge structure and also includes the flow structure from Fig. 1.10 is shown in Fig. 1.11. Unlike convection, the stratiform region is very complex and contains many large stratified charge regions. Observational and modeling studies support the mixture of charge advection and in-situ charging mechanisms in the generation of these charge layers (e.g., Rutledge et al. 1990, Stolzenburg 1994, Schuur and Rutledge 2000a,b). Further research needs to be conducted in order to gain a better understanding of charge layers and charging mechanisms in the stratiform region of MCSs.

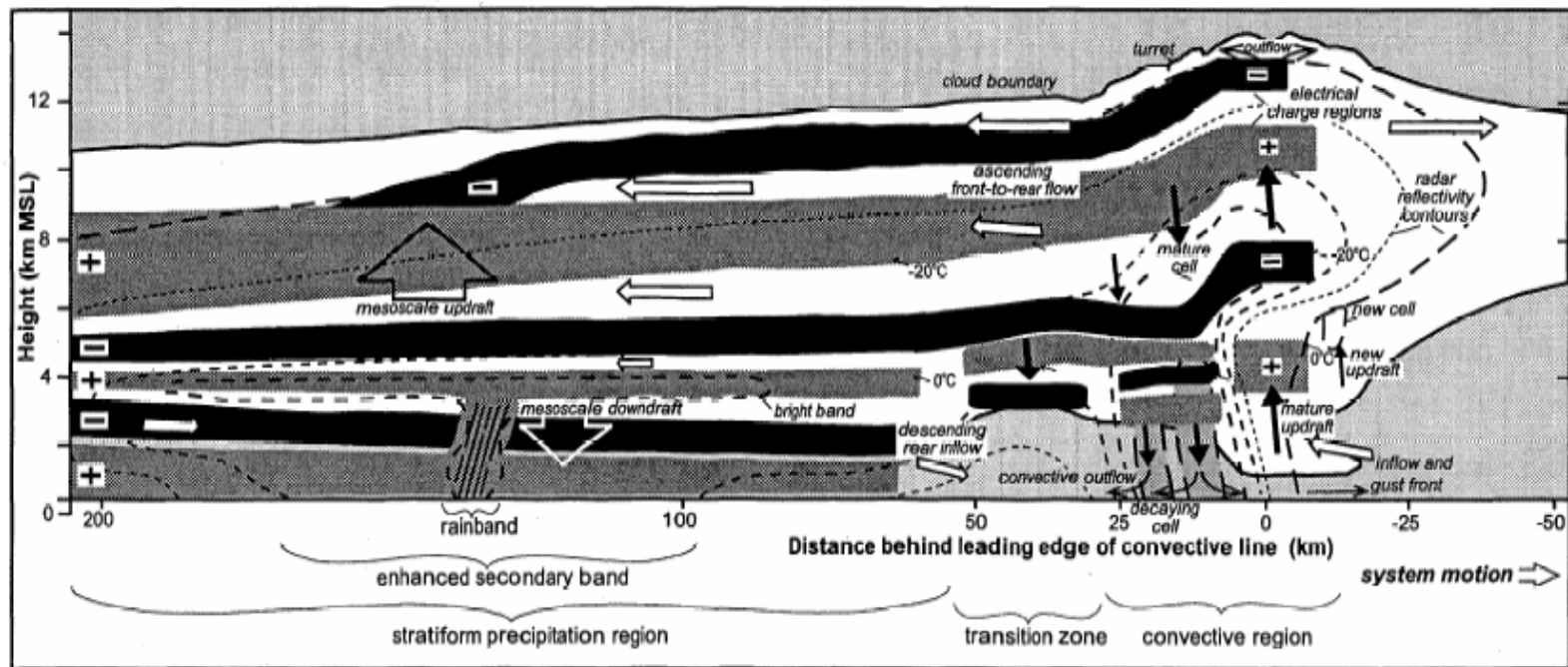


FIG. 1.11: A conceptual model of the charge structure of mature leading line trailing stratiform MCSs. Dashed lines indicate radar reflectivity contours from 10-50 dBZ with a spacing of 10 dBZ. Positive charge layers are lightly shaded with negative charge layers shaded heavily. In the convective region and transition zone, thick solid arrows depict updrafts and downdrafts while thin solid arrows show divergent outflows. Smaller open arrows throughout the system indicate storm relative motions and larger open arrows indicate mesoscale updrafts and downdrafts. Adapted from Stolzenburg et al. (1998).

1.3.2 MCS Lightning

MCSs are known producers of abundant lightning and the electrical and lightning properties of these systems have been the focus of many research studies, with much of the past attention focusing on cloud-to-ground (CG) lightning in relation to radar or satellite inferred storm structure (e.g., Goodman and MacGorman 1986, Rutledge and MacGorman 1988, Rutledge et al. 1990). The predominant source of lightning is centered on the vigorous vertical motion and abundant precipitation ice mass found in the convective region, where thousands of flashes may occur in an hour (Goodman and MacGorman 1986). Significantly more flashes are found in the convective region than in the stratiform region, where longer flashes tend to occur (Mazur and Rust 1983). As a thunderstorm becomes more intense and vertical, it becomes more electrified (Williams et al. 1989, Goodman et al. 2005). Non-inductive charging is likely the dominant charging mechanism for the convective region (Takahashi 1978, Jayaratne et al. 1983, Illingworth 1985) as the updraft is able to maintain charge separation. Once the updraft weakens, ice particles fall, the separation of charge lessens, and the amount of IC flashes decrease (Williams et al. 1989).

Rutledge and MacGorman (1988) found that the maximum negative ground flash rate occurs with the maximum rainfall in the convective region and the maximum positive ground flash rate corresponds with the maximum rainfall in the stratiform region. This effect is known as the lightning bipole (Orville et al. 1988). The time lag between the two maximums was approximately two hours, which suggests possible charge advection from the top of the convective region to the stratiform region by the

front-to-rear flow. Another possibility is in situ charging, where lightning in the stratiform region is generated by local non-inductive charging or melting processes. An increase in stratiform electrical activity typically lags convective rainfall and is coincident with stratiform rainfall peaks (Rutledge et al. 1990, Rutledge and Petersen 1994). Holle et al. (1994) showed that negative CGs are predominant throughout the life cycle of an MCS with positive CGs increasing in the stratiform region during the mature and dissipating stages of the system. The rate of CGs found under the stratiform region is positively correlated to the magnitude of reflectivities found above the 0°C level (Rutledge and Petersen 1994).

Recently, networks capable of accurately measuring the time of arrival of impulsive VHF radiation from lightning propagation have been employed allowing researchers to produce highly detailed pictures of the three dimensional lightning structure in storms (Rison et al. 1999, Krehbiel et al. 2000, Goodman et al. 2005). Carey et al. (2005) and Dotzek et al. (2005) describe the detailed total lightning structure of mature leading-line trailing stratiform (LLTS) MCSs. According to their studies, VHF sources occur primarily in the convective region in a bimodal pattern, suggesting a tripole charge structure in the convective line. The lightning structure shown in the line-normal horizontal and vertical plane reveals a slanting lightning pathway beginning toward the top of the convective region, then descending 4-5 km downward and 40-50 km rearward through the transition zone and stratiform region in and above the bright band (Fig. 1.12). The VHF source densities also occur in layers in the stratiform region, suggesting layers of charge consistent with past electric field studies involving LLTS

MCSs (e.g., Stolzenburg 1998a). Carey et al. (2005) present a conceptual model of a mature LLTS MCS similar to Fig. 1.13 in which the general ice particle trajectory from the top of the convective region to the stratiform radar bright band corresponds to the lightning pathway. Carey et al. (2005) also examined 7 flashes producing positive CGs, all of which initiated in the MCS convective region and propagated through the stratiform region and then to the ground. In a study by Lang et al. (2004), 30 of 39 positive CG flashes originated in the convective region. They also found that positive CGs in the stratiform region deposited more charge on the ground than those from the convective region, along with Petersen and Rutledge (1992). Both Carey et al. (2005)

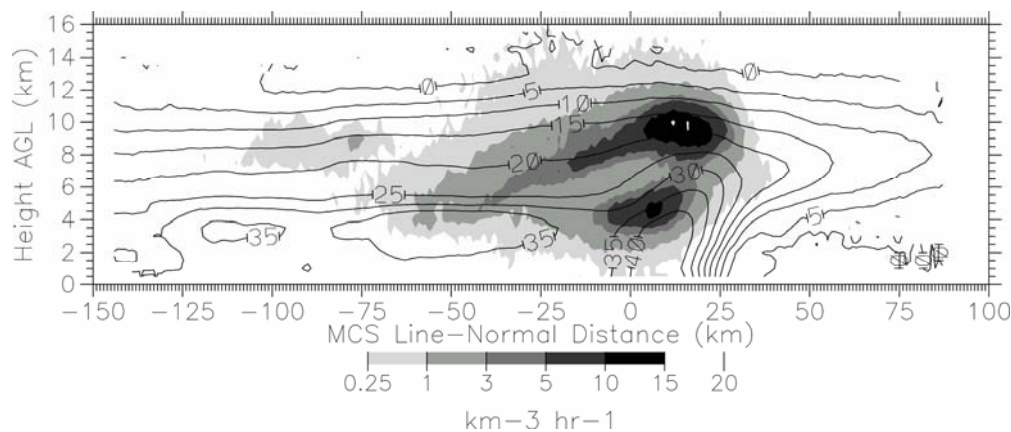


FIG. 1.12: A 30-min, line-normal vertical composite of radar reflectivity (dBZ, contours every 5 dBZ) and VHF lightning source density ($\text{km}^{-3} \text{h}^{-1}$, shaded as shown) through a mature leading line, trailing stratiform MCS over the DFW region on 16 June 2002 from 0609 to 0639 UTC. Adapted from Carey et al. (2005).

and Lang et al. (2004) suggest that the stratiform charge is a conduit for positive CG lightning from the convective line and may also initiate its own positive CGs. Lyons et al. (2003) found that as VHF source heights lowered in the two MCSs that they studied, that sprite production increased. Sprites are electrical discharges found in the mesosphere and are thought to be caused by large charge moment changes, the product of the amount of charge transferred to the ground and the lightning channel length of positive CGs (Pasko et al. 1997). The mean heights of the parent positive CG flashes associated with the sprites were found near the melting, close to 4 km.

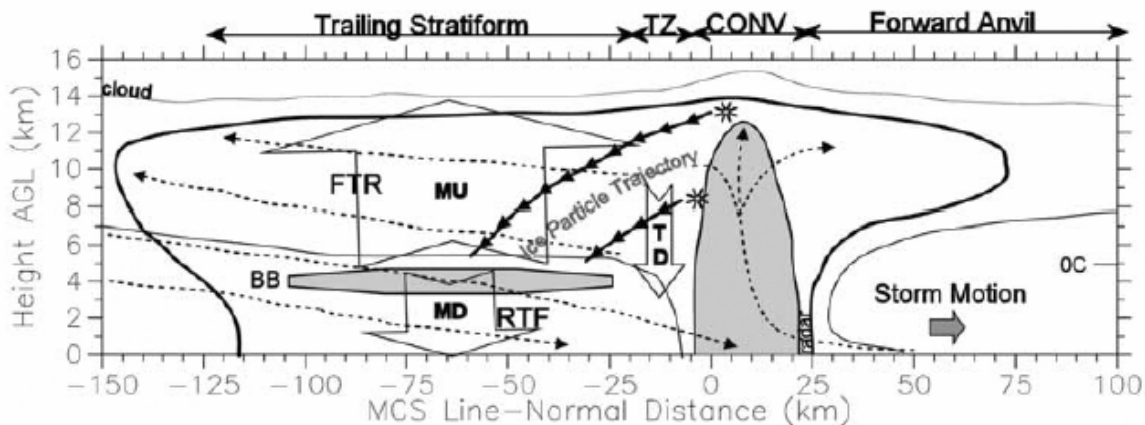


FIG. 1.13: Conceptual model of the kinematic and precipitation structure of a mature leading-line, trailing-stratiform (LLTS) mesoscale convective system (MCS) that is viewed in a vertical cross-section oriented perpendicular to the convective line (i.e., parallel to its motion) (Carey et al. 2005). Key regions of the line-normal structure are highlighted at the top, including the convective (CONV) region and transition zone (TZ). The thin line depicts the visual or satellite detected cloud boundary. The bold line depicts the radar observed outline of precipitation. The shaded areas indicate regions of enhanced precipitation or larger radar reflectivity, including the radar bright band (BB). The dashed arrows depict important storm relative flow fields, including the ascending front-to-rear (FTR) and descending rear-to-front (RTF) flows. The bold, repeating arrows indicate the approximate trajectories of ice particles, which are represented by asterisks. The direction of storm motion and height of the 0°C isotherm are indicated. Large block arrows indicate the approximate locations of the mesoscale updraft (MU), mesoscale downdraft (MD), and transition zone downdraft (TD). Adapted from Houze et al. (1989) and Biggstaff and Houze (1991).

1.4 Objective

With the recent deployment of the Texas A&M University (TAMU) Lightning Detection and Ranging (LDAR) network in Houston, Texas, the three-dimensional properties of total (i.e., CG and intracloud [IC]) lightning can be readily observed in a sub-tropical, coastal, urban environment. The network consists of 12 VHF time-of-arrival (TOA) sensors with an effective range of 130 km from the network center (Ely et al. 2007). Many MCS cases have passed over and been recorded by the Houston LDAR network since it became operational in 2005. Two LLTS formed, evolved, and traversed the Houston LDAR network on 31 October 2005 and 21 April 2006.

It is hypothesized that the intensification of stratiform region precipitation, including the bright band, plays an important role in the lightning pathway, charge structure, and total lightning production of the stratiform region. The advection of particles from the convective region and in situ processes created by the increase in the mesoscale updraft are directly related to the intensification of the stratiform region. The advection and in-situ generation of charge are also thought to lead to an increase in total electrification of the stratiform region, which should ultimately lead to increased total (IC + CG) and CG lightning production. Charge advection is considered to be prevalent throughout stratiform development, allowing the stratiform region to be a conduit for flashes originating in the convective line. On the other hand, in-situ charging is considered to increase as the mesoscale updraft develops, because of availability of cloud water and larger ice growth by deposition and aggregation, causing charge generation and more flashes to originate in the stratiform region.

The objective of the proposed thesis is to document the evolution in total lightning and radar reflectivity in two MCS cases, 31 October 2005 LLTS MCS and 21 April 2006 LLTS MCS, with emphasis on the stratiform region. These MCSs will be studied during the time in which they are well within range of and over the Houston LDAR network. Using Houston (KHGX) Weather Surveillance Radar – 1988 Doppler (WSR-88D), LDAR VHF source data, and National Lightning and Detection Network (NLDN) ground flash data, it will be shown that the total lightning structure and flash rate of LLTS MCSs evolves in response to the evolving microphysical and kinematic properties. Also, more insight into the defining microphysical and kinematic processes of a LLTS MCS, which are responsible for the observed total lightning structure, will be revealed. An investigation will also be conducted on where positive CGs in the stratiform region originate. More analysis of total lightning data in MCSs will be performed in order to improve our knowledge of MCS microphysical, kinematic, and electrical properties.

2. DATA AND METHODOLOGY

This study documents the evolution in total lightning and radar reflectivity for two LLTS MCSs on 31 October 2005 and 21 April 2006, with emphasis on the stratiform region. The Houston (KHGX) Weather Surveillance Radar – 1988 Doppler (WSR-88D) is used in conjunction with LDAR VHF lightning source data and National Lightning Detection Network (NLDN) ground flash data to provide insight into the electrical nature and lightning structure of the two MCSs as they passed within the effective range of the Houston LDAR network, which is less than 130 km according to Ely et al. (2007).

2.1 Radar Data

The Level-II WSR-88D reflectivity data from KHGX, which are available from the National Climatic Data Center (NCDC), are used to analyze the reflectivity structure of two LLTS MCSs that traversed Houston on 31 October 2005 and 21 April 2006. WSR-88Ds are S-band (10 cm) radars that provide radar reflectivity within a range of 230 km from the radar and both mean radial velocity and velocity spectrum width within a range of 115 km. The spatial resolution of reflectivity is 0.95° by 1 km (Crum et al. 1993). The radars continually make 360° azimuthal sweeps at increasing elevation angles. When the radar cycles through a complete set of elevation angles, the set of sweeps is called a volume scan. There are currently two volume coverage patterns (VCPs) that are primarily used for convective weather, VCP 21 (Fig. 2.1) and VCP-11 (Fig. 2.2). VCP-21 makes 11 sweeps at 9 different angles between 0.5° and 19.5° and

takes 6 minutes to complete the volume scan. On the other hand, VCP-11 makes 16 sweeps at 14 separate elevation angles between 0.5° and 19.5° and only takes 5 minutes to complete. VCP-11 is commonly used for severe weather because it provides more complete vertical and temporal coverage of storms by containing more elevation scans at levels greater than 5° and having a faster turnaround time (Brown et al. 2000). Due to the maximum elevation scan of 19.5° , neither VCP is able to scan the tops of storms within around 25 km of the radar. This area is called the “cone of silence” because no data is detected. However, due to the large horizontal size (> 100 km) of the MCSs, the cone of silence has a negligible effect on the analyzed radar properties. As the MCSs passed within range, KHGX was operating under VCP-11 in severe weather mode.

2.1.1 Radar Reflectivity

Radar reflectivity is the measure of power returned to the radar by a backscattering target and is influenced by the size, shape, number, aspect, and dielectric constant of the target (Rinehart 2004). Radar reflectivity factor (z) is defined as:

$$z = CPR^2/|K|^2 \quad (2.1)$$

where C is a radar constant, P is the transmitted power, R is the distance to the target, and K is function of the complex index of refraction of the target. The values of $|K|^2$ for ice and water are 0.197 and 0.93 respectively. The equivalent radar reflectivity is estimated by radar when it is assumed that the backscattering hydrometeors are spherical and composed of water in the radar range equation. Therefore, the equivalent radar reflectivity factor for ice (z_i) in terms of the radar reflectivity of water (z_w) is:

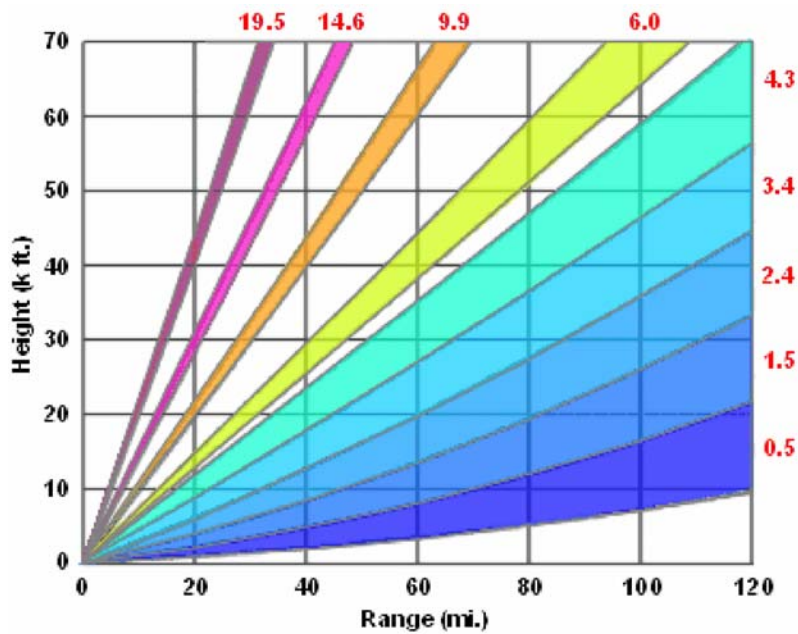


FIG 2.1: WSR 88D volume coverage pattern 21 (VCP 21).
 (<http://www.srh.noaa.gov/radar/radinfo/vcp21.gif>)

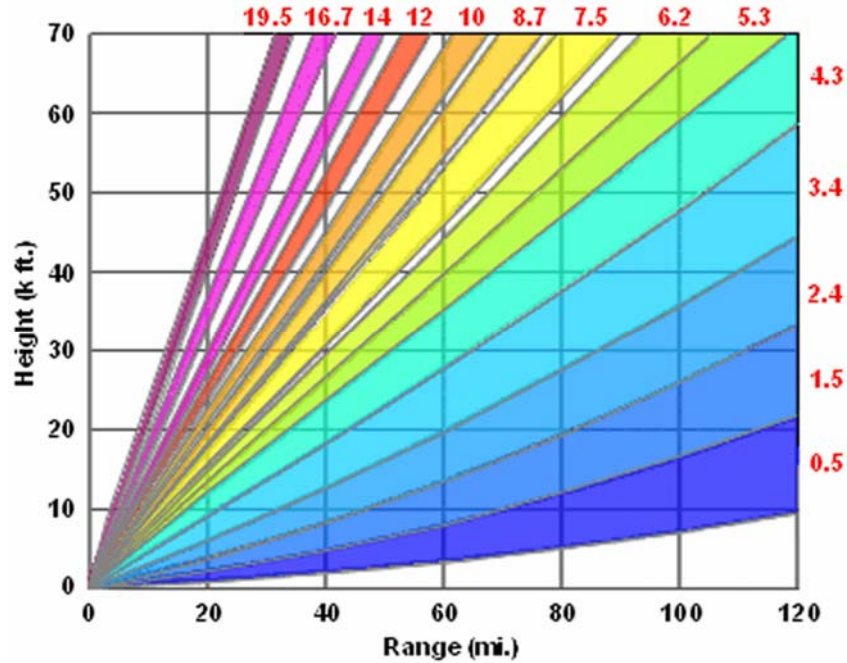


FIG 2.2: WSR-88D volume coverage pattern 11 (VCP 11).
 (<http://www.srh.noaa.gov/radar/radinfo/vcp11.gif>)

$$z_i = (|K_i| / |K_w|) z_w = 0.223z. \quad (2.2)$$

Radar reflectivity is usually expressed in decibel units (dB) as follows:

$$\text{dBZ} = 10\log_{10}(z). \quad (2.3)$$

Therefore, as ice melts to water, the radar reflectivity increases to:

$$\text{dBZ}(\text{water}) = \text{dBZ}(\text{ice}) + 6.5\text{dB}. \quad (2.4)$$

This process plays a profound role in the creation of the bright band as mentioned in section 1.2.3. The radar reflectivity factor may also be expressed as:

$$z = \int_0^{\infty} D^6 N(D) dD \quad (2.5)$$

Where D is the particle diameter and $N(D)$ is the particle size distribution such that $N(D)dD$ is the number of particles of size D in a volume. Note that radar reflectivity is highly correlated with particle size. For example, small raindrops yield a much lower reflectivity than large hailstones.

2.1.2 Analysis Techniques

Using REORDER software (Oye and Case 1992), radar reflectivity data are converted from radar coordinates to Cartesian coordinates with a horizontal and vertical grid spacing of 1.0 km to ensure high resolution data. The vertical gridding starts at 0.3 km and ends at 17.3 km, for 18 unique elevations. Interpolation was accomplished with

a Cressman weighting scheme (Cressman 1959). The Cressman scheme places more significance on radar values that are closer to the grid point by calculating a weighted mean of nearby radar gates at each grid point. The weighting function (W) is a function of the distance r between the data at an individual radar gate and the grid point and the radius of influence R according to

$$W = \frac{R^2 - r^2}{R^2 + r^2} \quad (2.8)$$

After multiple tests, a horizontal and vertical radius of influence of 2.0 km is used to ensure data coverage and resolution, especially at higher elevations. After the radar was converted to Cartesian coordinates, several Interactive Data Language (IDL) programs were employed to read in the gridded data and perform analysis.

2.1.2.1 Partitioning the Data

A major focus of this study is to examine the contributions the convective and stratiform regions have on MCS structure and evolution. Therefore, the two regions must be separated and defined. Two possible ways of partitioning the convective and stratiform regions were considered: (1) the automated (objective) two-dimensional reflectivity texture method summarized by Steiner et al. (1995) and (2) the manual (subjective) partitioning approach based on the known three dimensional reflectivity structure of the convective and stratiform regions in a LLTS MCS (e.g., Houze et al. 1990). The Steiner et al. (1995) partitioning method uses a combination of three reflectivity based thresholds on a horizontal plane at a low altitude (e.g., 2 km) to classify the precipitation type. First, any grid points characterized by reflectivity values

≥ 40 dBZ are automatically classified as convective. Second, if a large reflectivity gradient exists within a certain background reflectivity, those grid points are also classified as convective. Third, if any nearby grid points are within certain radii of convectively labeled grid points, they are also labeled as convective. Any reflectivity values not classified as convective are classified as stratiform. The Steiner et al. (1995) method has a tendency to mis-classify enhanced reflectivities in the stratiform region as convective and also lower convective reflectivities (especially on the leading edge of convection) as stratiform (McCormick 2003). On the other hand, subjective partitioning uses a straight line between the convective and stratiform regions to separate the two regions. Therefore, the only associated errors are in the transition between the two regions, where a non-linear boundary is represented by a straight line. The subjective partitioning method is used in this study because it is simple to implement for a small number of radar volumes and typically reduces bias in the classification of echo, particularly in stratiform regions with enhanced reflectivity.

In order to partition the MCS regions, the reflectivity data, along with LDAR VHF source data, are first rotated about the center of the LDAR network, where the convective line is parallel to the y-axis and line normal direction is parallel to the x-axis. The analysis region is then confined by the region determined by the LDAR source density plots, since its effective range is less than that of the radar. Radar reflectivity data are then subjectively partitioned into three separate regions (convective, transition, and stratiform) according to their location relative to the MCS radar reflectivity structure in the horizontal and vertical (e.g., Houze et al. 1990). An example of the partitioned

stratiform, transition, and convective regions is shown in Fig. 2.3. The convective leading line is composed of a continuous series of intense reflectivity cells oriented from the southwest to the northeast with a strong reflectivity gradient at the front of the line. The stratiform region consists of a secondary maximum of reflectivity values (30 – 40 dBZ for 31 Oct. MCS, 35-45 dBZ for 21 Apr. MCS) that is found rearward of the convective line. The transition zone, a region of minimum reflectivity values (20- 30 dBZ for 31 Oct. MCS, 25-35dBZ for Apr. MCS), separates the convective and stratiform regions. Using these guidelines, two straight lines, parallel to the leading convective line, are used to separate these three regions. Next, another parallel line is used to further sub-partition the stratiform region in the line-perpendicular domain to only go as far rearward as the detectable LDAR VHF sources. The convective region is also sub-partitioned by a parallel line in the line perpendicular domain to begin at the sharp reflectivity gradient at the leading edge of the line.

2.1.2.2 Contoured Frequency by Altitude Diagrams (CFADs)

The vertical structures of reflectivity for the defined convective and stratiform regions are then analyzed by using mean profiles and reflectivity contoured frequency by altitude diagrams (CFADs) (Yuter and Houze 1995). In CFADs, reflectivity values are along the x-axis and height is along the y-axis; therefore, reflectivity is stratified by altitude only and the horizontal locations are ignored. The contours in the CFADs represent the percentage of points per unit variable (dBZ in this case) per kilometer and not merely the percentage of points. The frequency distribution of reflectivity may be

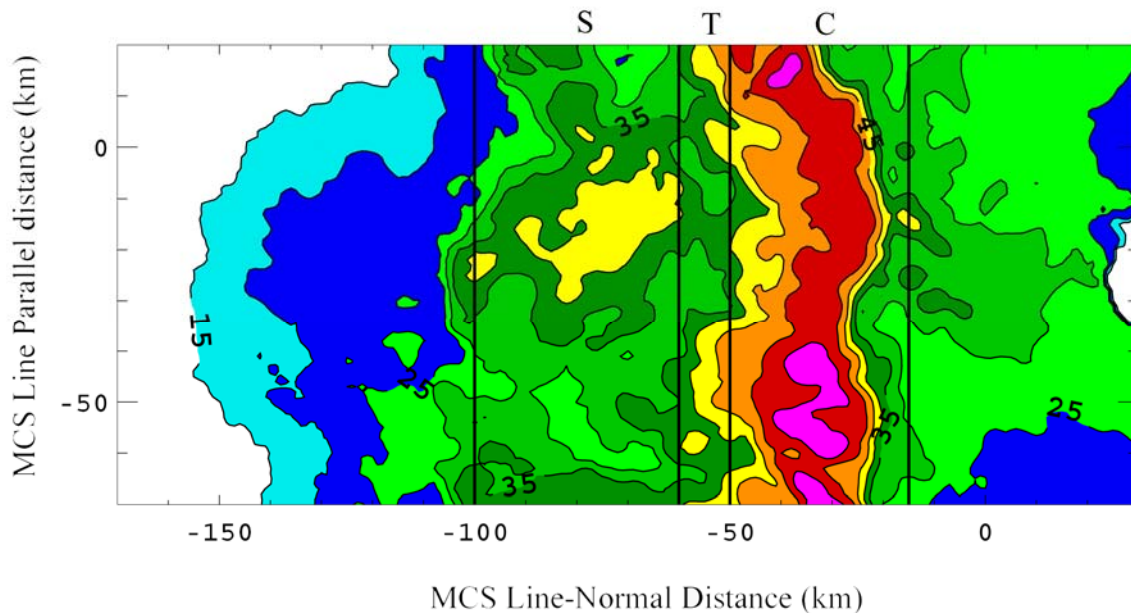


FIG. 2.3: An example of subjective partitioning of the 21 April 2006 MCS. Radar reflectivity values (dBZ) are contoured every 5 dBZ with every other contour labeled. Radar reflectivity shown is the maximum reflectivity throughout all vertical levels. Straight vertical lines indicate the partitioning used to separate the convective (C), transition (T), and stratiform (S) regions. See text for partitioning methods.

evaluated by comparing contour patterns between the same levels at different times and between different levels at the same time. CFADs provide a concise summary of the relative frequency of radar reflectivity with height and extend what is generally available from a single mean profile or cross-section (Yuter and Houze 1995).

2.1.2.3 Rainfall Totals

Radar reflectivity is often used to estimate rainfall rates. However, there are many errors that can be associated with reflectivity and rain rate (z-R) relationships. Such errors could be caused by power calibration errors, beam attenuation, horizontal

winds, bright band, rain rate variations, vertical air motions (updrafts or downdrafts), particle size distributions, or beam blockage (e.g., Rinehart 2004). Although these relations may be associated with errors, we use the z-R relations that Uijlenhoet et al. (2003) set forth for convective (2.6) and stratiform (2.7) regions in order to determine the general trends in each region's rainfall rate. In order to obtain the most accurate rain rate, a low level (2 km) elevation is used. This level is more likely to give results based on precipitation actually hitting the ground and is below the effect of the radar bright band. Before these calculations are performed, Z (dBZ) was converted to z ($\text{mm}^6 \text{m}^{-3}$) by the conversion $z = 10^{(Z/10)}$. Once the rain rate was found, total rainfall was calculated by finding the volume of rain that fell during the volume scan time and converting it to water mass (kg).

$$z = 300R^{1.4} \quad (2.6)$$

$$z = 450R^{1.4} \quad (2.7)$$

Calibration errors differ from WSR-88D to WSR-88D and with the same WSR-88D over a period of time (Anagnostou et al. 2001); therefore, the trends of radar reflectivity and calculated rain rates as the MCSs evolve are noted in this study, and not the actual values of these parameters. Rain rates, in addition to CFADs, time series plots of each region's mean reflectivity at varying altitudes, and each region's area are shown to document the evolution of the stratiform and convective regions. Note that the stratiform area used for analysis and comparison with the lightning data is dependent on how far rearward LDAR lightning flashes are detected in the MCS.

2.2 Lightning Detection and Ranging Network

Texas A&M University's Lightning Detection and Ranging (LDAR) network is composed of 12 sensors around the Houston metropolitan area and is used to detect three-dimensional location and time of VHF radiation sources emitted during the electrical discharge of lightning. These sensors can detect IC and the intra-cloud component of CG flashes. The individual sensors are similar to New Mexico Institute of Mining and Technology's Lightning Mapping Array (LMA) described by Rison et al. (1999) and are based off the original LDAR system developed at NASA's Kennedy Space center. Each sensor records the time and magnitude of the maximum pulse during a 100 us interval, allowing the network to record a possible 10,000 sources every second.

The average baseline of the network is 25 km and the diameter of the network is approximately 80 km. The sensors are tuned to a 5 MHz band centered on a frequency between 69 and 71 MHz depending on noise conditions (Rison et al. 1999, Ely et al. 2006). The network employs a time of arrival (TOA) technique that locates sources by differences in the time of arrival of the VHF signal at different sensors. Between two sensors, possible source locations define a hyperbola of constant time difference. With three sensors, two hyperbolas are defined and the intersection of the two hyperbolas is the source location. However, multiple intersections occur for certain source locations and therefore a fourth sensor is needed (Fig. 2.4) (MacGorman and Rust 1998). A minimum of five sensors are required to record a source arrival time in order to determine an accurate 3D source location. Since there are four unknowns ($x, y, z,$ and t),

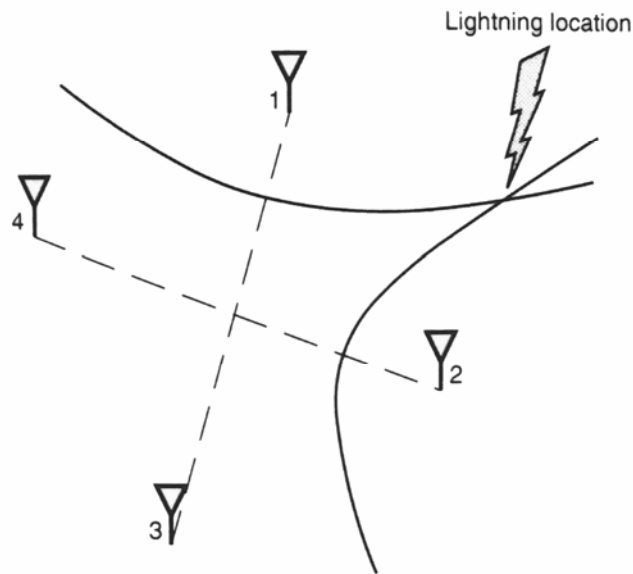


FIG. 2.4: The location of a lightning source based on the time of arrival technique. Hyperbolas on which the source occurs are formed by the difference in times in which the source is detected by two different sensors. The intersection of hyperbolas from multiple pairs of sensors marks the location of a lightning source. Adapted from MacGorman and Rust (1998).

the 5th (or more) sensor provides a redundant solution and improves the accuracy of the time and location of a VHF source in the presence of VHF noise.

During the time of the two cases being analyzed, 10 of the 12 sensors were operational. The two sensors that were not operational were not installed until after the MCS events took place. Ely et al. (2007) tested the network's range during the MCS that traversed the network on 31 October 2006. They found that the detection efficiency of VHF sources dropped off considerably beyond a radial distance of 130 km from the center of the network. Because of the reduced detection efficiency, this study will only consider VHF sources that are within ~100 km from the center of the network, well

within the network's effective range. During the 31 October MCS, the calculated root mean square (RMS) time error was 80 ns, which led to a 3D location error of approximately 250 m for sources within the network's perimeter and 1 km accuracy out to 100 km from the center of the network (Ely et al. 2007).

The location of these VHF sources provide valuable information on the stratiform and convective charge centers of the MCS since lightning tends to propagate through net charge centers (e.g., Coleman et al. 2003). The source location and time data are recorded for the MCSs that traversed the Houston LDAR network on 31 October 2006 and 21 April 2007. The VHF sources used in this study are located in the stratiform and convective regions along a segment of the convective line that was relatively straight for 100 (90) km for the 31 Oct. 2005 (21 Apr. 2006) event. Analysis over a relatively straight convective line is important in determining possible particle and charge advection by the front-to-rear flow from the convective line and into the stratiform region.

2.2.1 VHF Source Density Plots

In order to make VHF source density plots comparable to those seen in previous work (e.g., Carey et al. 2005), the VHF lightning source data are grouped into 10 minute intervals, centered on the KHGX radar volume scan times. As mentioned section 2.1.2.1, both the radar reflectivity data and VHF source data are then rotated about the center of the LDAR network where the convective line was parallel to the y-axis and line normal was parallel to the x-axis. VHF composite source density and maximum composite radar reflectivity plots are created for three different views: (1) line normal

versus altitude, (2) horizontal plan view, and (3) line parallel versus altitude and overlaid on the corresponding maximum composite radar reflectivity contours. In order to create the line normal vs. altitude (X-Z) view, the VHF source density ($\text{m}^3 \text{min}^{-1}$) is calculated by taking the integral of sources throughout the line parallel extent of the MCS being studied (100 km or 90 km) for the 10 min period and then dividing by the volume of the grid column (100 km^3 or 90 km^3) and also by the time interval in which the sources were taken (10 min). The composite radar reflectivity is determined by the maximum reflectivity in the line parallel grid column.

Similarly, the composite source density for the horizontal (X-Y) plan view is computed by taking the integral of sources throughout the height of the column (17 km) for the 10 min period and dividing by the volume of the grid column (17 km^3) and the integration time (10 min). The composite reflectivity shown is the maximum reflectivity in the vertical grid column. The line parallel versus altitude view was created in much the same way. The composite VHF source density was calculated by adding all the sources throughout the line normal length of the grid column (100 km for both cases) for the 10 min period and dividing by the total line normal grid column volume (100 km^3) and the integration time (10 min). The composite reflectivity shown is the maximum reflectivity in the line normal grid column. These views give insight into the lightning pathway for a portion of the MCS that remained within the effective range of the LDAR network during the analysis times and where the convective line remained relatively straight.

2.2.2 Flash Algorithm

In order to obtain flash characteristics for each region of the MCS, a modified version of a NASA flash algorithm is used to group individual VHF sources into flashes based on temporal and spatial restraints. The algorithm requirements of a flash are as follows: the maximum time duration of a flash is 3 seconds, the maximum time delay between a source already associated with a flash and a new source is 0.5 seconds, and the maximum distance between a new source and an already determined flash source is 5 km. The algorithm also indicates flash branching. If a new source is within 0.03 seconds and 5 km of an already indicated flash source, then the new source is considered part of the same branch of the flash source. If the time lag between sources is greater than 0.03 seconds, but less than 0.5 seconds, and the new source is within 5 km of another determined flash source, then a new branch is created. If the time lag between sources is greater than 0.5 seconds or the distance between the last determined flash source and the new source is greater than 5 km, then a new flash begins. Flashes that contained less than 3 sources are considered poorly located events that are either part of other, larger flashes or background noise and are not counted as flashes. The analysis domain is within the effective range of the LDAR network and very few flash events recorded had less than 3 sources.

Once all the VHS sources are combined into flashes, flash characteristics are determined for each MCS region. Flashes are grouped in ten minute intervals centered on the radar scan times. Flash rates are then calculated for each region by counting the number of flashes that propagated through the region and dividing by 10 minutes. Also,

flash rates for the number of flashes initiating in each region were also determined by adding all original (i.e., first) VHF source signals of a flash in each region. These flash rates give clues into how electrified each MCS region is and whether or not flashes are originating in one region (e.g., convective) and propagating into another region (e.g., stratiform). Along with flash rates, mean flash extent and mean VHF source count of flashes initiating in their respective regions are found. The flash extent is calculated by taking the largest three-dimensional distance between any two sources of the flash. These characteristics are displayed in times series plots and compared with reflectivity data throughout the analysis time domain.

As well as source density plots, individual flashes are also plotted as a series of individual VHF sources (or dots) on the same views as mentioned above. These flashes are used to validate the lightning pathway as seen in the VHF source density distribution and also to determine flash characteristics. Examples of these flashes are shown in the next section. Line normal vs. altitude, line-parallel vs. altitude, and horizontal plan views are created by plotting all the individual sources throughout the analysis domain on a 2-D plane of the respective view. The radar reflectivities in these plots are created in the same way mentioned in the source density plots. A time-height plot is shown and indicates the height of sources with time. The sources are color coded with increasing time, and the respective colors are used throughout all views. Also, a histogram of sources with height is shown. All these views are combined to produce one 5-panel plot of individual flashes. These plots of individual flashes help confirm the VHF source density plots mentioned above as lightning pathways and also may help distinguish

separate charge layers in the thunderstorm due to the breakdown of negative charge in a positive charge region being noisier than breakdown of positive charge in a negative charge region (e.g., Rison et al. 1999). The flash rate of both the convective and stratiform regions is calculated and used as a measure of the electrical strength of the region because flash rate is directly proportional to thunderstorm electrical power (Vonnegut 1963, Boccippio 2002) and also because the flash detection efficiency decreases less rapidly than source detection efficiency with increasing distance from the LDAR network center.

2.3 National Lightning Detection Network

The National Lightning Detection Network (NLDN) has been detecting CG lightning flashes since 1989 (Orville 1991). The network originally consisted of magnetic direction finders, but has recently been upgraded to use a combination of TOA and Magnetic Direction Finding (MDF) technology and consists of 106 sensors. The new method for combining the two technologies is referred to as the improved accuracy from combine technology (IMPACT) method (Cummins et al. 2006).

MDF sensors calculate the location of CG flashes by the ratio of signal strengths recorded simultaneously at multiple MDF sites. The sensors are composed of two vertically looped antennas that are mounted perpendicular to each other. The direction of a lightning flash is calculated by the ratio of electromagnetic signals radiated by lightning from two orthogonal magnetic loop antennas. The location of the flash may be found by finding the intersection of the directions from multiple sensors (Fig. 2.5) (Krider et al. 1980, MacGorman and Rust 1998).

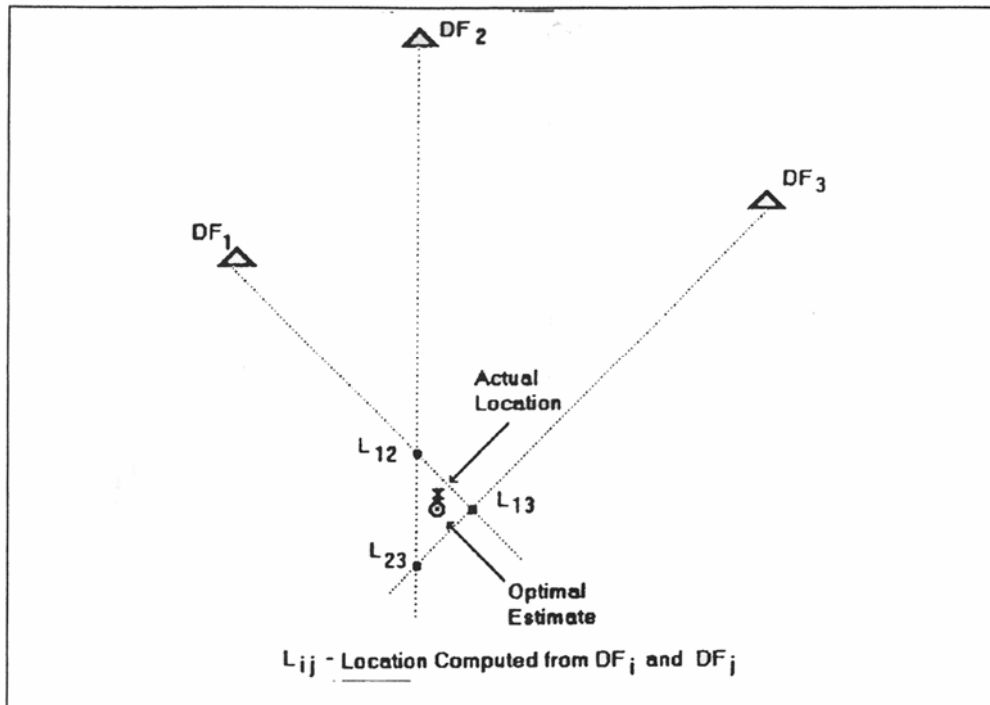


FIG. 2.5: A network consisting of 3 direction finding sensors determine the location of a lightning strike. An optimal location algorithm is used to minimize the azimuthal errors. Adapted from Cummins et al. (1993).

Using a combination of these sensors, NLDN detects the time, location, polarity, multiplicity, and peak current of CG flashes. NLDN groups individual strokes into flashes based on temporal and spatial clustering. For up to 1 second after the first return stroke, a maximum of 14 additional strokes will be added to the flash if they are within 10 km from the first stroke and 500 ms from the previous stroke. The reported location, polarity, and peak current of the flash is based on the first return stroke. NLDN has a location accuracy of 500 m and flash detection efficiency of 90% across the United States (Cummins et al. 1998).

For this study, NLDN flashes with positive peak currents less than 10 kA are discarded because they could be misidentified IC flashes (Cummins et al. 1998, Wacker

and Orville 1999). NLDN flash rates and characteristics are found for the defined convective and stratiform regions of the MCS and grouped into ten minute time segments centered on radar volume scan times. The evolution of NLDN flash characteristics such as flash rate, percent positive flashes, IC:CG ratio, and positive and negative mean peak currents are documented for each region. The IC:CG ratio is calculated by first subtracting the number of NLDN detected CG flashes from LDAR detected flashes to find how many IC flashes occurred. Then, the number of IC flashes are divided by the number of CG flashes to compute the IC:CG ratio. These characteristics are then put in context with each regions evolving radar reflectivity and LDAR flash characteristics in order to gain knowledge of the microphysical and charging aspects of the MCS.

The stroke level data were also acquired from Vaisala, Inc. in order to associate NLDN positive strokes with a parent LDAR detected flash. The stroke level data are used due to its increased temporal accuracy over the flash level data. Stroke level data sees all strokes in a flash with a temporal resolution of microseconds, whereas the flash level data includes the first stroke of a flash with a resolution of one second. The greater temporal resolution will improve associations between NLDN detected positive strokes with parent LDAR flashes. The NLDN positive stroke locations are associated with the nearest LDAR flash, both temporally ($<1s$) and spatially (<20 km). In some cases, there are no VHF sources near (<20 km and <1 s), or there are multiple flashes near the ground strike location make the association ambiguous. Once the NLDN flashes are paired to a parent LDAR flash, they are grouped into three categories based on location:

(1) stratiform, if the location falls within the defined stratiform domain; (2) non-stratiform, if the location falls within the analysis domain, but outside the stratiform region; and (3) outside, if the flash origination falls outside the analysis domain. These groupings are then subdivided by when the flashes occurred, either before or after 2300 (1207 UTC) for the 31 Oct 2005 (21 Apr. 2006) MCS. This time was used because it appeared as a midway point for stratiform development and the evolving lightning pathway. By determining the origin of these LDAR flashes, the locations of the initiation point of the positive CGs are determined. The mean, maximum, and minimum are computed for the LDAR flash VHF source count, along with the maximum LDAR flash extent and NLDN return stroke current for the +CG flashes occurring in the stratiform and non-stratiform categories.

3. RESULTS

3.1 2005 October 31 LLTS MCS

On 2005 October 31, a symmetric LLTS MCS passed within range of Houston's WSR-88D (KHGX) and Texas A&M's LDAR network. The MCS formed near the Oklahoma, Texas border and evolved as it moved southeast toward and into the Gulf of Mexico (Fig. 3.1). As the MCS traversed the LDAR network it underwent significant evolution in both the convective and stratiform regions. The evolution of the partitioned MCS will be analyzed by using radar and total lightning characteristics during a time span of an hour and a half from 22:27 UTC to 22:53 UTC.

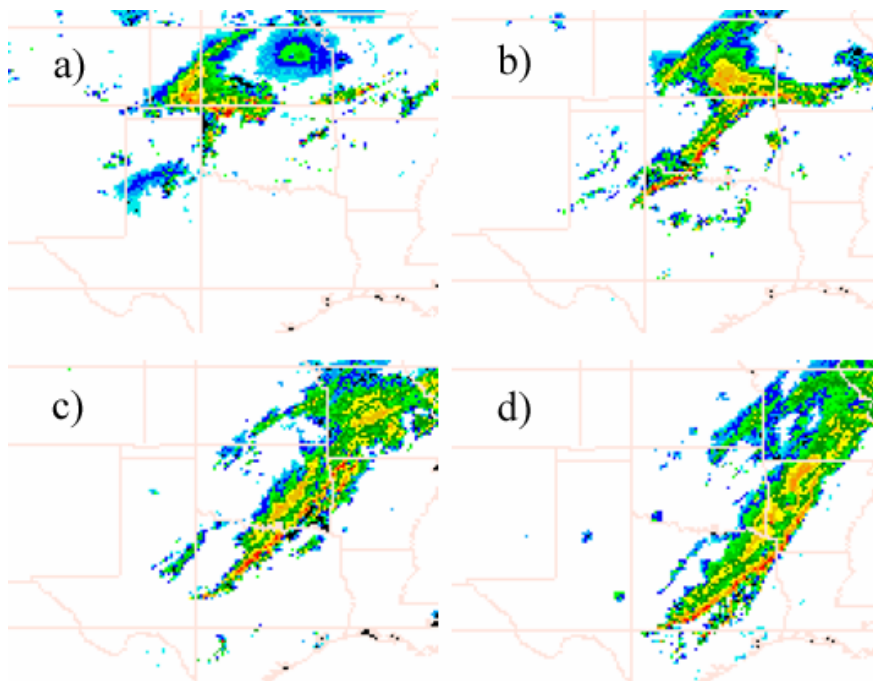


FIG 3.1: NEXRAD reflectivity images of the 31 October MCS at a) 08:00 UTC, b) 12:00 UTC, c) 16:00 UTC, and d) 20:00 UTC.

3.1.1 Radar Reflectivity

Radar reflectivity analysis is used to investigate the evolution of the intensity and structure of the MCS partitioned into convective and stratiform regions (Fig. 3.2). Important features to notice in the horizontal plan view (Fig 3.2) of radar reflectivity are the growth and development of enhanced radar reflectivity (> 35 dBZ). The enhanced areas of reflectivity could be indicative of the development of the radar bright band, which is due to particles melting below the 0°C isotherm. During these radar scans, areas of radar reflectivity > 35 dBZ have grown and areas of 40 dBZ have emerged in the defined stratiform region (Fig. 3.2). It is important to note that the areas of 40 dBZ seen rearward of the stratiform region are a part of a previous convective line that is dissipating due to the formation of the current convective line. The areas associated with the collapsing convective line had no detectable lightning and therefore were not included as part of the defined stratiform region. Also, it is important to determine if the remnants of convective line had any impact on the development of enhanced reflectivity within the defined stratiform region seen in Figs. 3.2c,d. To assist in this determination, the stratiform region was divided into three equal regions extending 0 - 25 km, 25 - 50 km, and 50 - 75 km from the stratiform and transition boundary. Time series of mean reflectivity in Figure 3.3 shows a high reflectivity feature entering and exiting the 50 - 75 km region during the 2238 UTC to 2310 UTC time period. At the time the 40 dBZ feature is exiting the 50 - 75 km region, the 25 - 50 and 0 - 25 km regions exhibit only a slight increase in mean reflectivity values. This suggests that the feature associated with the remnants of prior convection moved out the back end of the analysis area and did not

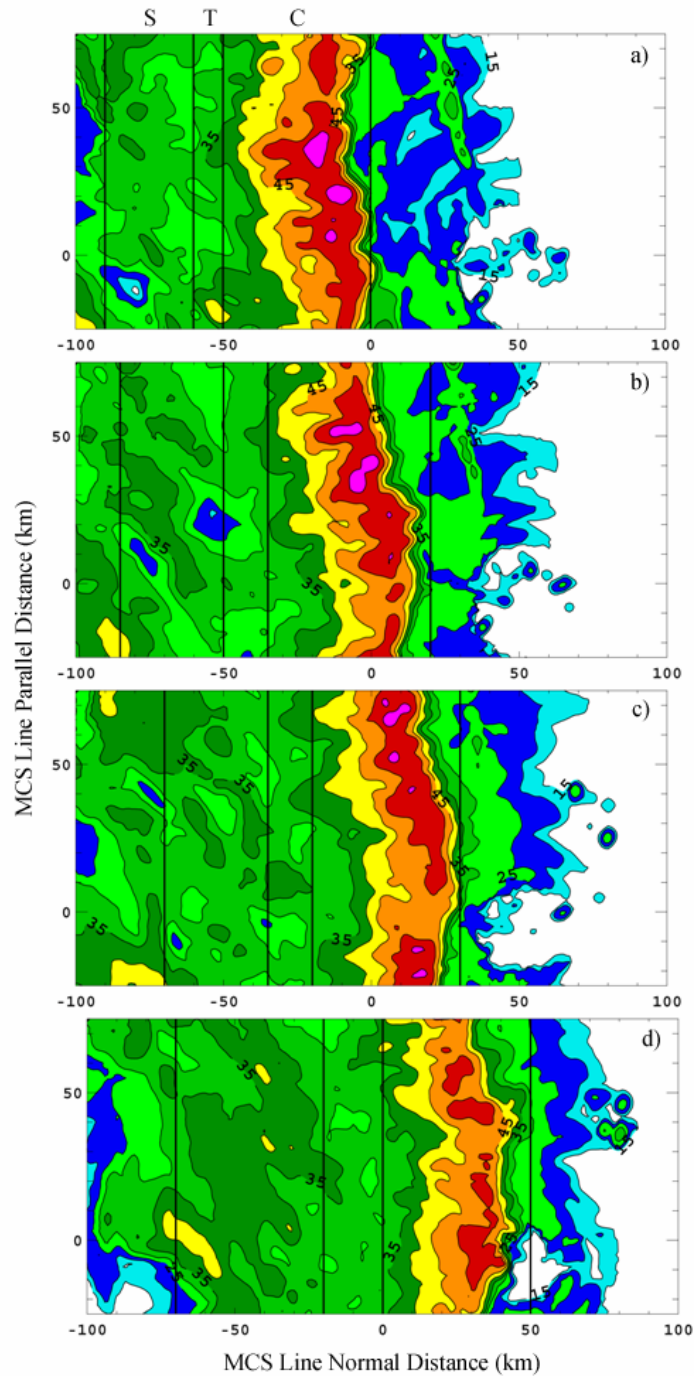


FIG. 3.2: Composite reflectivity images for four different times during the lifetime of the 31 October MCS. The times shown are: a) 22:43 UTC, b) 22:59 UTC, c) 23:15 UTC, and d) 23:32 UTC. Reflectivity is contoured every five dBZ with every other contour labelled (25 dBZ, 35 dBZ, 45 dBZ, 55 dBZ). Warmer colors indicate higher reflectivity values. Vertical solid lines indicate portions of the stratiform (S), transition (T), and convective (C) regions.

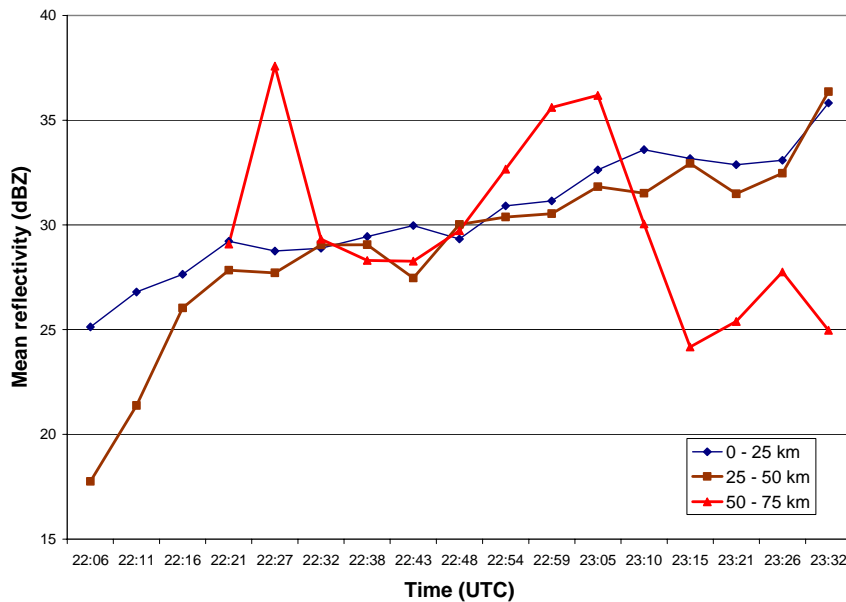


FIG. 3.3: Time series plot of the mean reflectivities (dBZ) in three equally sized areas of the stratiform region. Distance values indicate rearward distance in the stratiform region from the stratiform-transition zone boundary.

have a significant influence on the development of the radar bright band at later times (Figs. 3.2c,d).

A combination of CFADs, time series of reflectivity, and rainfall amounts are used to provide a summary of the MCS evolution. CFADs provide a concise summary of the relative frequency of radar reflectivity values in height and extend what is available from a single mean profile or cross-section (Yuter and Houze 1995). Two CFADs, along with mean profiles, for both the stratiform (Fig. 3.4a) and convective (Fig. 3.4b) regions, are compared against the corresponding LDAR VHF lightning source density displays at critical times in the evolution of the stratiform region lightning

structure. The times shown for both regions are 22:43 UTC and 23:32 UTC, near the beginning and end of the analysis time period.

Similar to Yuter and Houze (1995), the stratiform CFADs show a narrower reflectivity distribution than the CFADs from the convective region, which can serve as an indication of correct stratiform/convective partitioning. According to Fig. 3.4a, as the stratiform region evolves from 22:43 UTC to 23:32 UTC, there is an increase in the frequency of high dBZ values (> 30 dBZ) at low- to mid-levels (< 5 km), which can be associated with the growth of the radar bright band. The formation of the bright band begins with ice crystals being ejected rearward from the convective region by the front-to-rear flow. These ice crystals then fall slowly across the mesoscale updraft and grow by deposition and then by aggregation before they reach the melting level. Upon falling through the melting level, these aggregates melt into raindrops, producing what is called the radar bright band, a band of maximum reflectivity (e.g., Houze et al. 1989).

The bright band development can be shown by the increase in relative frequency of high reflectivity values found between the heights of 2 and 5 km. At 3 km from 22:43 to 23:32 UTC, the upper limit of the 1% contour changes from 41 dBZ to 45 dBZ (Fig. 3.4a) and the lower limit of the 1% contour changes from 15 dBZ to 10 dBZ. These results indicate that the stratiform CFAD is broadening from 22:43 UTC to 23:32 UTC as the upper (lower) tails increase (decrease). The increase in mean reflectivities is therefore a result of the increase in the upper tail. The decrease of the lower tail is possibly due to the development of the stratiform region. A similar increase in the mean stratiform region radar reflectivity with time can also be noted in Fig. 3.2. Also,

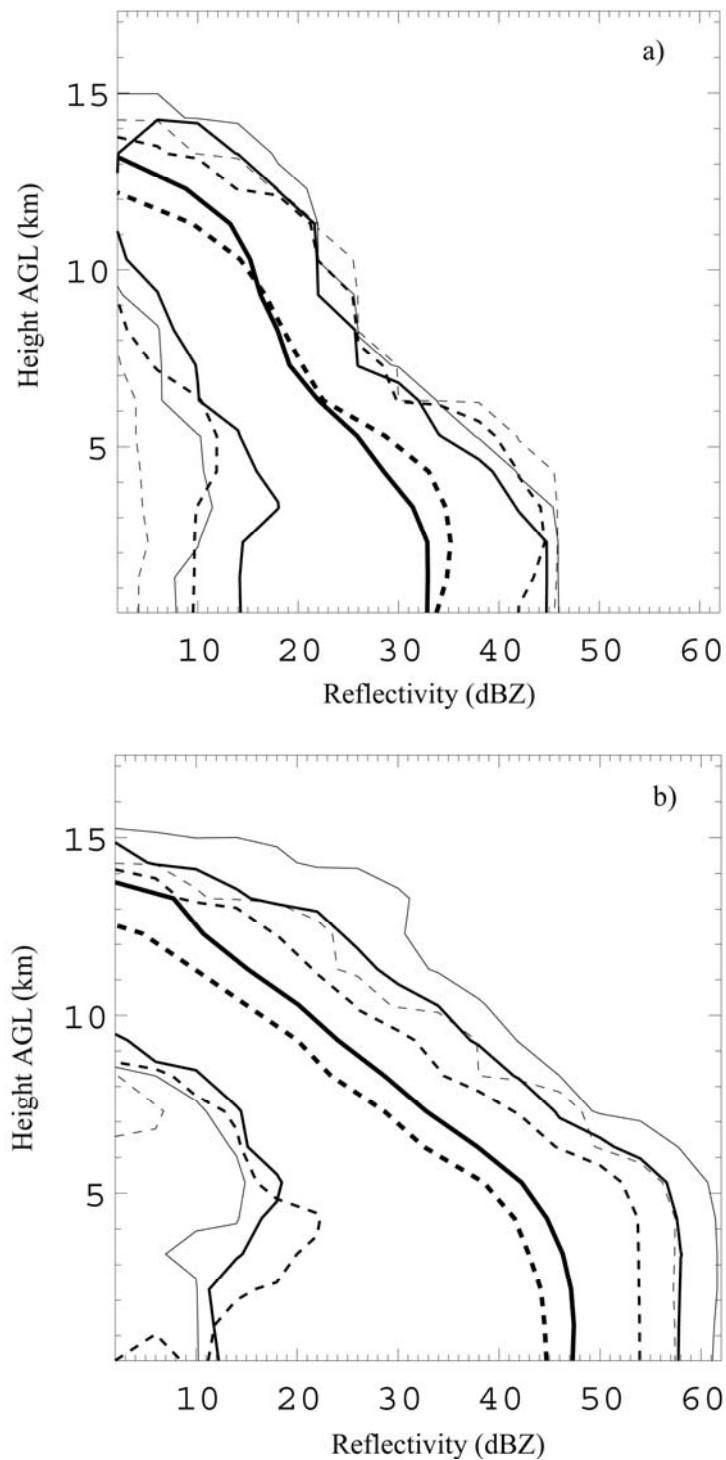


FIG. 3.4: Contoured frequency by altitude diagrams (CFADs) and mean profiles of radar reflectivity for the 31 October MCS a) stratiform and b) convective regions for 22:43 UTC (solid) and 23:32 UTC (dashed). The bin size was set to 4 dBZ and the displayed contours are 0.1% data $\text{dBZ}^{-1} \text{km}^{-1}$ (gray), 1% data $\text{dBZ}^{-1} \text{km}^{-1}$ (black), and the mean dBZ (bold).

reflectivities decrease at higher elevations. For example, the 1% contour decreases from 20 dBZ to 15 dBZ from 22:43 UTC to 23:32 UTC at 13 km. Therefore, the height of moderate reflectivities in the stratiform is lowering during this time period. However, it is noted that the percentage of available data points from the maximum number of points decreases with height to below 20% above 13 km and therefore may not be representative of storm structure.. According to Fig. 3.4b, the largest reflectivity values of the convective region decreased significantly with time, a sign that the convective line is weakening. For example, high dBZ values of 58 - 61 were present throughout the lower levels at 22:43 UTC and were absent by 23:32 UTC (Fig. 3.4b). The mean radar reflectivity decreased by 2 to 4 dB through the entire vertical depth of the convective region from 22:43 UTC to 23:32 UTC.

In addition to the CFADs, time series of mean reflectivities at all heights are shown for the stratiform (Fig. 3.5a) and convective (Fig 3.5b). Reflectivities in the stratiform region at low-to-mid levels (< 8 km) increase steadily throughout the analysis time period. Mean reflectivities of 20 dBZ, 25 dBZ, and 30 dBZ are found at 7 km, 5.5 km, and 3 km, respectively, at 22:27 dBZ. As the MCS matures, the mean reflectivity values of 20 dBZ, 25 dBZ, and 30 dBZ are found at higher heights of 8km, 6 km, and 5 km, respectively, at 23:53 UTC. Also, the emergence of higher reflectivities (> 35 dBZ) is found at 23:32 UTC at low levels (< 3 km). Again, higher reflectivities seen at low- to mid-levels as the system matures could be the result of particle growth by aggregation and deposition as they slowly sink through the mesoscale updraft toward the melting level after being ejected into the stratiform region from the rear of the convective region.

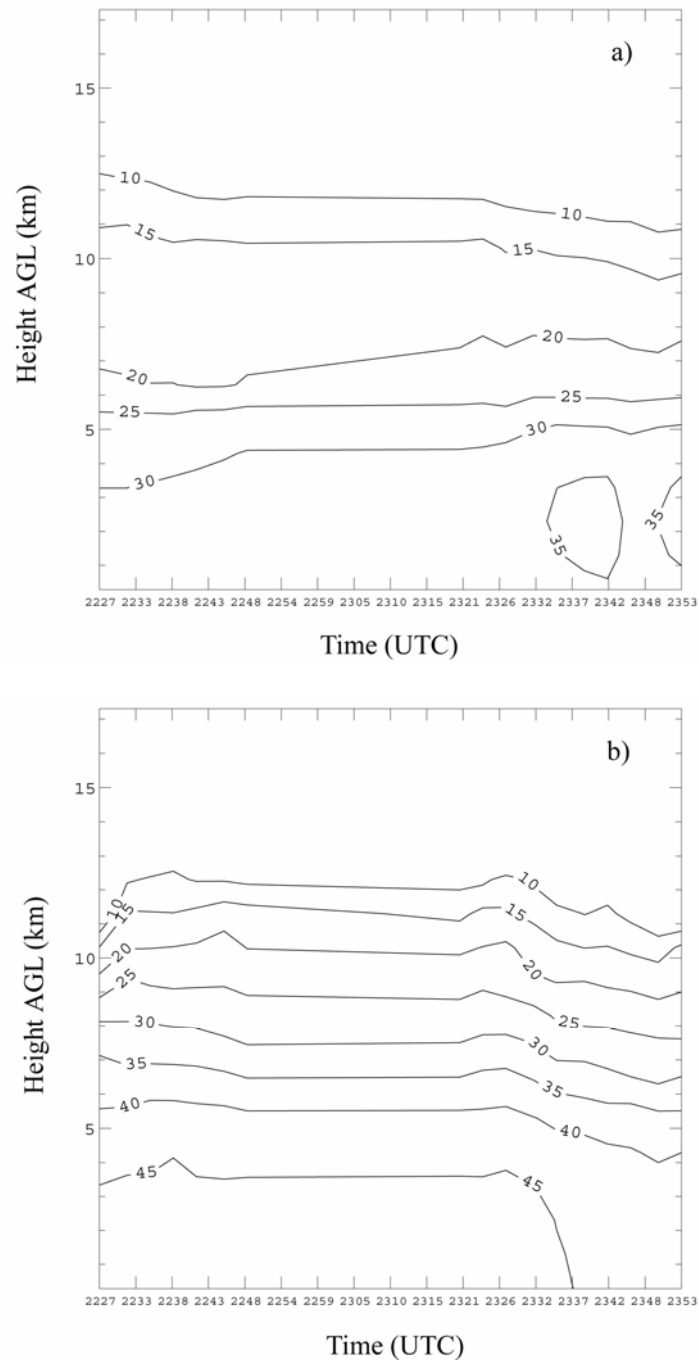


FIG. 3.5: Time series of mean reflectivities at all elevations for the a) stratiform and b) convective regions of the 31 October MCS. Mean reflectivity is contoured every 5dBZ from 10 dBZ to 55 dBZ.

The sinking motion can be illustrated by the slow decrease in low reflectivities at higher elevations (10-13 km) (Fig. 3.5a). Reflectivity values greater than 10 dBZ are seen near the altitude of 12.5 km initially. However, these reflectivity values are only seen below 11 km at later times. As the reflectivity at higher heights in the stratiform region of the MCS decrease, low-to-mid levels see a significant increase in reflectivity.

The convective region on the other hand, shows an increase of mean reflectivity values at most elevations until 22:38 UTC, followed by little change throughout all heights until 23:26 UTC. After 23:26 UTC, the convective region begins to lose intensity rapidly (Fig 3.5b). The increase in reflectivities initially is shown by the reflectivities shifting from lower to higher heights, indicating a possibly of strengthening updrafts. These stronger updrafts would be able to carry particles to higher levels and also able to support larger ice particle formation such as graupel and hail. As the reflectivity values begin to sink down to lower altitudes, this could signify weakening of the updraft, causing larger ice particles to fall lower in the cloud and then to the ground.

To corroborate these findings, time series of mean reflectivities at a height of 4.3 km for the stratiform and convective regions were plotted along with the defined areas of each region (Fig. 3.6). This height was chosen because of its proximity to the melting level during the time of the MCS. As shown, the stratiform mean reflectivity at 4.3 km intensified in time rather steadily, increasing by 8 dB from 22:27 UTC to 23:53 UTC. Not only did the stratiform mean reflectivity increase significantly, its area also expanded from 1200 km² to 7000 km² during the analysis time period. The convective mean reflectivity shows a peak in intensity at 22:43 UTC and weakening beyond 23:32

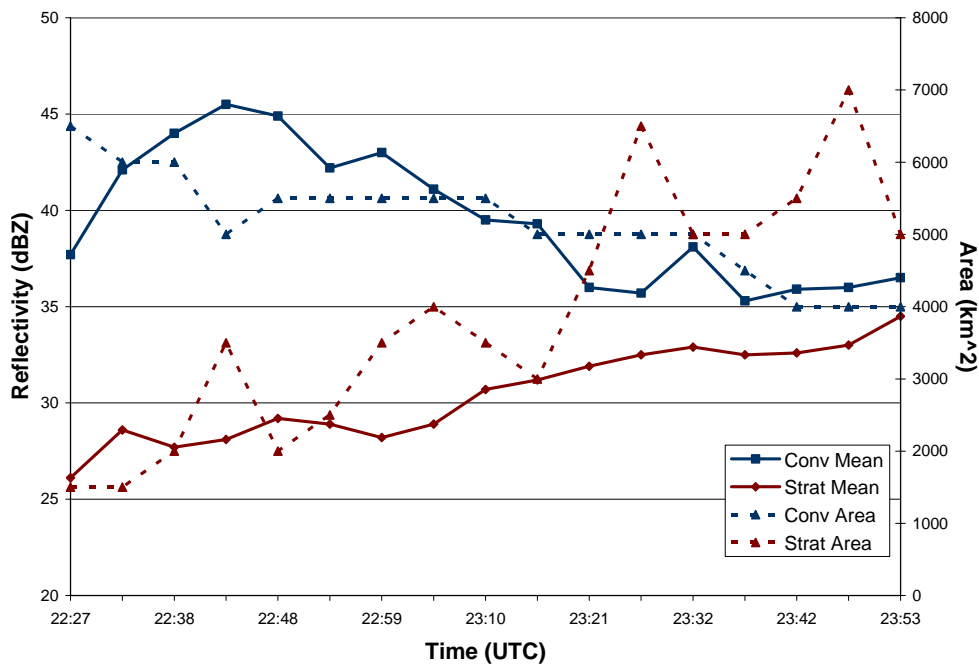


FIG. 3.6: Time series plot of the mean stratiform and convective reflectivities of the 31 October MCS at a height of 4.3 km. Also plotted are the areas of the stratiform and convective regions.

UTC. The convective area decreased in time, which is expected with a decrease in the intensity.

Rain amounts were also determined by calculating the mass of rain that fell during each radar volume scan time for both stratiform and convective regions (Fig. 3.7). The stratiform (convective) region rain amounts increase (decrease) steadily during the analysis time period. Each region's rainfall trend is in agreement with the previous analyses of stratiform region intensification and weakening of convective region with time.

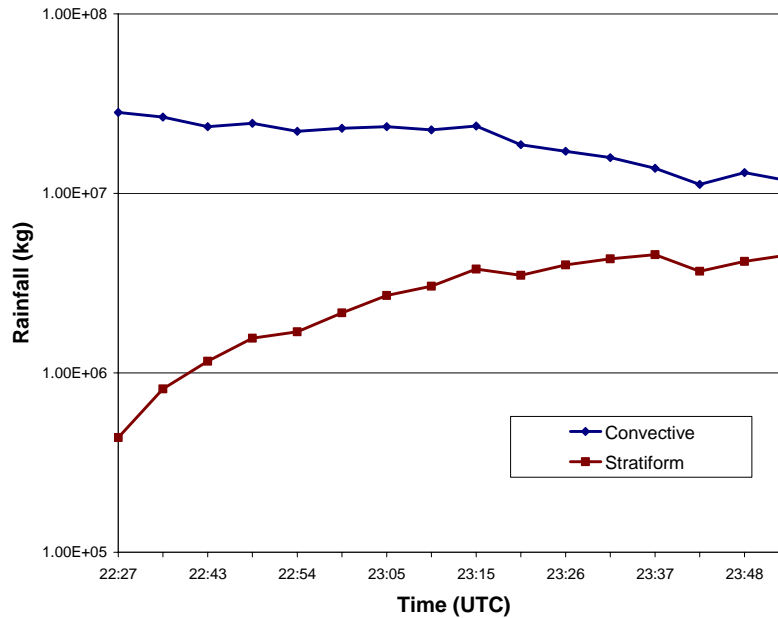


FIG. 3.7: Time series plot of the radar derived rainfall totals that fell under the 31 October MCS convective and stratiform regions during the time span of each volume scan.

3.1.2 Total Lightning

Along with radar reflectivity, the total lightning structure evolved as the MCS traversed the LDAR network within its effective range. The following two sections give insight into the evolving structure based on LDAR and NLDN data.

3.1.2.1 Lightning Detection and Ranging (LDAR)

Ten minute LDAR source density plots are overlaid on composite contoured reflectivity for several different times: 22:43 UTC, 22:59 UTC, 23:15 UTC, and 23:32 UTC. All four times show a maximum source density toward the rear of the convection at a height 8 – 10 km, with a secondary maximum seen below, near 4-5 km (Fig 3.8).

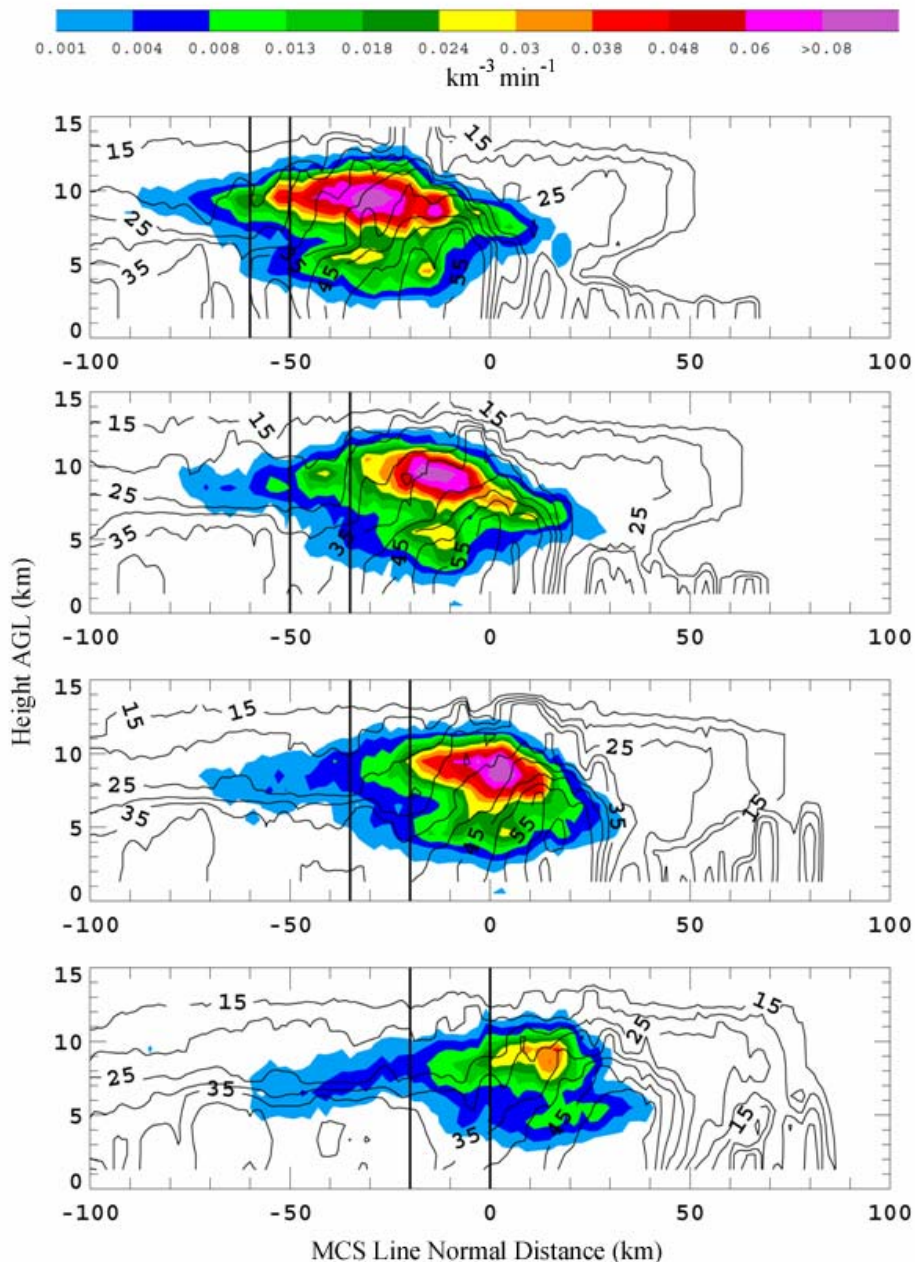


FIG. 3.8: VHF source density (color filled) and composite radar reflectivity (contoured) line normal vs. vertical cross-section plots for 4 different times during the evolution of the 31 October 2005 MCS. The times shown are: a) 22:43 UTC, b) 22:59 UTC, c) 23:15 UTC, and d) 23:32 UTC. Solid vertical lines indicate the applied partitioning method between the convective and stratiform regions. VHF source densities were taken over a 10 minute interval centered on the radar volume start time indicated. Resolution in the vertical (horizontal) is 1 km (2 km).

Since negative breakdown in a positive region is noisier than positive breakdown in a negative region, the layered maximum source densities with a minimum source density between could be indicative of the tripole storm charge structure (Carey et al. 2005). The line normal versus height cross section results (Fig. 3.8) show an evolving lightning pathway. At earlier times (Fig. 3.8ab), the lightning pathway extends horizontally rearward by 40 - 50 km from the top of the convection into the stratiform region at a steady altitude between 8 km and 11 km. As the MCS matures, the lightning pathway evolves such that it slants downward by 5 km and rearward by 40 km from the top of the convection at 10 km altitude through the transition zone toward the radar bright band in the stratiform region. Once over the stratiform bright band, the lightning levels off and extends further, horizontally back into the stratiform region at a height of 5 km (Fig. 3.8cd). The descent of the pathway levels off just above the melting level and the radar bright band. Also, note during these time steps the increasing area of the 35 dBZ and 40 dBZ contours in the stratiform region (Fig. 3.8a-d). This increase in area may also be seen in Fig. 3.2a-d.

The path of individual flashes can be assumed because of the short time scale (10 min). Many flashes originating in the convective and transition regions follow the pathway shown at the different times. Fig. 3.9(3.10) shows individual VHF sources associated with an example flash from a time period early (late) in the MCS evolution. The flash that occurred at 22:38 UTC (Fig. 3.9) is representative of the 22:43 UTC source density plot (Fig. 3.8a). The flash first extends parallel to the convective line before propagating rearward into the stratiform region (Fig. 3.9d). The main source

distribution of the flash remains at a constant height of 8 – 11 km as it extends from the convective region into the stratiform region (Fig. 3.9a,b,c,e). There is also secondary maximum of sources found at a height of 4 -6 km throughout the flash extent. These two maximum in sources produce a layered flash structure as seen distinctly in Figs. 3.9a,e. A flash representative of the lightning pathway during the time period of 23:32 UTC (Fig. 3.8d) is shown in Fig. 3.10. The majority of sources in this flash begin in the convective region near a height of 8 – 11 km, then slant rearward and downward into the convective region (Fig. 3.10d). This flash appears less layered as it propagates from the top of the convective region to lower heights within the stratiform region. Although these flashes are representative of the time period, not all flashes follow the same pathway. Flashes originating in the stratiform region also contribute to the leveling off appearance of the source densities in the stratiform region.

A modified version of a NASA flash algorithm is used to group individual LDAR sources into flashes. Using the algorithm, flash counts are made of all flashes entering the stratiform region. Total flash rates in the stratiform region doubled from 1.5- 2 flashes min^{-1} to over 3 – 4 flashes min^{-1} during the analysis time period (Fig. 3.11). The maximum increase is seen after 23:15 UTC as the lightning pathway begins to slant downward toward the melting level. These flashes are then classified based on where they originated from. The flashes were first classified as to whether or not they originated in the analysis domain consisting of the defined convective, transition, and stratiform regions. Throughout all times, a mean of 80% of stratiform flashes originated within the analysis domain (Fig. 3.12). This would indicate that few flashes propagate

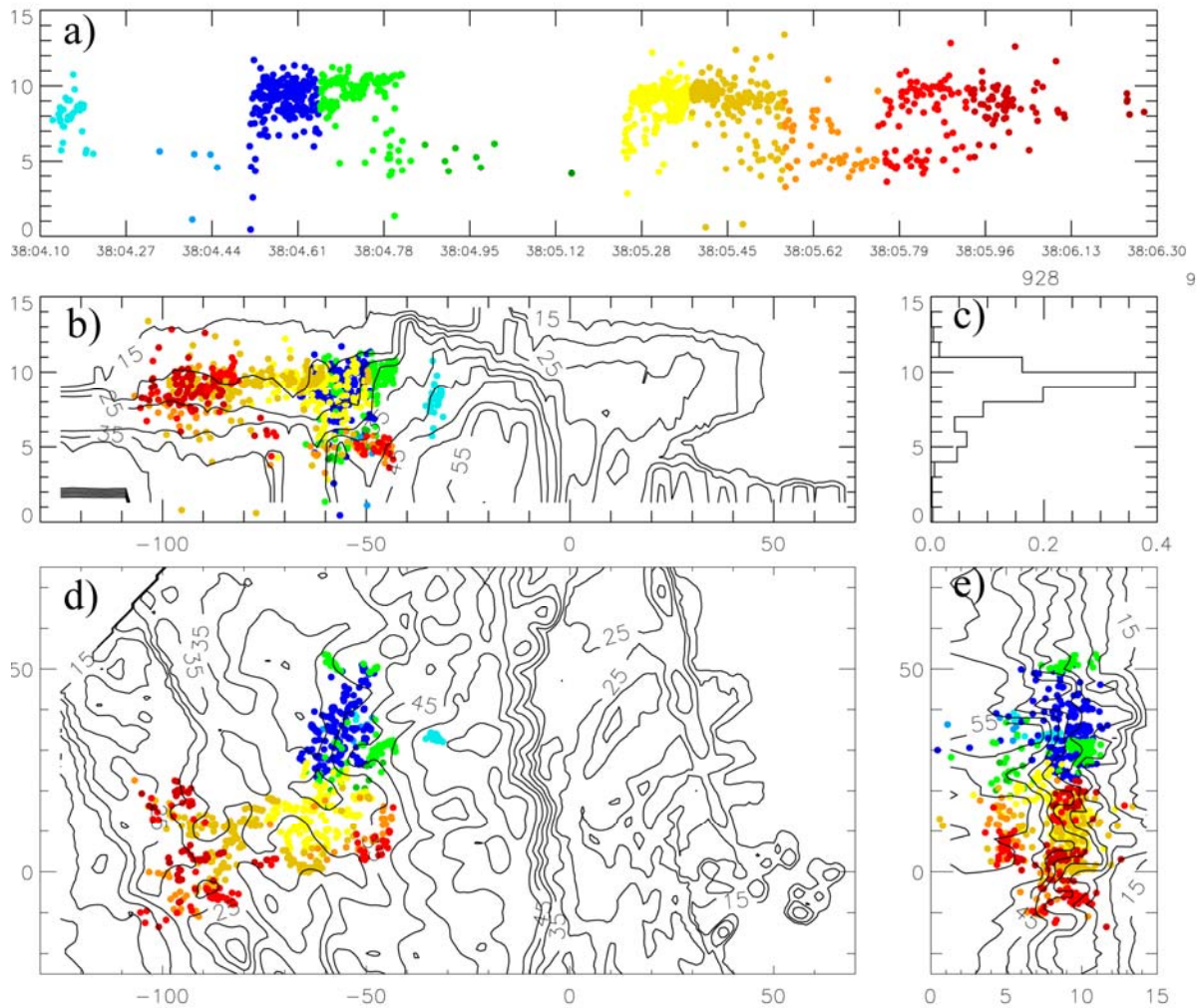


FIG. 3.9: Plot of VHF lightning sources (color coded with respect to time) and composite reflectivity associated with a representative flash that occurred on 31 October at 22:38 UTC. The lightning flash originated above the convective line and extended horizontally into the stratiform region. The coordinates of the plots are: a) height (km) versus time (sec), b) height (km) versus line normal distance (km), c) normalized VHF source frequency as a function of height, d) line parallel distance (km) versus line normal distance (km), and e) line parallel distance (km) versus height (km).

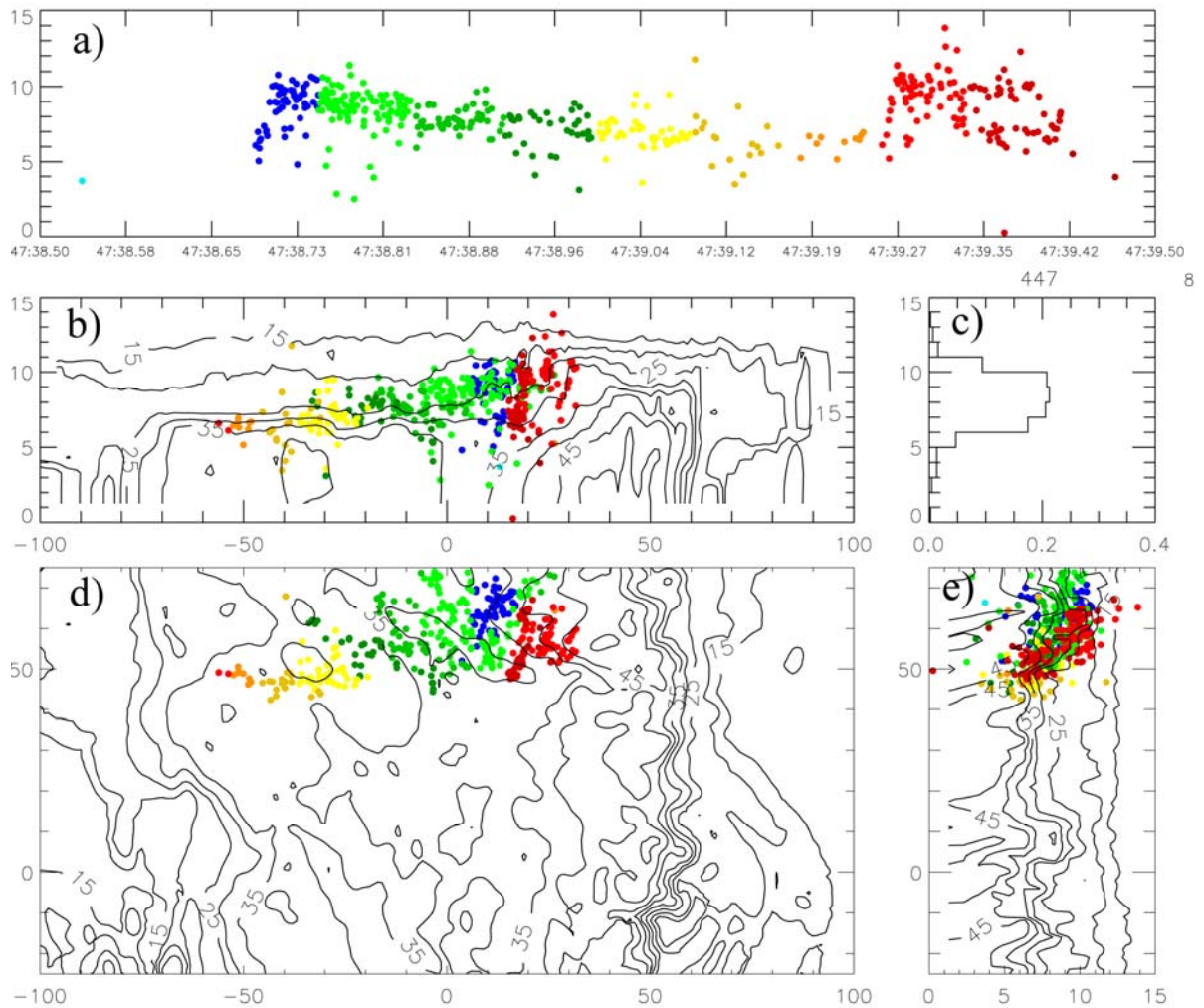


FIG. 3.10: Same as Fig. 3.9 except for a representative flash that originated in the convective region and propagated rearward and downward through the stratiform region. The flash occurred at 23:47 UTC.

into the stratiform region from areas outside the analysis domain. In taking into account all flashes that originate within the analysis domain, the percentage of flashes actually originating in the stratiform region varies depending on whether the time is before or after 23:15 UTC as the stratiform region begins to intensify. Before 23:15 UTC, an average of 10% of stratiform flashes originating in the analysis domain actually originated in the stratiform region. However, after 23:15 UTC, this percentage increased to over 50% (Fig. 3.12). The majority of stratiform flashes in the analysis domain originate in the stratiform region once the stratiform region becomes fully developed and the lightning pathway nears the melting level.

In order to investigate whether LDAR flash detection efficiency errors significantly impact the results during the analysis time period, the mean flash extent is measured for both convective and stratiform regions. The flash extent is measured as the maximum distance between any two VHF sources in one flash. As the system traverses the LDAR network, the flash extents for both convective and stratiform regions remain relatively steady near 60 km and 20 km, respectively (Fig. 3.13). If the LDAR flash detection efficiency decreased significantly with distance from the network center, then flashes would have been broken up into smaller, lesser extent flashes during earlier time periods. This would have caused the flash extent to slowly grow with time as the MCS approached the network center. The steady flash extent increases our confidence that flash detection efficiency did not adversely affect our results within the effective range of the network as defined by Ely et al. (2007).

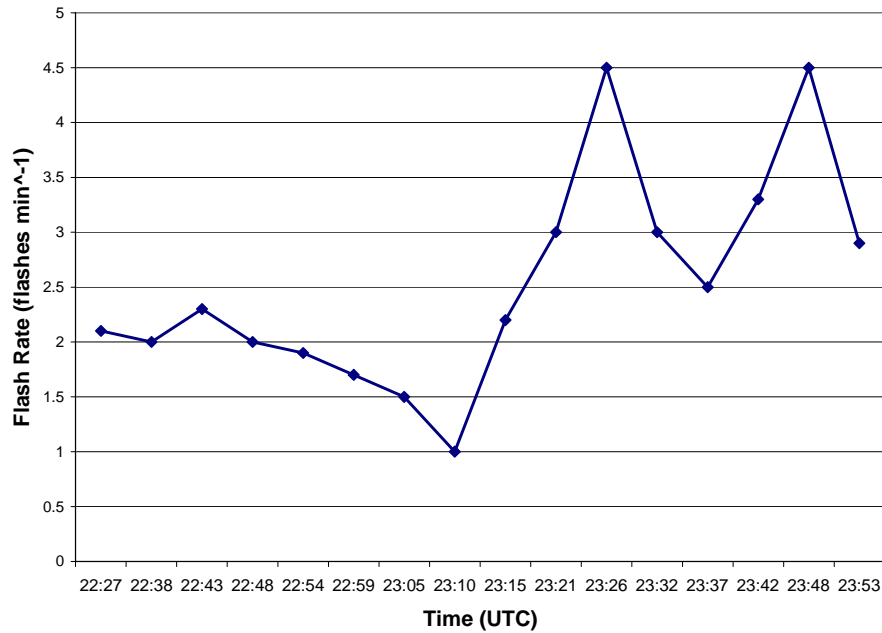


FIG. 3.11: Time series plot of the 31 October MCS stratiform flash rate during ten minute intervals centered on the radar volume scan times.

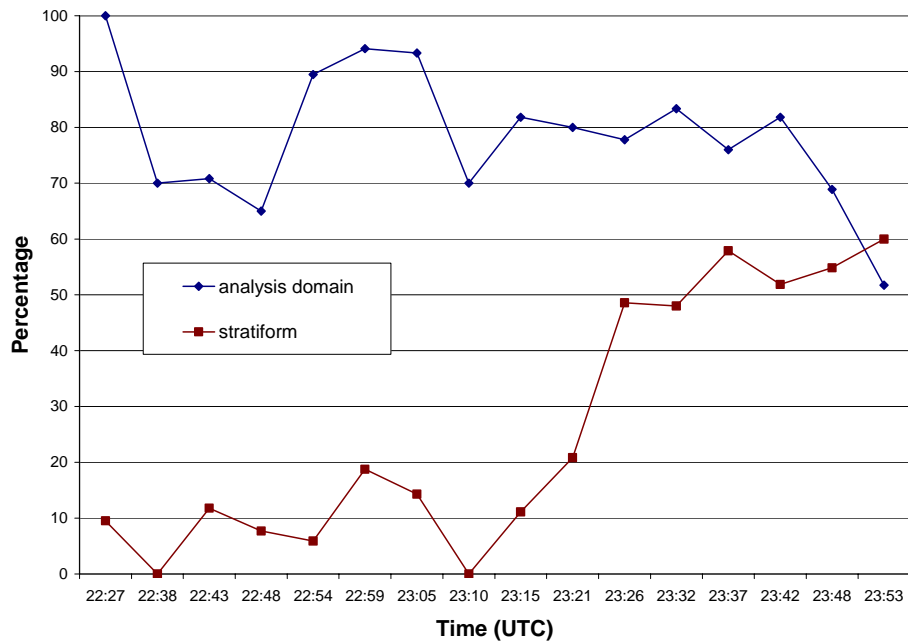


FIG. 3.12: Time series plot of the percentage of stratiform flashes originating in the 31 October MCS analysis domain (convective, transition, or stratiform regions). Also plotted is the percentage of these flashes that originate in the stratiform region.

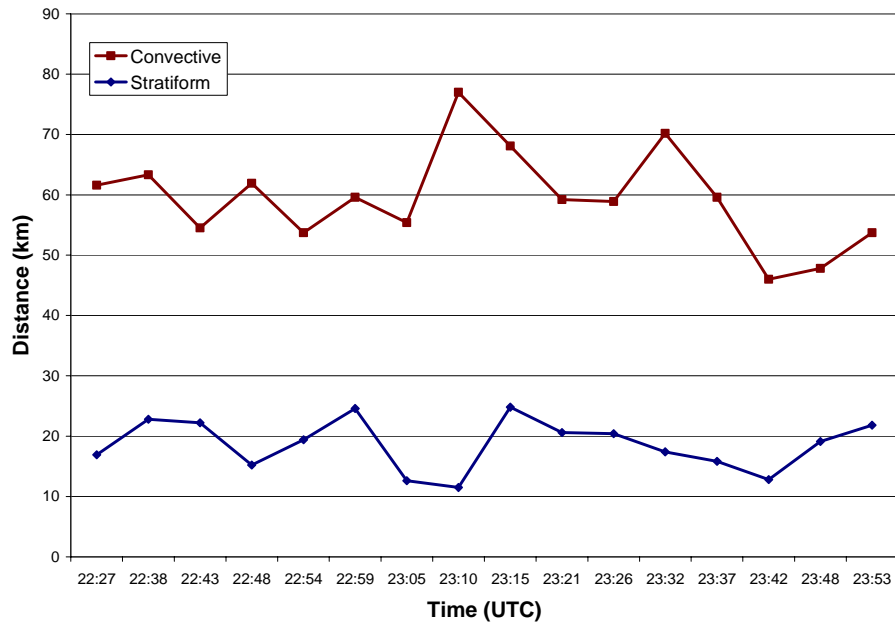


FIG. 3.13: Time series plot of the mean flash extent for stratiform flashes originating in both the 31 October MCS stratiform and convective regions.

The mean VHF source count is determined for flashes originating in the stratiform region and those that propagate into the stratiform region from the convective region. The mean VHF source count for flashes originating in the convective region and propagating into the stratiform region drops considerably from 800 to 400 VHF sources during the analysis time (Fig. 3.14). If this was a detection error, then the mean VHF source count should increase with time. The decrease in sources may be due to the weakening of the convective line and decreasing extent of charge layers. Although the flash extent remained fairly constant throughout the time period (Fig. 3.13), the flashes during later times may have been less branched and extensive in the convective region due to decreasing charge layers as the line weakens. The stratiform mean VHF source

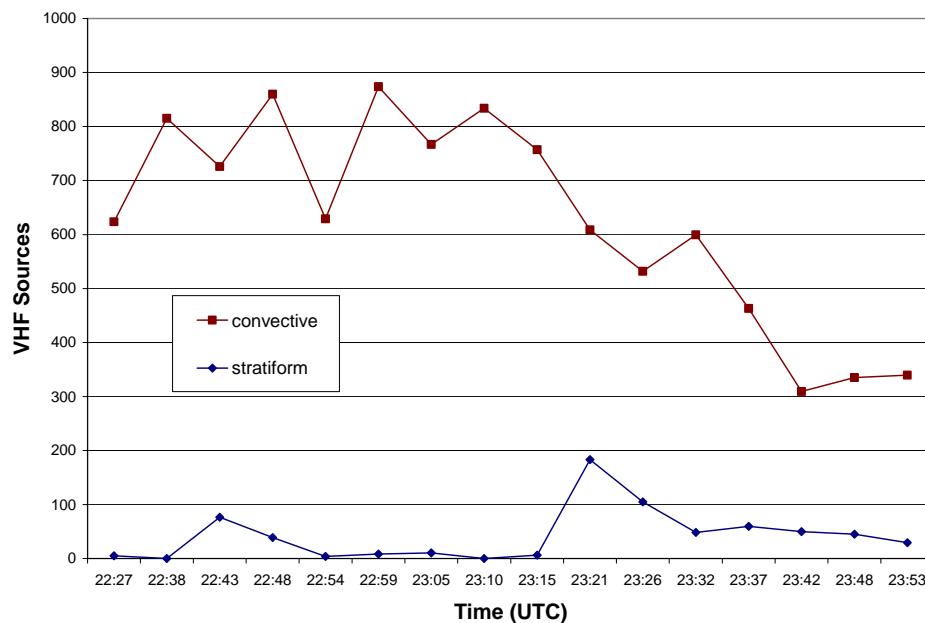


FIG. 3.14: Time series plot of the mean number of VHF sources that compose stratiform flashes originating in both the 31 October MCS stratiform and convective regions.

count shows a slight increase with time. This increase, however, could be associated with developing extensive charge layers in the stratiform region with time.

The mean heights of stratiform flashes differ depending on which region (convective or stratiform) the flashes originated in. Flashes originating in the convective region and propagating into the stratiform region tend to have higher mean heights compared to their counterparts in the stratiform region (Fig. 3.15). The mean height of convective flashes that propagate into the stratiform region lowers steadily with time from 9 km to 7.5 km. The lowering of the mean height is consistent with the slanting lightning pathway as well as the weakening of the convective line and lowering echo heights throughout the MCS (Figs. 3.5, 3.7). The mean heights of flashes originating in the stratiform region show a more complex trend with the mean decreasing in height

from 9 km to 5 km before 23:15 UTC and from 8 km to 6 km after 23:15 UTC (Fig 3.15). There is also a complex difference between the mean flash height of flashes originating in the stratiform region and the median initiation height of these flashes. During early times (before 23:15 UTC), the median initiation height is generally above the mean flash height, while later times (after 23:15 UTC) the median initiation height is below the mean flash height (Fig. 3.15). The relatively few flashes originating in the stratiform region during early analysis times could contribute to the noisier mean flash and origination height patterns. The overall lowering of flash heights as MCSs mature was also found by Lyons et al. (2003) in their study of two MCSs.

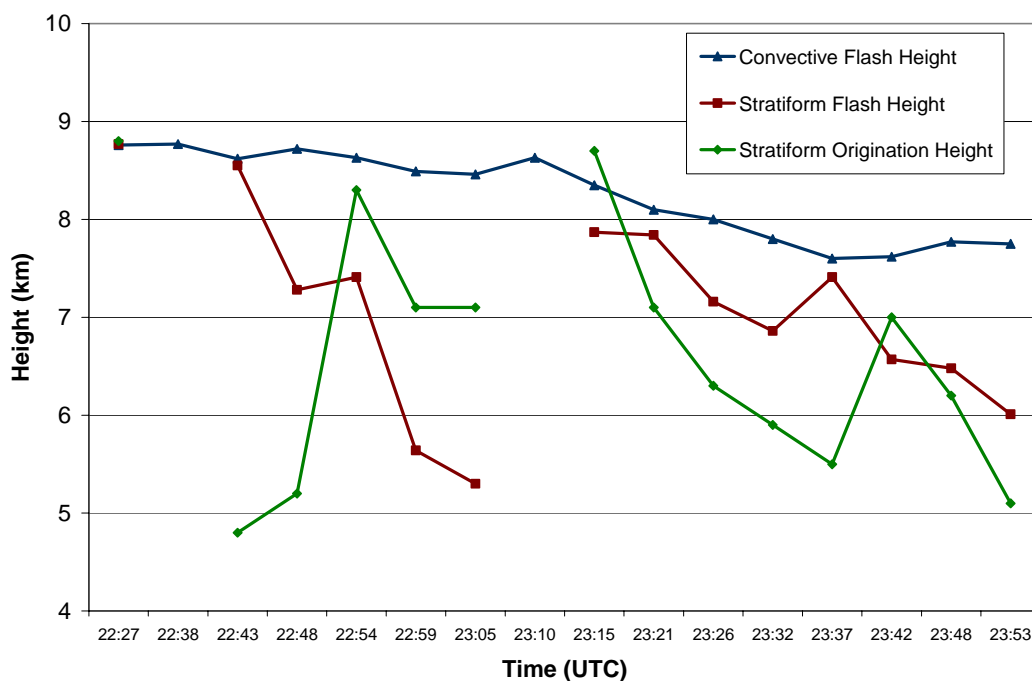


FIG. 3.15: Time series plot of the mean flash heights of stratiform flashes originating in both the 31 October MCS stratiform and convective regions. Also plotted is the mean height of the initiation of flashes originating in the stratiform region. Data gaps occur when no flashes originated in the stratiform region.

3.1.2.2 NLDN

NLDN data is used to document important trends in CG flashes during the evolution of the MCS. The IC:CG ratio for the stratiform region remains fairly constant (~ 4) throughout the time period (Fig. 3.16). However, the total flash rate in the stratiform region shows a general increasing trend with time; which along with a steady IC:CG ratio, indicates increasing CG rates with time as well. CG flash rates are found to increase from 0.1 - 0.6 CG flashes min^{-1} before 23:15 UTC to 0.6 - 1 flashes min^{-1} after 23:15 UTC (Fig. 3.17). The percent of positive CGs in the stratiform region fluctuates between around 25 – 50%, with higher percentages concentrated near the end of the analysis period. The increase in the NLDN flash rate in the stratiform region (Fig. 3.17) supports the similar increase found in the LDAR indicated flash rate (Fig. 3.11) during the same time period. While the CG flash rate in the stratiform region increased with time, the opposite was found in the convective region. The number of CGs found in the convective region reaches a high of 15.1 flashes min^{-1} at 22:54 UTC, then falls dramatically to 3.6 flashes min^{-1} at the end of the analysis time period (Fig. 3.18). The percent of positive CGs is in a range from 2 - 10 % throughout the time period, significantly lower than the percentages found in the stratiform region.

Mean peak currents of positive and negative CG flashes are also different between stratiform and convective regions. Positive CGs in the stratiform region deposit larger peak currents than their counterparts in the convective region (Fig. 3.19). The stratiform peak positive currents also show an increasing trend as the stratiform region

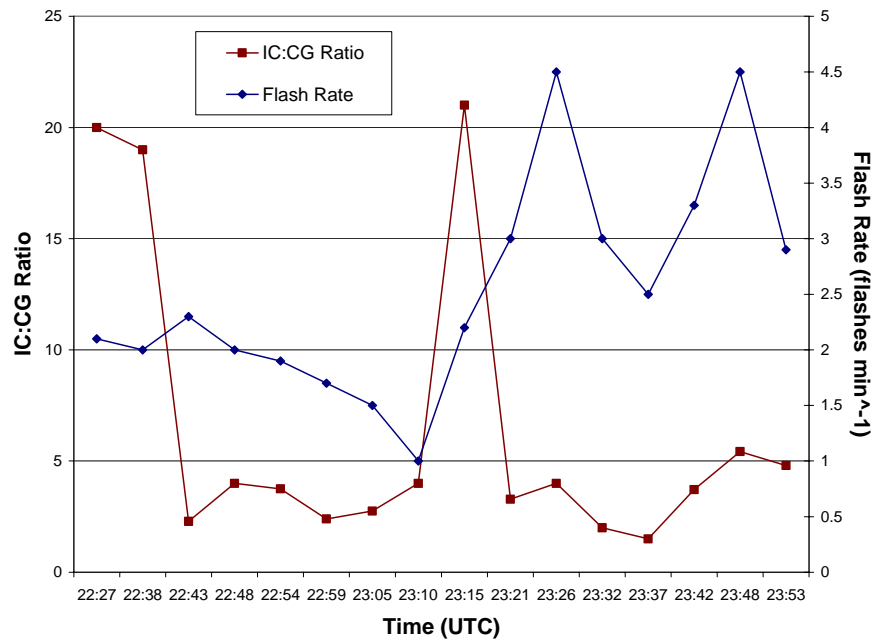


FIG. 3.16: Time series plot of the flash rate and the IC:CG ratio in the 31 October MCS over a ten minute time span centered on the radar volume scan time.

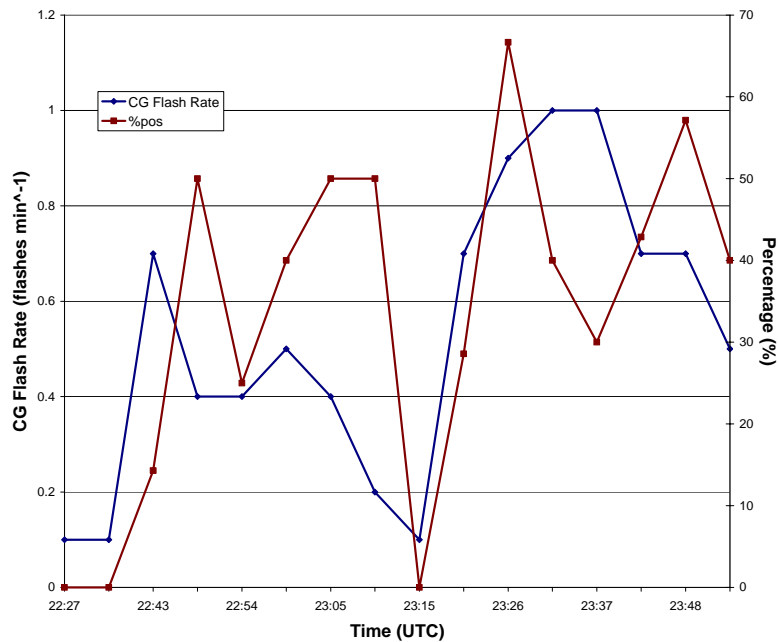


FIG. 3.17: Time series plot of the CG flash rate and the percent of positive CGs occurring over a ten minute time period in the 31 October MCS stratiform region.

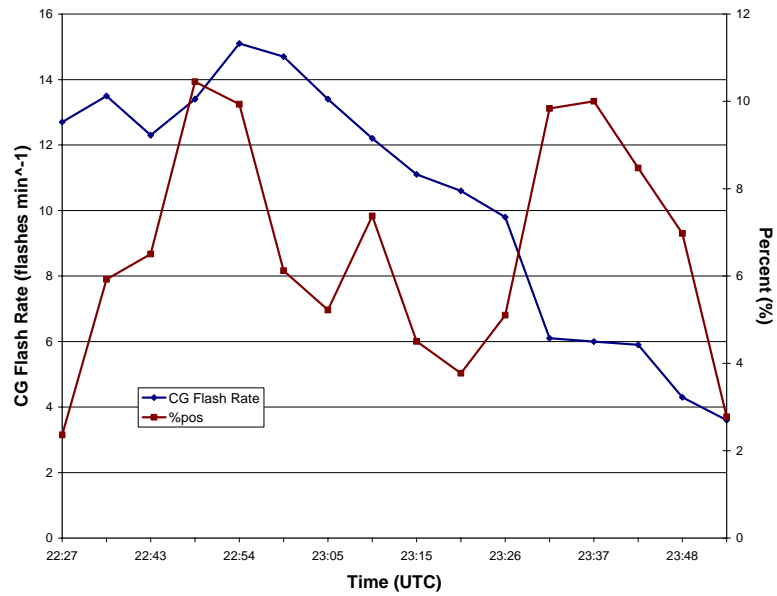


FIG. 3.18: Same as Fig. 3.17 except for in the 31 October MCS convective region.

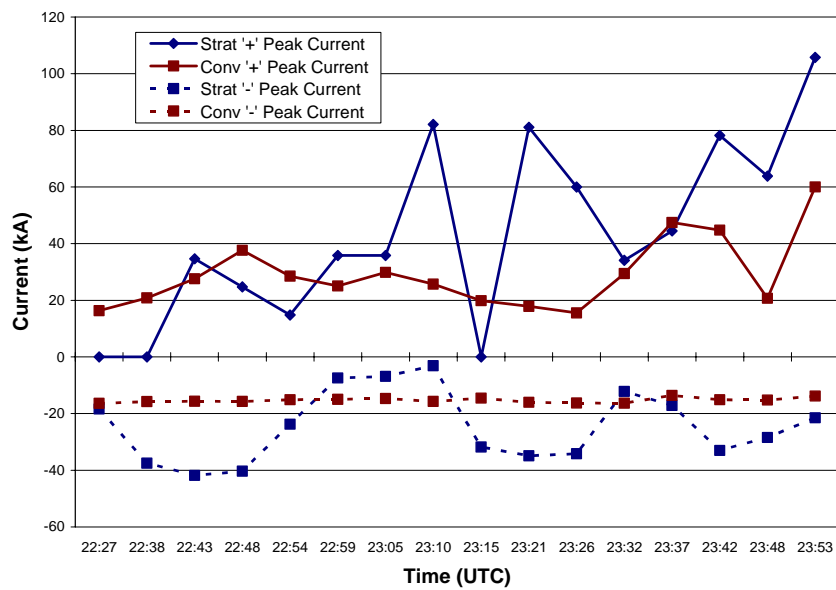


FIG. 3.19: Time series plot of the 31 October MCS stratiform and convective CG peak currents.

intensifies. The stratiform mean peak negative currents are much more variable (-2 to -40 kA) than the negative peak currents in the convective region (~ -15 kA).

Over the analysis time period, 18 separate stratiform region flashes are associated with CGs that contained a positive return stroke. Three parent stratiform flashes can not be uniquely defined due to the lack of LDAR detected VHF sources near (< 20 km and < 1 s) the ground strike point, or multiple flashes are near the ground strike location making the association between LDAR flash and NLDN ground stroke location ambiguous. The LDAR flash initiation points are then grouped into three categories based on location: (1) stratiform, if the location falls within the defined stratiform domain; (2) non-stratiform, if the location falls within the analysis domain, but outside the stratiform region; and (3) outside, if the flash origination falls outside the analysis domain. These groupings are then subdivided by when the flashes occur, either before or after 23:15 UTC. This time is used because it appeared as a midway point for stratiform development and the evolving lightning pathway. The mean, maximum, and minimum are then computed for the LDAR flash VHF source count, maximum LDAR flash extent, and NLDN return stroke current for the +CG flashes occurring in the stratiform and non-stratiform categories.

Stratiform region positive CG strokes, which occur throughout the analysis time period, are associated with 15 unique LDAR flashes. The number of flashes originating in the stratiform, non-stratiform, and outside regions, that contain a CG with at least one positive return stroke located in the stratiform region, are 6, 5, and 4 respectively. After further subdividing the groups based on occurrence before (after) 23:15 UTC, the

distributions are 0(6), 2(3), 0(4) in the stratiform, non-stratiform, and outside domains, respectively. These results, plus other positive CG flash statistics, which are taken from the NLDN and LDAR networks, are listed in Table 3.1. The mean LDAR flash extent and LDAR VHF source count of flashes from the non-stratiform region are larger than those from the stratiform region, which can be expected because of the distance the flashes need to propagate in order to tap into the charge in the stratiform region (20-40 km). However, flashes originating in the stratiform region generally propagate in the along line direction and are thus limited by the line-parallel size of the domain. Larger stratiform flash extents may be seen with a larger analysis domain in the line-parallel

Table 3.1: Summary of flash statistics for the 31 October MCS stratiform region positive CG flashes that originated in stratiform (top) and non-stratiform regions (bottom).

Stratiform			
		Count	
Total		6	
Before(after) 2315 UTC		0(6)	
	source count	extent (km)	current (kA)
mean	272	51	81
min	20	13	12
max	879	79	180
Non-stratiform			
		Count	
Total		5	
Before(after) 2315 UTC		2(3)	
	source count	extent (km)	current (kA)
mean	883	80	43
min	330	48	12
max	1986	104	82

direction. Interestingly, the mean NLDN positive peak current flashes originating in the non-stratiform region is less than the peak current from those originating in the stratiform region, despite the shorter flash extents of the stratiform originating flashes.

A five panel plot of lightning VHF sources and corresponding maximum reflectivity for an example stratiform flash originating in the convective and stratiform regions are shown in Fig. 3.20 and Fig. 3.21, respectively. The flash originating in the convective region occurred at 23:02 UTC. In the line normal distance versus height panel (Fig. 3.20b), it shows similar features of the composite lightning pathway representative of that time (Fig. 3.8b). The flash begins at the top rear of the convective region and propagates 70 km horizontally rearward through the transition and stratiform regions. The flash slants slightly in the line normal direction before leveling off near 8 - 10 km in the stratiform region, above other flashes seen during later times. This flash

could indicate the transition of the lightning pathway from extending horizontally rearward from the top of the convective line to slanting rearward and downward into the stratiform region. The flash exhibits a somewhat of a bi-level structure with the majority of its VHF sources occurring between 8 – 10 km and another grouping of sources near the 5 km level. The horizontal layers are more ambiguous in the line parallel distance vs. height plot (Fig. 3.20e). The horizontal extent and number of VHF sources of this flash is the max of all flashes originating in the non-stratiform region at 103.56 km and 1986 respectively (Table 3.1). However, the peak positive current deposited on the earth by the flash is just above the mean of non-stratiform flashes (Table 3.1). The flash that originates in the stratiform region at 23:42 UTC initiates near the edge of the analysis domain and propagates 80 km in the line parallel direction (Fig. 3.21). The majority of the sources of this flash occur between the heights of 6 km and 7 km. This flash has an extent of 119.86 km which is the maximum extent seen by flashes originating in the stratiform region and has 504 sources, which is above average of flashes originating in the stratiform region (Table 1).

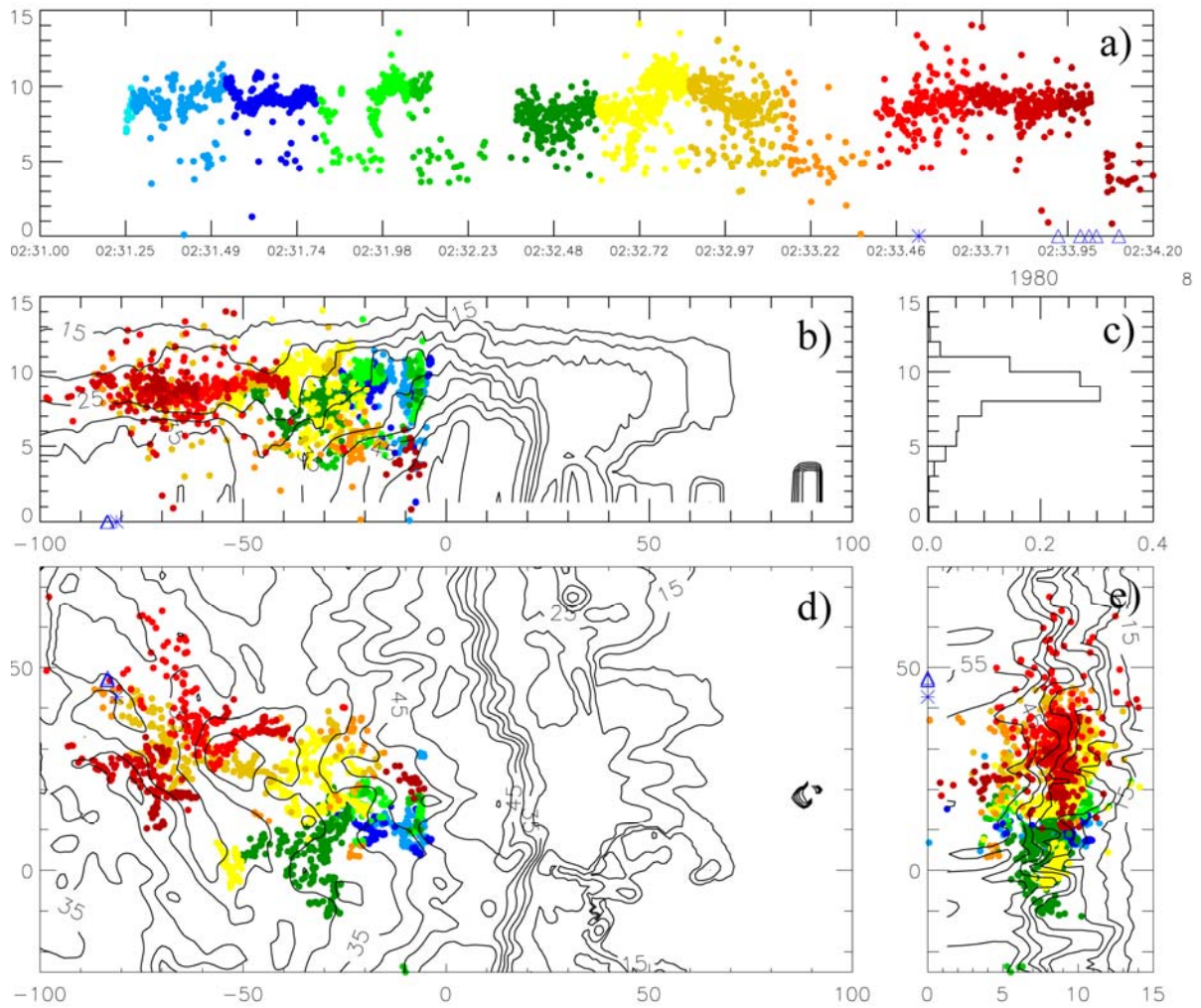


FIG. 3.20: Same as Fig. 3.9 except with a +CG flash originating from the convective line at 23:02 UTC. Triangles (Δ) indicate a negative CG stroke while asterisks (*) indicate positive CG strokes.

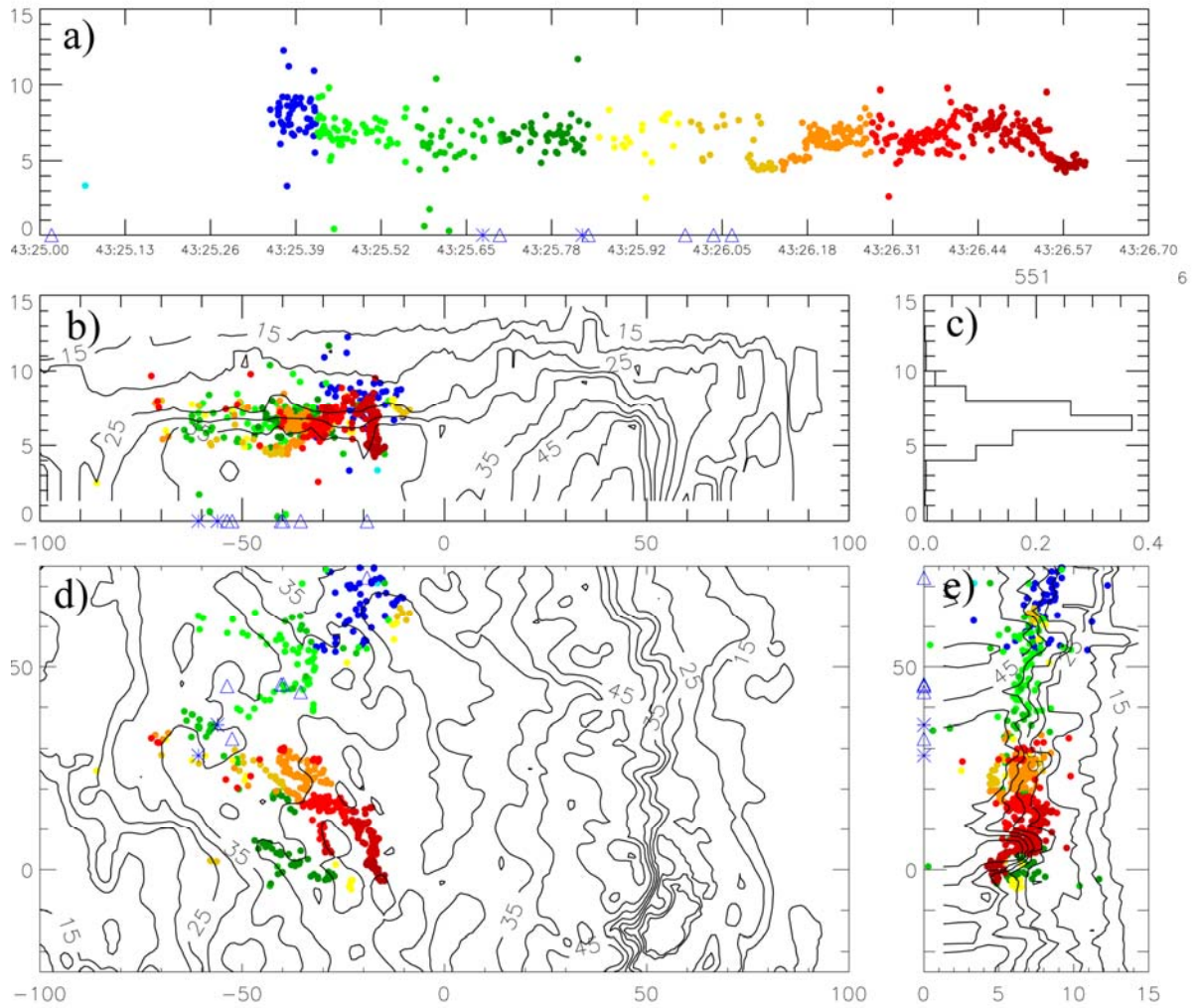


FIG. 3.21: Same as Fig. 3.9 except with a + CG flash originating in the stratiform region at 23:42 UTC. Triangles (Δ) indicate a negative CG stroke while asterisks (*) indicate positive CG strokes.

3.2 2006 April 21 LLTS MCS

On 2006 April 21, another symmetric LLTS MCS traversed within range of Houston's WSR-88D (KHGX) and Texas A&M's LDAR network. The MCS formed in central Texas and propagated east toward and into the Gulf of Mexico (Fig. 3.22). As the MCS traversed the LDAR network, it too underwent significant evolution in both the convective and stratiform regions. The evolution of the partitioned stratiform and convective regions will be analyzed by using total lightning and radar characteristics during a time span of two and a half hours from 10:40 UTC to 13:01 UTC.

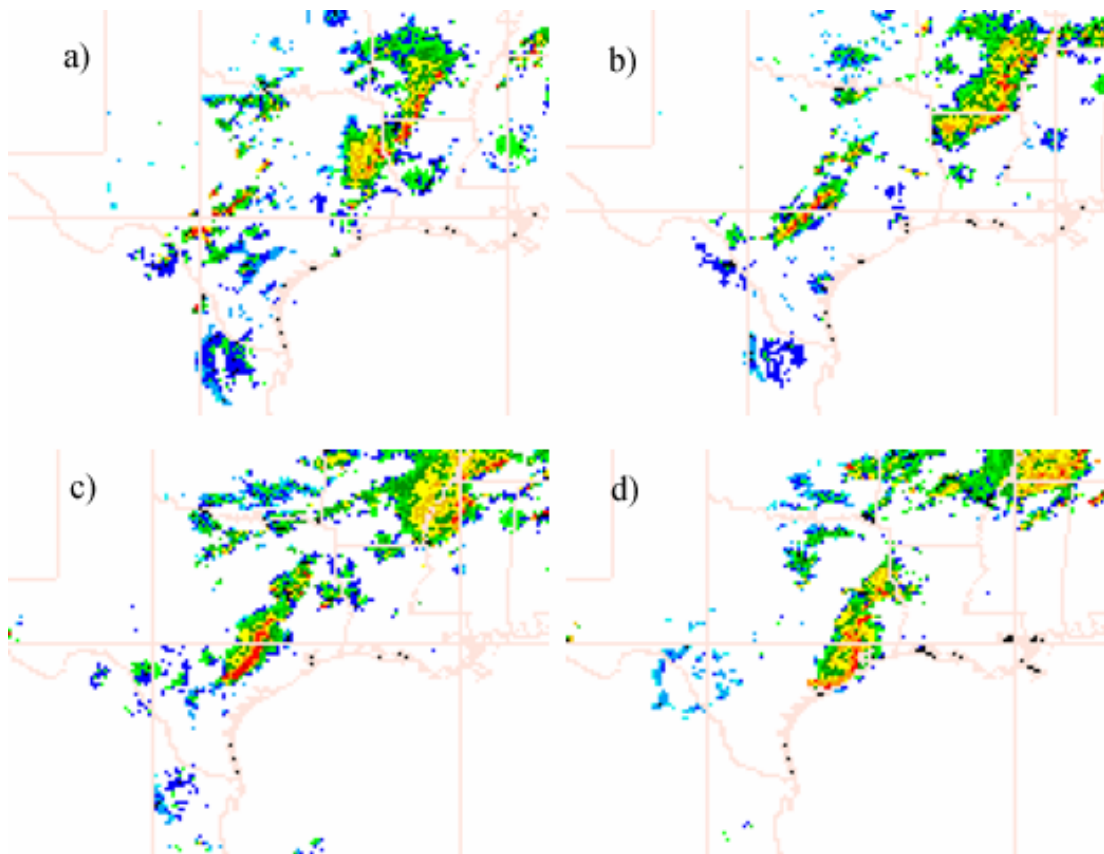


FIG. 3.22: NEXRAD reflectivity images of the 21 April MCS at a) 06:00 UTC, b) 08:00 UTC, c) 10:00 UTC, and d) 12:00 UTC.

3.2.1 Radar Reflectivity

Radar reflectivity analysis is used to investigate the evolution of the intensity and structure of the MCS. The following analyses are performed on the partitioned stratiform and convective regions as seen in Fig. 3.23. Once again, a combination of CFADs and time series of reflectivity and rain rates are used to provide a summary of the MCS evolution. Two CFADs, along with mean profiles, for both the stratiform (Fig. 3.24a) and convective regions (Fig. 3.24b), are produced to compare against the corresponding LDAR VHF lightning source density displays at critical times in the evolution of the stratiform region lightning structure. The times shown for both regions are 11:09 UTC and 12:41 UTC, near the beginning and end of the analysis time period.

According to Fig. 3.24a, as the stratiform region evolves from 1109 UTC to 1241 UTC, there is an increase in frequency of high reflectivity values (> 45 dBZ) at low-to-mid levels (< 6 km) as the upper limit of the 1% (0.1%) contour changes from 44 (45) dBZ to 49 (53) dBZ. This increase can be associated with the development and growth of the radar bright band, which occurs due to ice crystals growing by deposition and aggregation before melting near the 0°C level (Houze et al. 1989). Also, at higher heights, reflectivities decrease from 1109 UTC to 1241 UTC. Mean reflectivities drop 10 dB from 15 dBZ to 5 dBZ at a height of 13 km, which could be indicative of particles slowly falling in the stratiform region. Once again, it is noted that the percentage of available data points from the maximum number of points decreases with height to below 20% above 14 km and therefore may not be representative of storm structure.

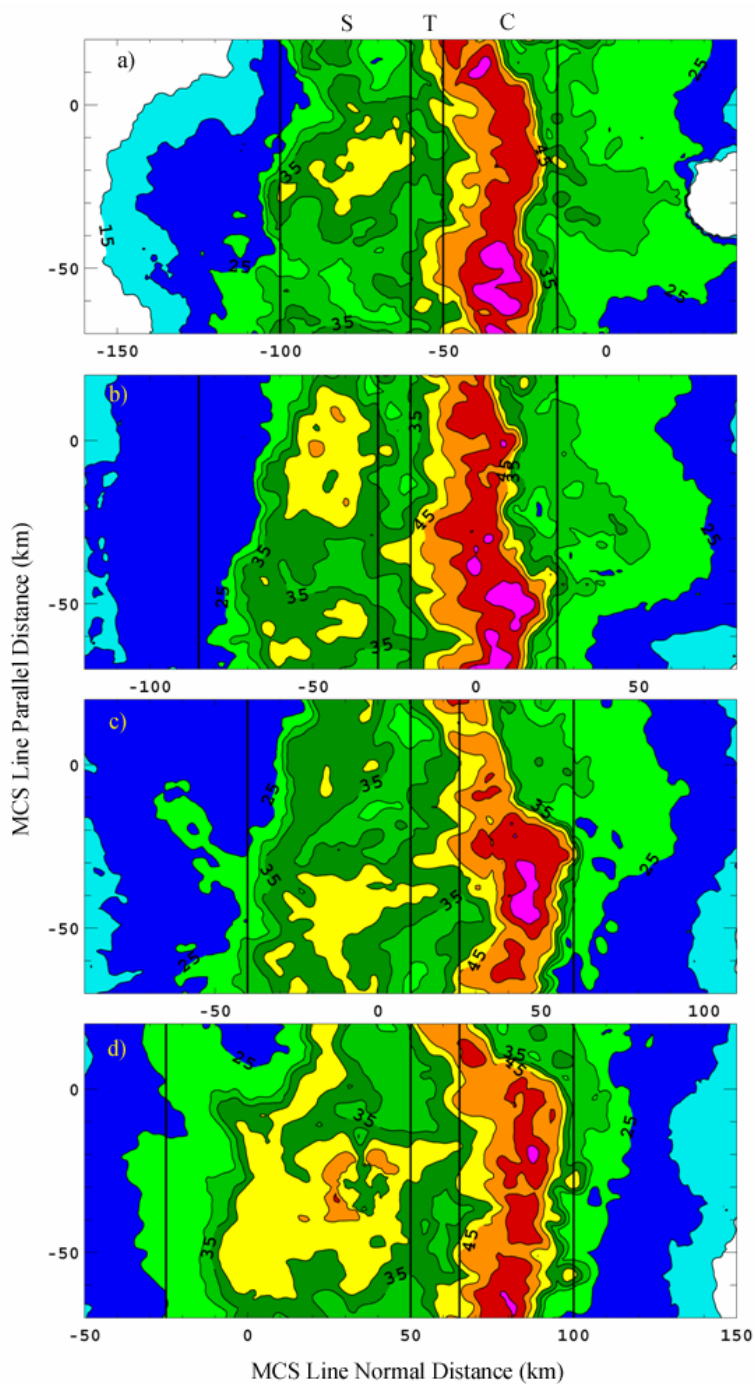


FIG. 3.23: Composite reflectivity images for four different times during the lifetime of the 21 April MCS. The times shown are: a) 11:09 UTC, b) 11:34 UTC, c) 12 UTC, and d) 23:32 UTC. Reflectivity is contoured every five dBZ with every other contour labelled (25 dBZ, 35 dBZ, 45 dBZ, 55 dBZ). Warmer colors indicate higher reflectivity values. Vertical solid lines indicate portions of the stratiform (S), transition (T), and convective (C) regions.

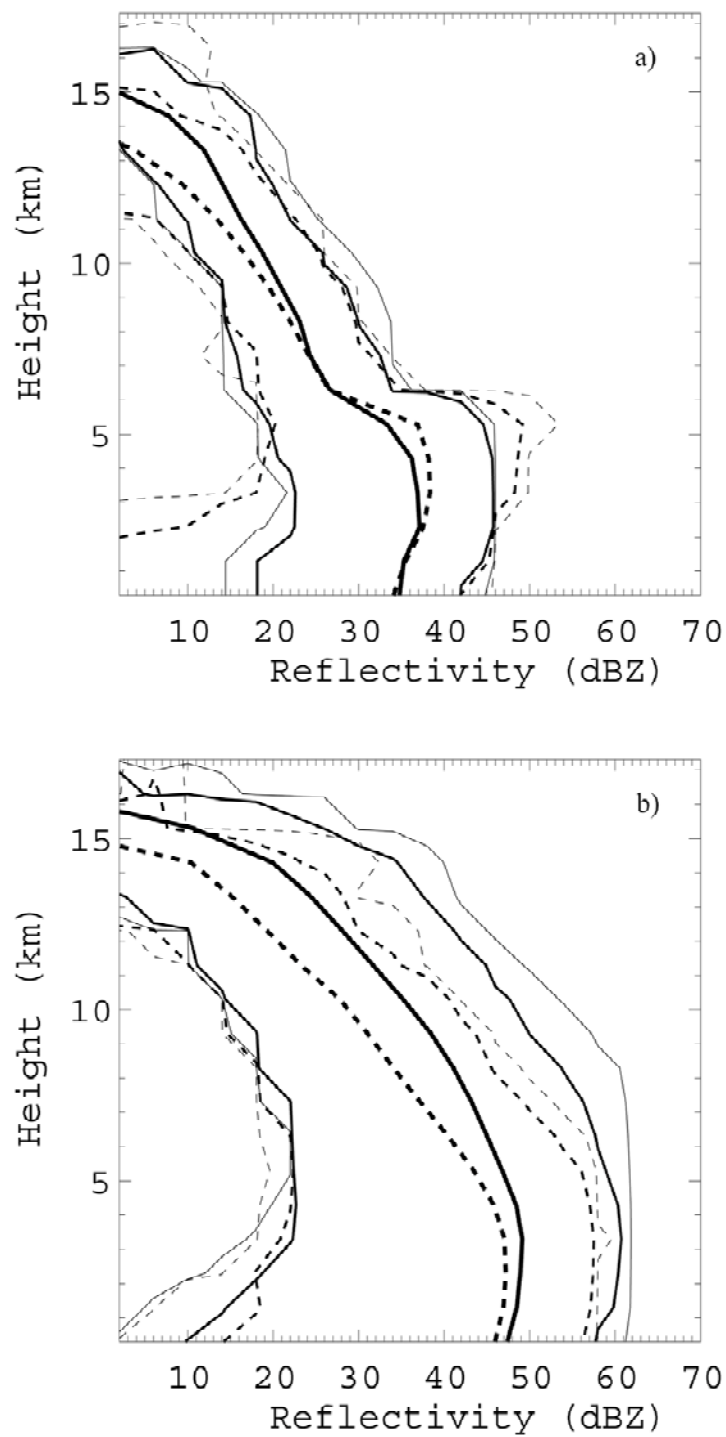


FIG. 3.24: Contoured frequency by altitude diagrams (CFADs) and mean profiles of radar reflectivity for the 21 April MCS a) stratiform and b) convective regions for 11:09 UTC (solid) and 12:41 UTC (dashed). The bin size was set to 4 dBZ and the displayed contours are 0.1% data $\text{dBZ}^{-1} \text{km}^{-1}$ (gray), 1% data $\text{dBZ}^{-1} \text{km}^{-1}$ (black), and the mean dBZ (bold).

On the other hand, the convective CFADs (Fig. 3.21b) show a weakening trend as reflectivity values generally decrease throughout all heights. The largest decrease occurs between the heights of 8 km and 11 km where the 0.1% contour decreases by an average of 10 dB. In lower levels, high reflectivity values (> 60 dBZ) are shown at early times while they are completely absent at later times.

In addition to the CFADs, time series of mean reflectivities at all heights are shown for the stratiform (Fig. 3.25a) and convective (Fig. 3.25b) regions. The stratiform region's greatest change throughout the time period occurs at low-to-mid levels. At heights near 4 and 5 km, reflectivity values are below 35 dBZ during early times. However, as time progresses, higher reflectivities (>35 dBZ) are seen at these heights (Fig. 3.25a). Also, reflectivities over 38 dBZ emerge at low heights (2-4 km) at later times. Higher reflectivities seen at low-to-mid levels in the stratiform region during later time periods are indicative of particle deposition, aggregation, and melting as they fall through the melting level. At higher levels (> 12 km) reflectivities fall significantly on the order of 5 dB in time (Fig. 3.25a). The mean reflectivity at 12 km is close to 15 dBZ near the beginning of the time period and falls to below 10 dBZ at the end of the analysis period. This could be the result of a combination of the convective line weakening and ejecting small ice particles at lower heights and also the particles falling from higher to lower heights in the stratiform region as time passes. During two time periods, near 11:29 UTC and 12:17 UTC, reflectivity pulses at all heights.

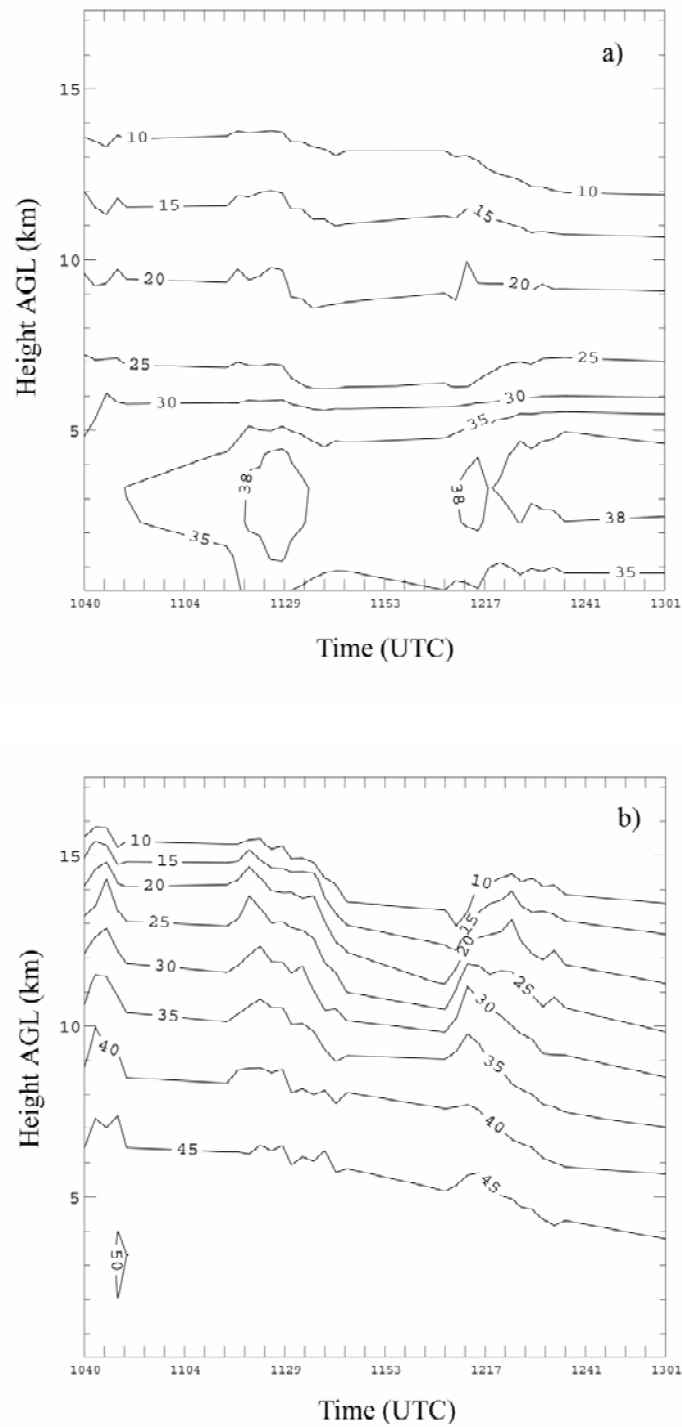


FIG. 3.25: Time series of mean reflectivities at all elevations for the 21 April MCS a) stratiform and b) convective regions. Mean reflectivity is contoured every 5dBZ from 10 dBZ to 55 dBZ.

The convective region, on the other hand, shows decreasing mean reflectivities throughout all heights. Higher mean reflectivities (> 45 dBZ) are more predominant at lower levels, with some mean values of 50 dBZ seen during early times (Fig. 3.25b). At heights of 5 km and above, mean reflectivities drop considerably. The mean reflectivity at 6 km starts above 45 dBZ and then begins to decrease down to below 40 dBZ by the end of the analysis time period. At 10 km, the mean reflectivity begins near 40 dBZ and continues to decrease significantly to below 25 dBZ. The decrease in reflectivity at mid-to-upper levels is a sign of the convective region weakening. As time passes, the weakening updraft is likely only able to support smaller particles. However, similar to the stratiform region, the reflectivity pulses at all height levels near 11:29 UTC and 12:17 UTC (Fig. 3.25b). These results, from both the stratiform and convective region, are very similar to the CFAD results for each region in showing a strengthening stratiform region and a weakening convective region.

A time series plot of stratiform and convective mean reflectivity and area at a height of 4.3 km is provided as additional support to the CFADs and the mean reflectivities at all heights (Fig. 3.26). This height was chosen because of its proximity to the melting level during the time of the MCS. Notice that the area of the stratiform region quadruples from 1030 UTC to 1236 UTC from less than 2,000 km² to over 8,000 km². With this increase in area, the mean stratiform reflectivity value significantly increases from around 32 dBZ to 38 dBZ. Similar to the CFADS, this time series plot shows a strengthening of the stratiform reflectivity. On the other hand, the convective area does not change nearly as dramatically (steady near 4,000 km²); however, the mean

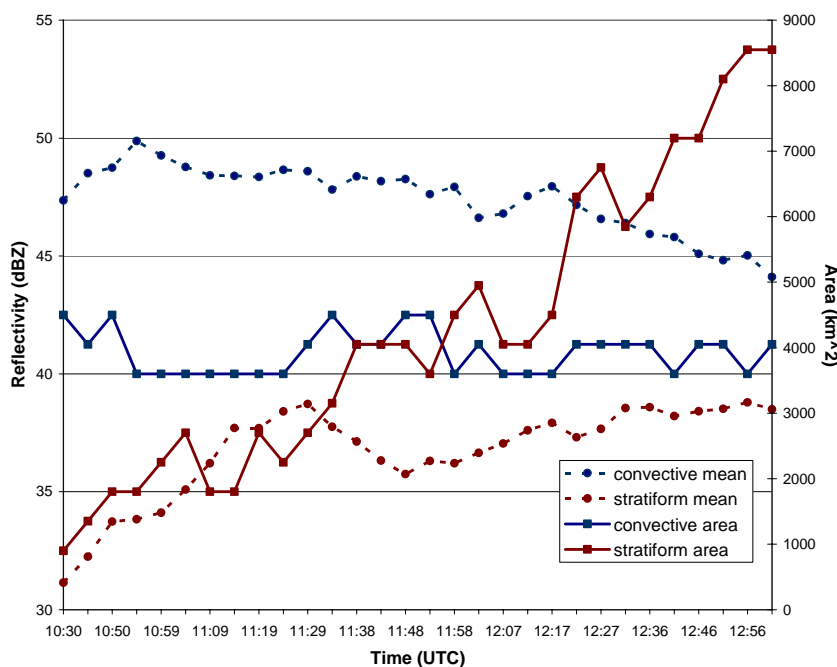


FIG. 3.26: Time series plot of the mean stratiform and convective reflectivities of the 21 April MCS at a height of 4.3 km. Also plotted are the areas of the mean stratiform and convective regions.

convective reflectivity values significantly decrease from near 50 dBZ to 44 dBZ. This, along with the convective CFAD and mean reflectivity plots (Figs. 3.24b & 3.25b), shows the convective region slowly weakening throughout the MCS lifetime during the analysis time period.

The rainfall amount is calculated by determining the mass of rain that fell during each radar volume scan time for both stratiform and convective regions and is also used as a final justification for the strengthening of the stratiform region and weakening of the convective region (Fig. 3.27). The rainfall totals in the stratiform region increase from close to 1×10^5 kg to 3×10^6 kg under the analysis area. Rainfall below the convective region decreases by one half from 2×10^7 kg to 1×10^7 kg. Total rainfall supports the

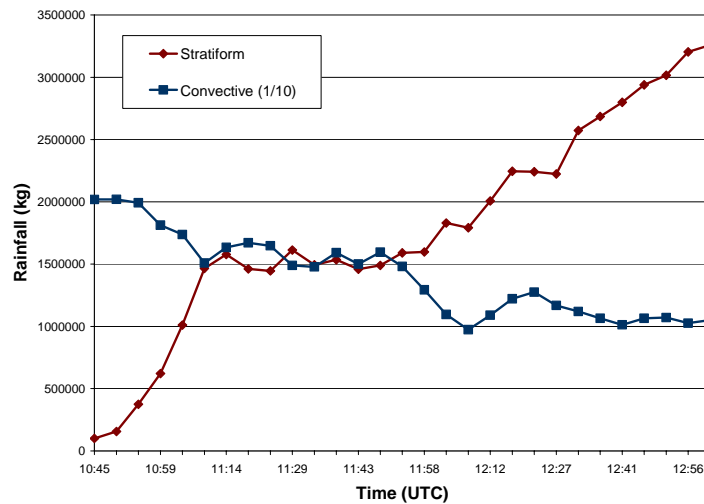


FIG. 3.27: Time series plot of the radar derived rain mass that fell under the 21 April MCS convective and stratiform regions during the time span of each volume scan.

previous analyses with the stratiform region intensifying and the convective region becoming less intense with time.

3.2.2 Total Lightning

Along with radar reflectivity, the total lightning structure evolved as the MCS traversed Houston within the effective range of the LDAR network. The following two sections give insight into the evolving structure of the 21 April MCS based on LDAR and NLDN data.

3.2.2.1 Lightning Detection and Ranging (LDAR)

Ten minute LDAR source density plots are overlaid on composite contoured reflectivity for several times: 1109 UTC, 1138 UTC, 1207 UTC, and 1241 UTC. At earlier times (1109 UTC, 1138 UTC), the lightning pathway extends horizontally rearward by 40 - 50 km from the top of the convection into the stratiform region at a

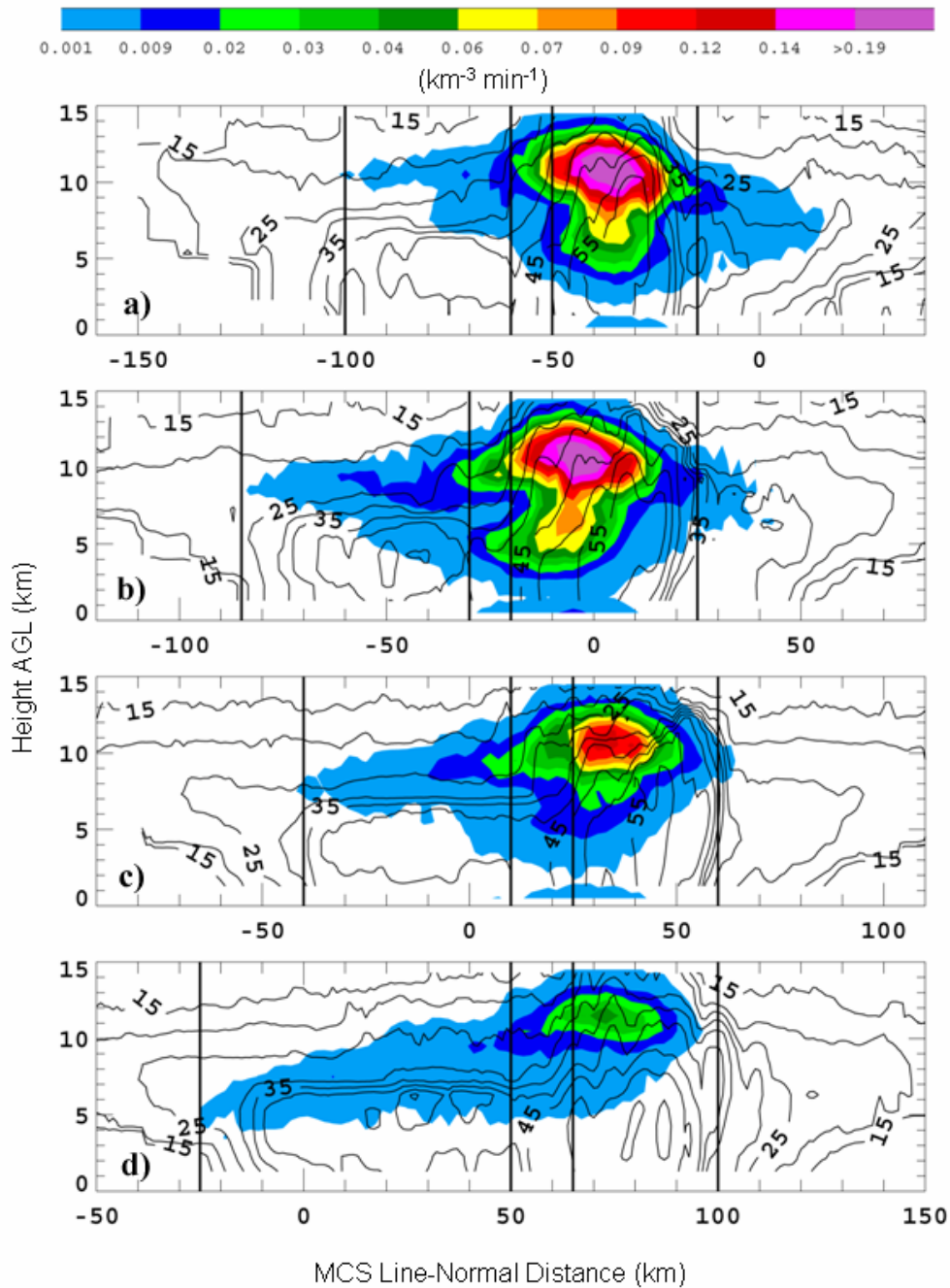


FIG. 3.28: VHF source density (color filled) and composite radar reflectivity (contoured) line normal vs. vertical cross-section plots for 4 different times during the evolution of the 21 April MCS. The times shown are: a) 11:09 UTC, b) 11:38 UTC, c) 12:07 UTC, and d) 12:41 UTC. Solid vertical lines indicate the applied partitioning method between the convective and stratiform regions. VHF source densities were taken over a 10 minute interval centered on the radar volume start time indicated. Resolution in the vertical (horizontal) is 1 km (2 km).

steady altitude between 10 km and 12 km (Fig. 3.28ab). As the MCS matures, the lightning pathway evolves such that it slants downward by 6 km and rearward by 40 km from the top of the convection at 12 km altitude through the transition zone toward the radar bright band in the stratiform region. Once over the stratiform bright band, the lightning levels off and extends 40-50 km horizontally back into the stratiform region at a height between about 5 and 7 km (1207 UTC, 1241 UTC) (Fig. 3.28cd). The descent of the pathway levels off just above the melting level and the radar bright band. Also, note during these time steps the increasing area of the 40 dBZ and 45 dBZ contours in the stratiform region (Fig. 3.28a-d). This increase in area may also be seen in Fig. 3.21a-d. As the stratiform area increases and reflectivities become more intense, the lightning pathway takes on a more slanted course (Fig. 3.28). Because of the short time scale (10 min), the path of individual flashes can be assumed.

Two representative flashes of the horizontal and slanting lightning pathways that originate in the convective region and propagate into the stratiform region occurred at 11:09 UTC (Fig. 3.29) and 12:43 UTC (Fig. 3.30). The flash that occurred at 11:09 UTC originated in the convective region and propagated horizontally rearward into the stratiform region. The majority of sources slants slightly in the line normal domain, but are concentrated at a height of 9 – 13 km as the flash extends into the stratiform region (Fig. 3.29). The flash that occurred at 12:43 UTC extends 110 km rearward and 6 km downward from a height of 10 – 12 km at the top of the convective line through the transition zone and stratiform region to a height of 4 – 6 km (Fig. 3.30). This flash represents the lightning pathway for the time period near 12:41 UTC (Fig. 3.28d).

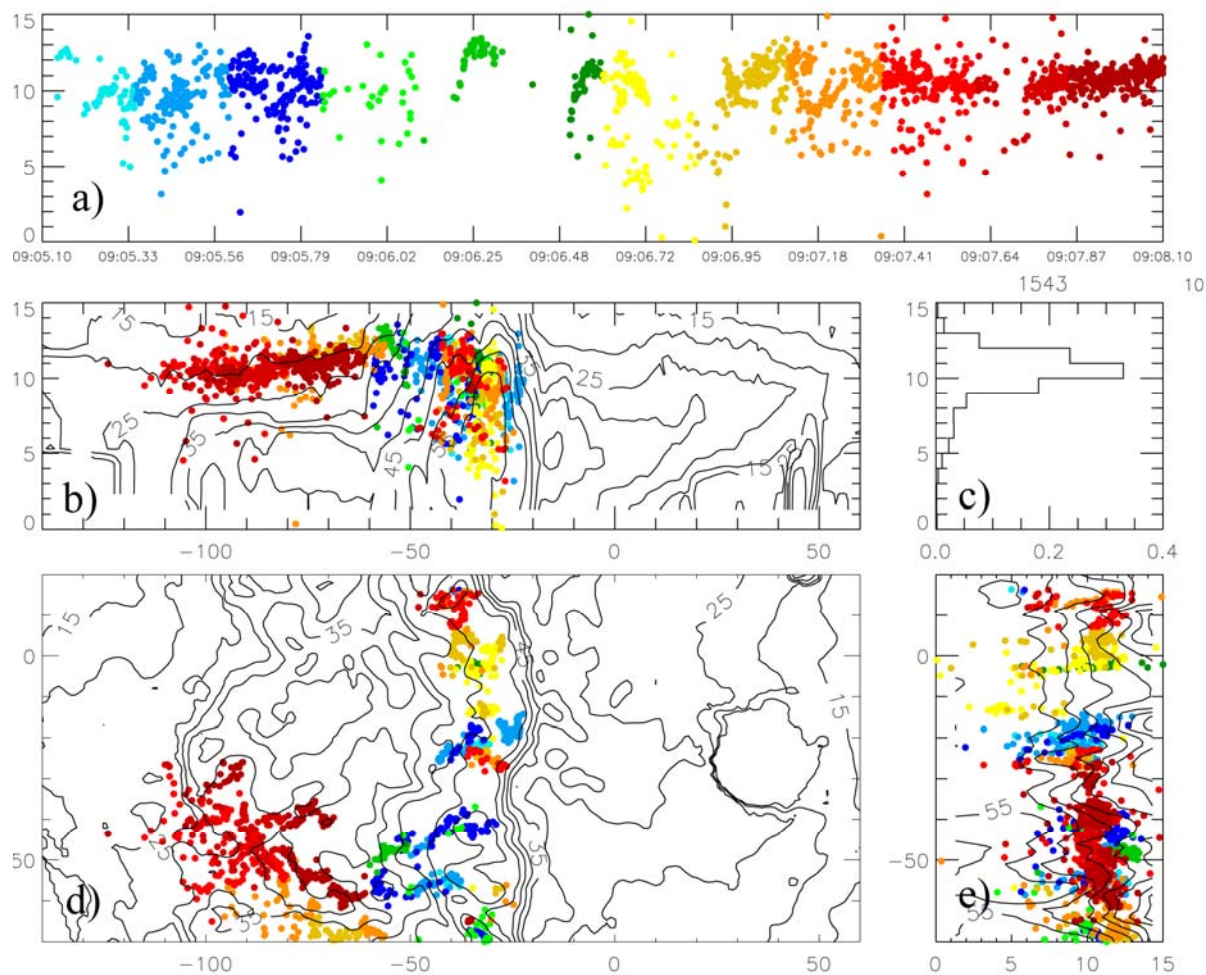


FIG. 3.29: Plot of VHF lightning sources (color coded with respect to time) and composite reflectivity associated with a representative flash that occurred on 21 April at 11:09 UTC. The lightning flash originated above the convective line and extended horizontally into the stratiform region. The coordinates of the plots are: a) height (km) versus time (sec), b) height (km) versus line normal distance (km), c) normalized VHF source frequency as a function of height, d) line parallel distance (km) versus line normal distance (km), and e) line parallel distance (km) versus height (km).

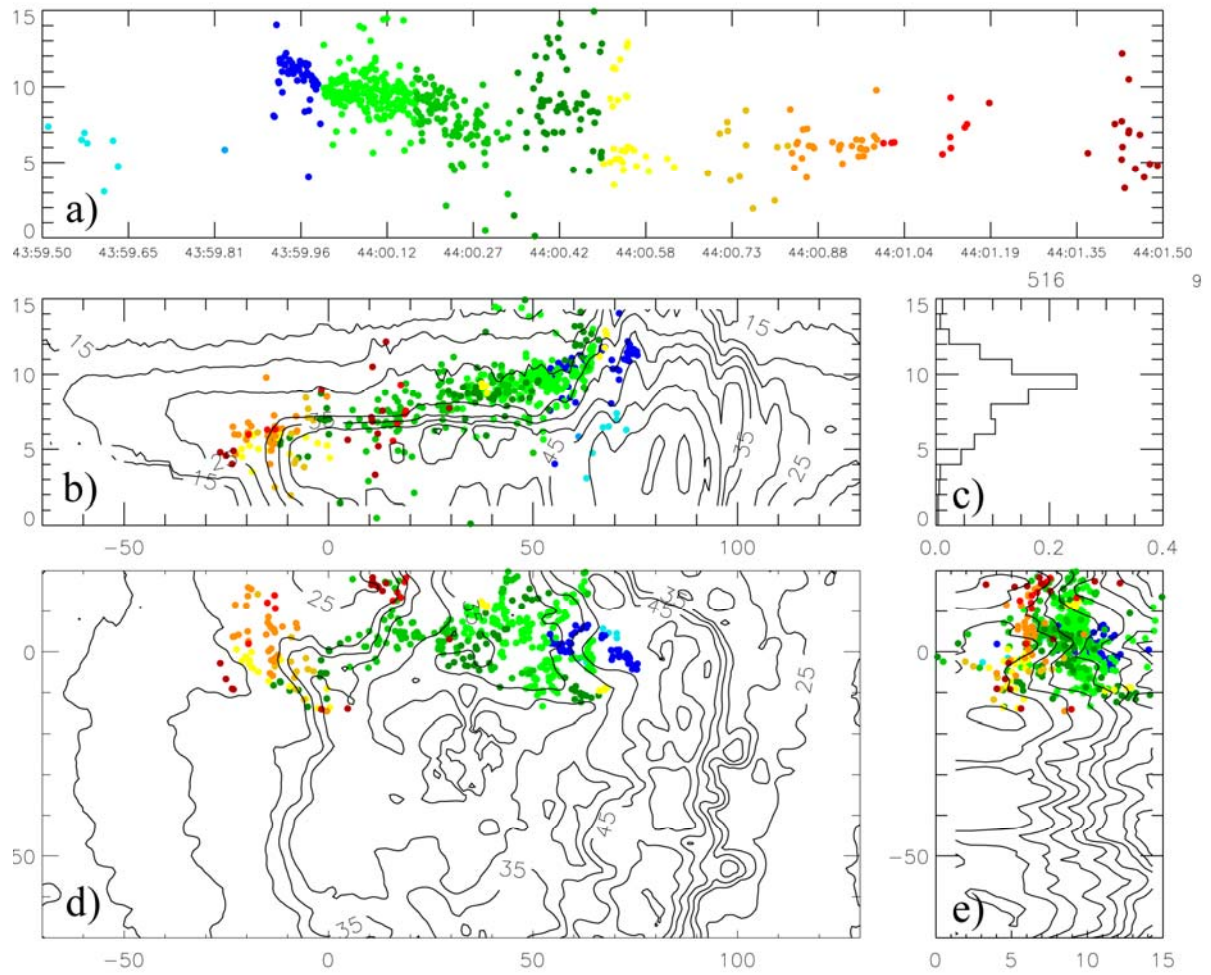


FIG. 3.30: Same as Fig. 3.29 except for a representative flash that originated in the convective region and propagated rearward and downward through the stratiform region. The flash occurred at 12:43 UTC.

Although these flashes are characteristic of their time periods, not all flashes followed the representative pathway. Flashes originating in the stratiform region also contribute to the leveling off appearance of the source densities in the stratiform region.

A modified version of a NASA flash algorithm is once again used to group individual LDAR sources into flashes. The stratiform flash rate was calculated throughout the analysis time by using the flash algorithm (Fig. 3.31). The flash rate, although noisy, increases with time from 5 flashes min^{-1} to over 10 flashes min^{-1} flashes. These flashes are then classified based on where they originated from. The flashes were first classified as to whether or not they originated in the analysis domain consisting of the defined convective, transition, and stratiform regions. Most (70 – 80 %) of the electrical activity in the stratiform region originated within the analysis domain (Fig. 3.32). Therefore, few lightning flashes originate outside the analysis domain and propagate into the stratiform region. The percentage of flashes that originate in the analysis domain within the stratiform region increases from near 20 % (10:40 UTC – 11:29 UTC) to as high as 60 % during later times (e.g., 12:41 UTC). The increase in the amount of flashes originating in the stratiform region occurs as the lightning pathway begins to slant downward into the region and into the melting level.

In order to confirm that the MCS was well within the effective range of the LDAR network, the mean flash extent (calculated by taking the maximum distance from any two VHF sources in a flash) and mean source counts of all flashes are calculated. The mean flash extent for stratiform region flashes originating in both the convective and stratiform regions remained steady throughout the analysis time period. The

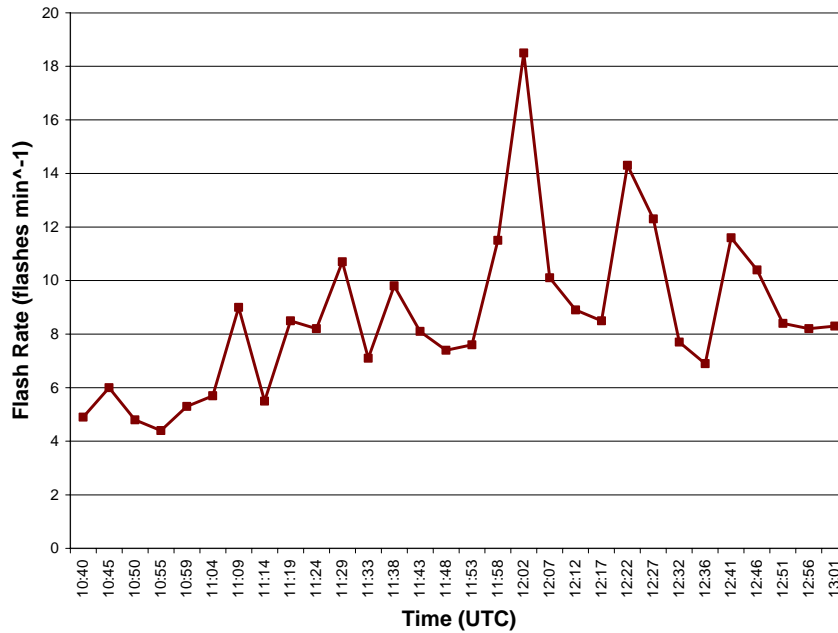


FIG. 3.31: Time series plot of the 21 April MCS stratiform flash rate occurring over ten minute intervals centered on the radar volume scan times.

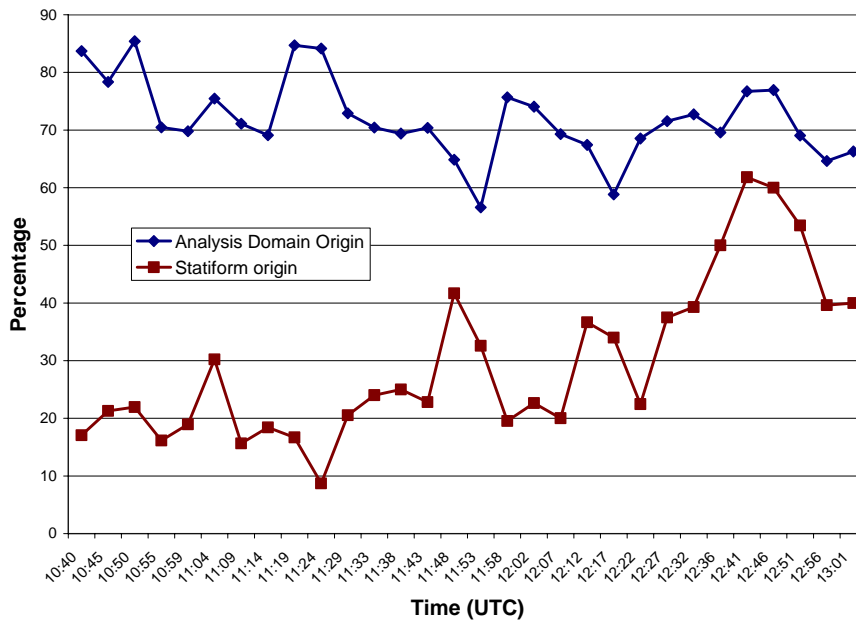


FIG. 3.32: Time series plot of the percentage of the 21 April MCS stratiform flashes originating in the analysis domain (convective, transition, or stratiform regions). Also plotted is the percentage of these flashes that originate in the stratiform region.

convective region flash extents remained near 50 km while the mean stratiform flash extent remained near 20 km (Fig. 3.33). If the MCS was outside the effective range, large flashes would have been broken up into smaller flashes due to the lack of detected VHF sources and the flash extent trend would have increased as the MCS traversed closer to the network. The mean VHF source count of flashes in the convective region generally decreased in time from 500 to 200 VHF sources (Fig. 3.34). This trend is the opposite of what would be expected if there was a range efficiency error, in which more sources would be detected as the system propagated closer to the network center. The stratiform region mean VHF source count remained relatively constant at near 50 VHF sources per flash throughout the time period.

The mean heights of flashes originating in the stratiform region and convective regions that propagate into the stratiform region were calculated. The mean heights of both sets of flashes decrease with time. The convective flashes begin with mean heights of 10 km that slowly decrease down to 9 km with time. The stratiform flash mean heights descend further from 10 km down to 6 km (Fig 3.35). The decrease in flash heights corresponds well with the descent of the lightning pathway into the stratiform region with time (Fig. 3.28). Also of note, the flash origination height of flashes originating in the stratiform region also decreases, from 9 km to 6 km, and stays generally below the mean height of those flashes throughout the time period (Fig. 3.35).

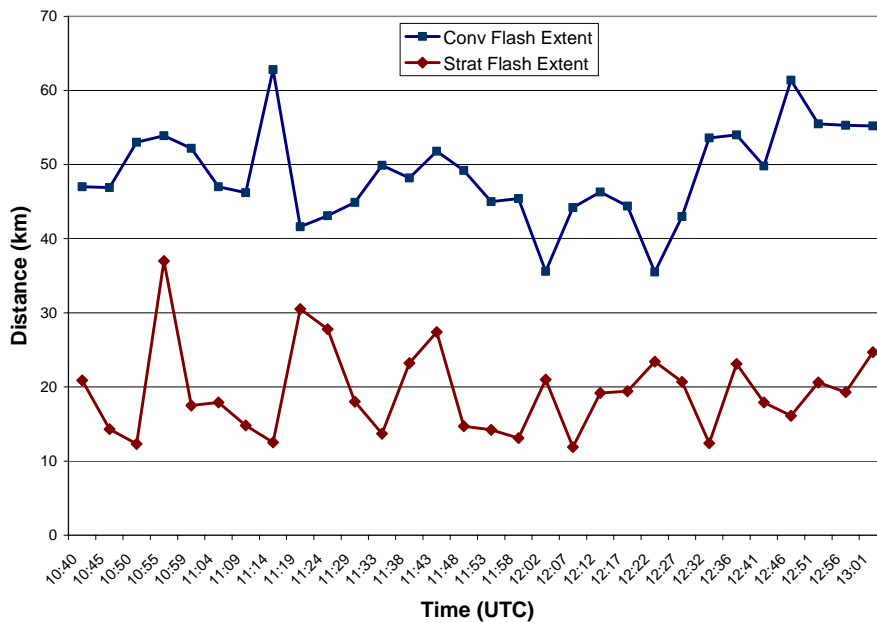


FIG. 3.33: Time series plot of the mean flash extent of stratiform region flashes originating in both the 21 April MCS stratiform and convective regions.

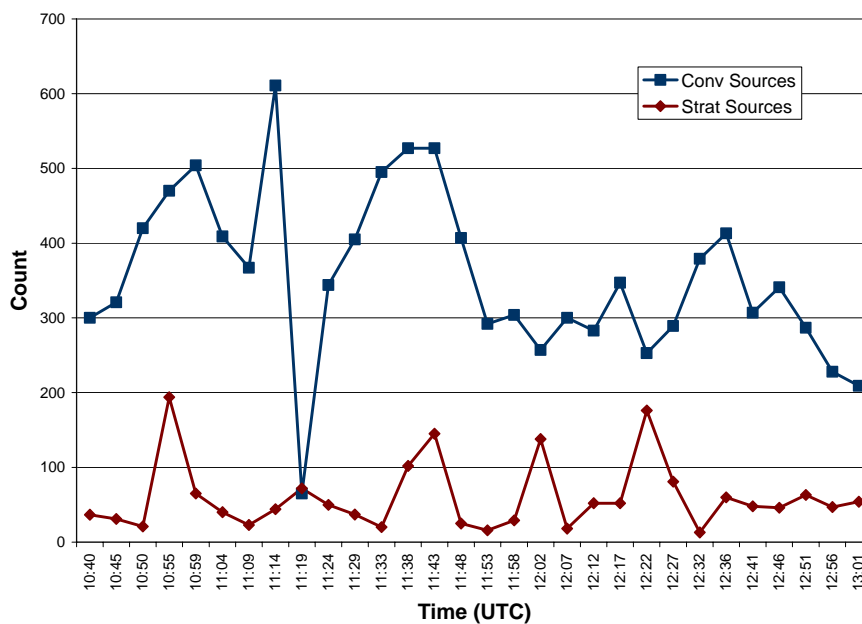


FIG. 3.34: Time series plot of the mean number of VHF sources that compose stratiform region flashes originating in both the 21 April MCS stratiform and convective regions.

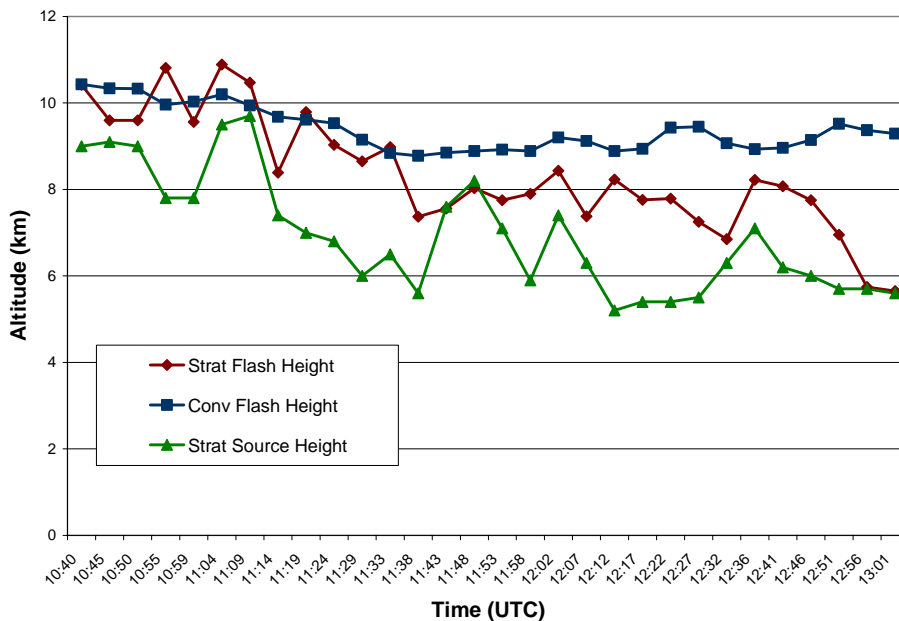


FIG. 3.35: Time series plot of the mean flash heights of stratiform flashes originating in both the 21 April MCS stratiform and convective regions. Also plotted is the mean height of the initiation of flashes originating in the stratiform region.

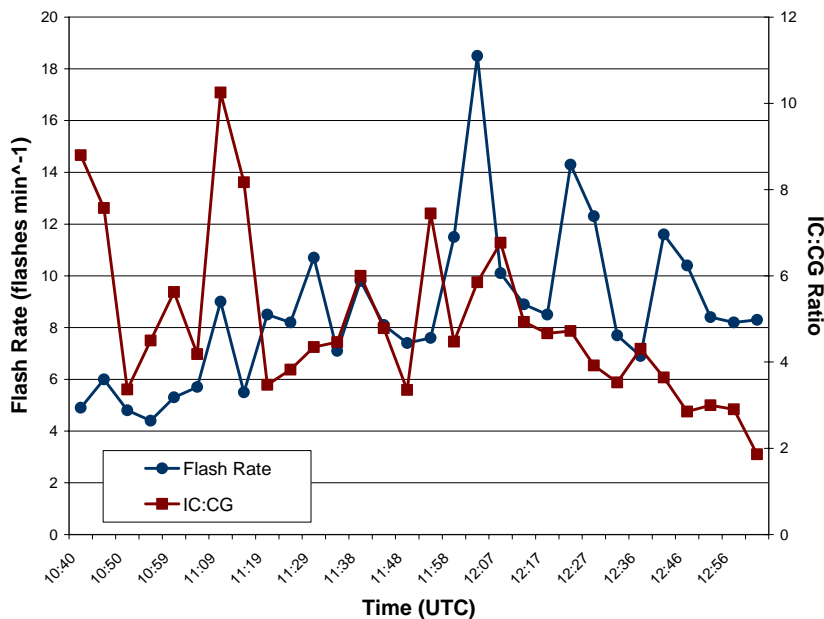


FIG. 3.36: Time series plot of the flash rate and the IC:CG ratio in the 21 April MCS stratiform region over a ten minute time span centered on the radar volume scan time.

3.2.2.2 *National Lightning and Detection Network (NLDN)*

NLDN data is also used to document how CG flashes evolve with the MCS. A time series plot of the total stratiform lightning flash rates and the stratiform IC:CG ratio is shown in Fig. 3.36. The total stratiform flash rate increases steadily as well as the stratiform CG flash rate, which is shown by the decreasing IC:CG ratio by roughly a factor of five from a maximum of ten at 11:09 UTC to a minimum of two at 13:01 UTC (Fig. 3.36). Figure 3.37 shows the stratiform CG flash rate increasing from 0.5 flashes min^{-1} to 3.4 flashes min^{-1} during the analysis time domain. As the CG flash rate increases, so does the percent of positive CGs. The percent of positive CGs during early times is around 10%. As time progresses, the percent positive CGs increases to 37% at 12:46 UTC (Fig. 3.37). The percent of positive CG flashes is much higher in the stratiform region than it is in the convective region. In the convective region, the percent of positive CGs is around 4% with a maximum of 7% (Fig 3.38). Although the percent of positive CGs remains fairly constant as the convective region evolves, the CG rate drops from near 400 CGs in ten minutes at the beginning of the analysis time to close to 125 CGs in ten minutes at the end of the study (Fig. 3.38). Overall, the CG rates decrease in the convective region and increase in the stratiform region as the MCS matures. The percent of positive CGs also increase in the stratiform while the percentage remains constant in the convective region over time.

The mean peak currents of stratiform and convective CGs also differ from one another. The stratiform peak positive currents have a tendency to be greater than the positive peak currents found in the convective region (Fig. 3.39). Also, the peak

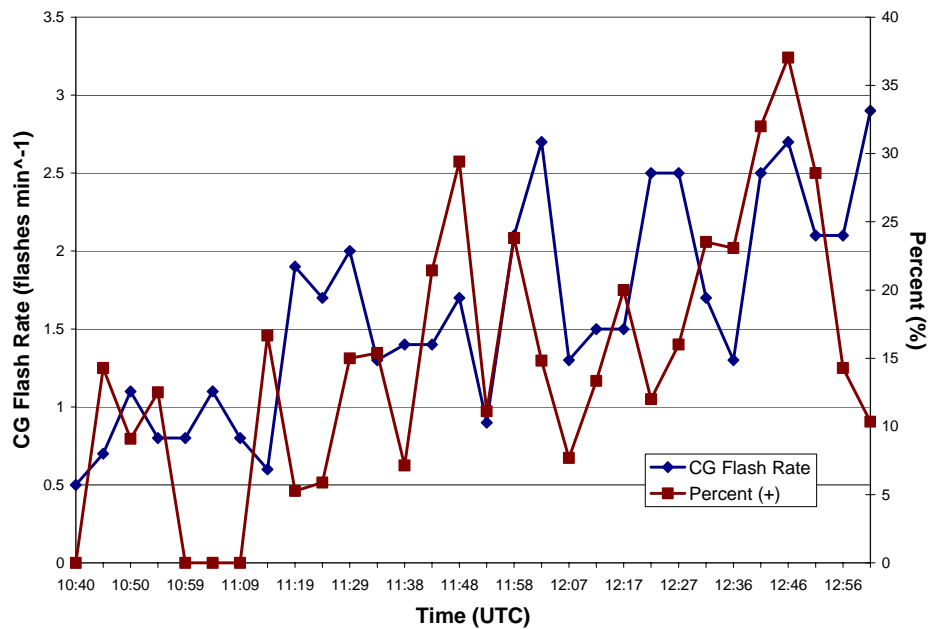


FIG. 3.37: Time series plot of the CG flash rate and percent of positive CGs occurring over a ten minute time period in the 21 April MCS stratiform region.

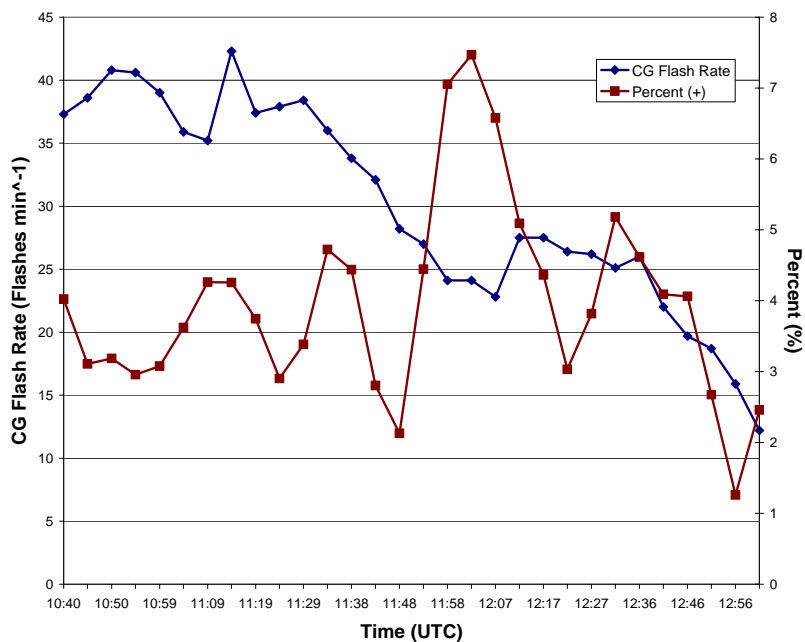


FIG. 3.38: Same as Fig. 3.37 except for in the 21 April MCS convective region.

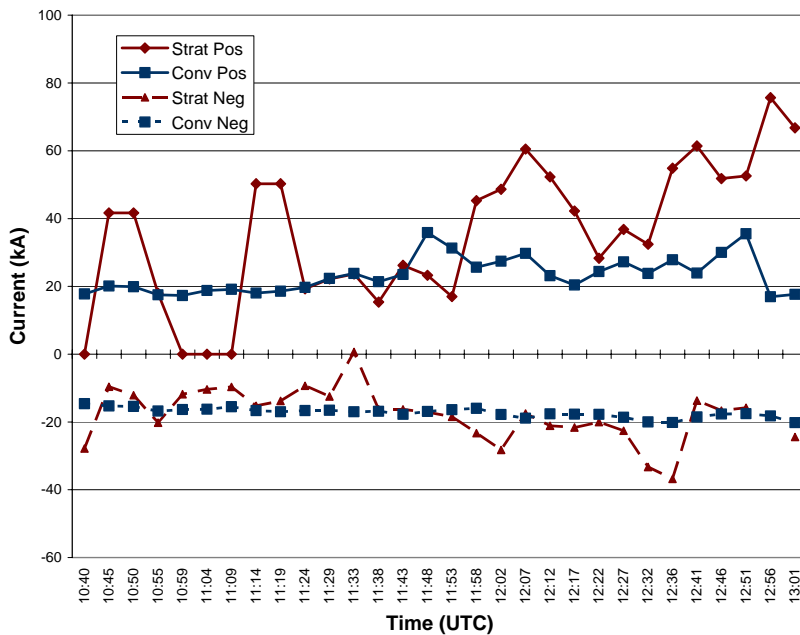


FIG. 3.39: Time series plot of the mean stratiform and convective CG peak currents during the 21 April MCS.

currents in the stratiform region increase from around 40 kA to 70 kA while the convective peak currents increase from 18 kA to 35 kA (Fig. 3.39). The negative peak currents in the convective region stay relatively constant near -17 kA throughout the time period. The stratiform mean negative peak currents have smaller amplitudes (~ -12 kA) than those in the convective region during the first half of the analysis time ($< 11:48$ UTC). However, their amplitudes increase (~ -22 kA) to surpass the convective mean peak currents in the second half of the time period ($> 11:48$ UTC) (Fig. 3.39).

Throughout the analysis time period, 36 LDAR flashes are associated with stratiform region positive CG strokes. The number of flashes originating in the stratiform, non-stratiform, and outside regions, that contain a CG with at least one positive return stroke located in the stratiform region, are 7, 19, and 10, respectively.

After further subdividing the groups based on occurrence before (after) 12:07 UTC, the distributions are 2(5), 6(13), 5(5) in the stratiform, non-stratiform, and outside domains, respectively. These results, plus other positive CG flash statistics, which are taken from the NLDN and LDAR networks, are listed in Table 3.2. The mean LDAR flash extent and LDAR source count of flashes from the non-stratiform region are larger than those from the stratiform region, which can be expected because of the distance the flashes need to propagate in order to tap into the charge in the stratiform region (20-40 km). However, flashes originating in the stratiform region generally propagate in the along line direction and are thus limited by the line-parallel size of the domain. Larger stratiform flash extents may be seen with a larger analysis domain in the line-parallel direction. Interestingly however, even though flashes originating in the non-stratiform domain have longer flash extents, their mean NLDN peak current is less than those that originate in the stratiform region. Not shown in the table are the times in which the CGs occurred. A stratiform initiated flash occurring at 10:45 UTC accounts for the first positive CG. This flash preceded the first non-stratiform initiated positive CG by 45 minutes.

Table 3.2: Summary of flash statistics for stratiform region positive CG flashes that originated in the 21 April MCS stratiform (top) and non-stratiform regions (bottom).

Stratiform			
		Count	
Total		7	
Before(after) 1207 UTC		2(5)	
	source count	extent (km)	current (kA)
Mean	180	49	57
Min	35	27	17
Max	460	71	112
Non-stratiform			
		Count	
Total		19	
Before(after) 1207 UTC		6(13)	
	source count	extent (km)	current (kA)
Mean	807	96	43
Min	259	50	15
Max	1679	125	111

A five panel plot of lightning VHF sources and corresponding maximum reflectivity for an example stratiform flash originating in the convective and stratiform regions are shown in Fig. 3.40 and Fig. 3.41, respectively. The flash originating in the convective region occurred at 12:52 UTC and in the line normal distance versus height panel (Fig. 3.40b) shows similar features as the composite lightning pathway representative of that time (Fig. 3.28d). The flash begins at the top rear of the convective region and propagates 30 km rearward and 6 km downward through the transition zone, seemingly following the slope of the 30 dBZ reflectivity contour. The flash then levels off in two horizontal layers as it travels 50 km rearward through the stratiform region. The first layer occurs just as the flash begins to level off between the

heights of 6 km and 7 km and is 20 km in line-normal extent. The second layer occurs just after the first layer and extends another 30 km rearward into the stratiform region between the heights of 5 km and 6 km. The horizontal layers are more ambiguous in the line parallel distance vs. height plot (Fig. 3.40e). The horizontal extent of this flash is near the mean extent of all flashes originating in the non-stratiform region at 91.5 km (Table 3.2). However, the number of sources is below the mean source count of flashes originating in the non-stratiform regions (Table 3.2), with a source count of 458 (Fig. 3.40d,e). The flash that originates in the stratiform region at 1249 UTC propagates 60 km in the line parallel direction (Fig. 3.41). The majority of the sources of this flash occur right above the melting level between the heights of 4 km and 5 km. There is a secondary maximum of sources that occur between the heights of 6 km and 7 km. This flash has an extent of 66 km which is near the maximum extent seen by flashes originating in the stratiform region and has 254 sources, which is above average of flashes originating in the stratiform region (Table 3.2).

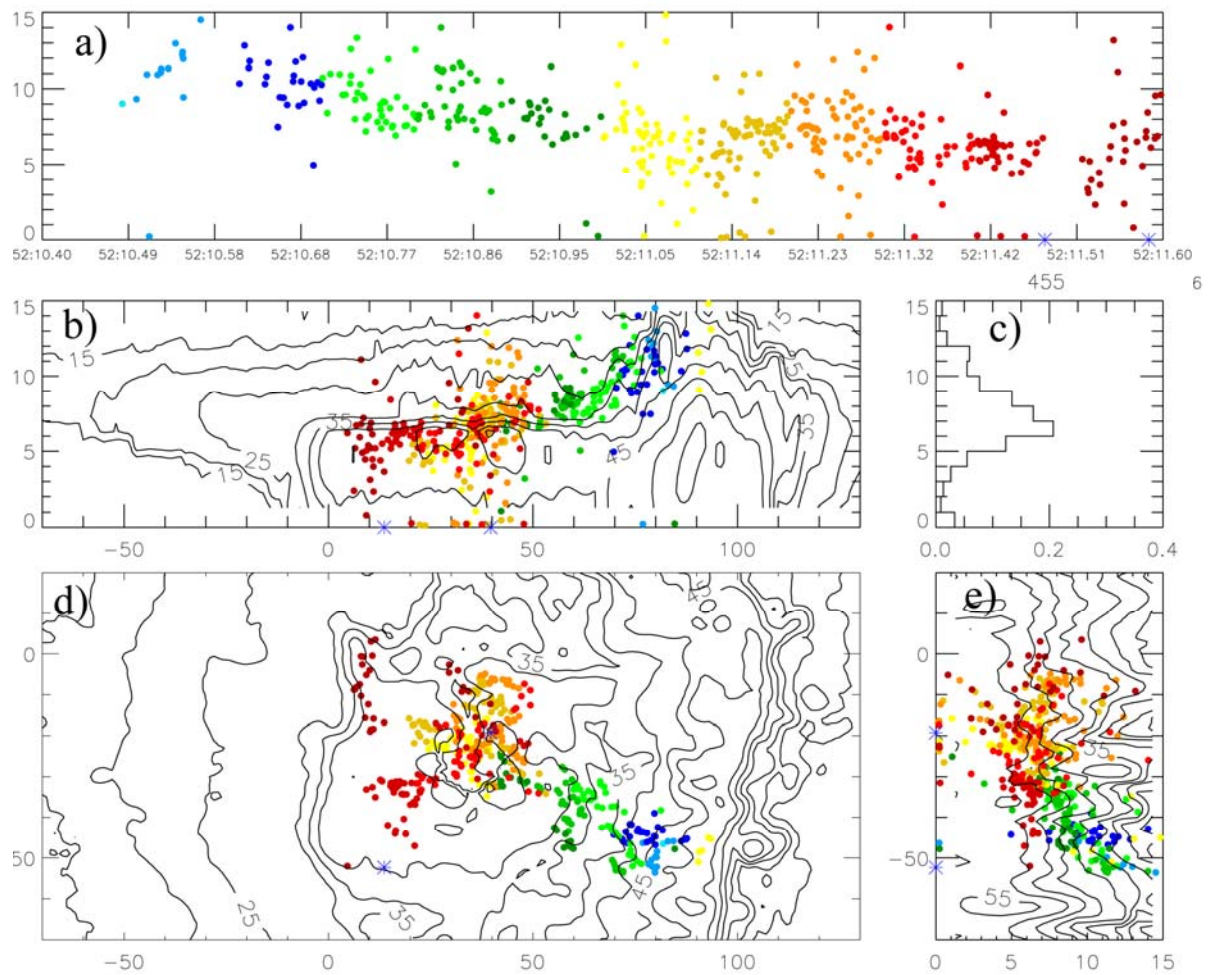


FIG. 3.40: Same as Fig. 3.29 except with a +CG flash originating from the convective line at 12:52 UTC. Triangles indicate negative CG strokes while *s indicate positive CG strokes.

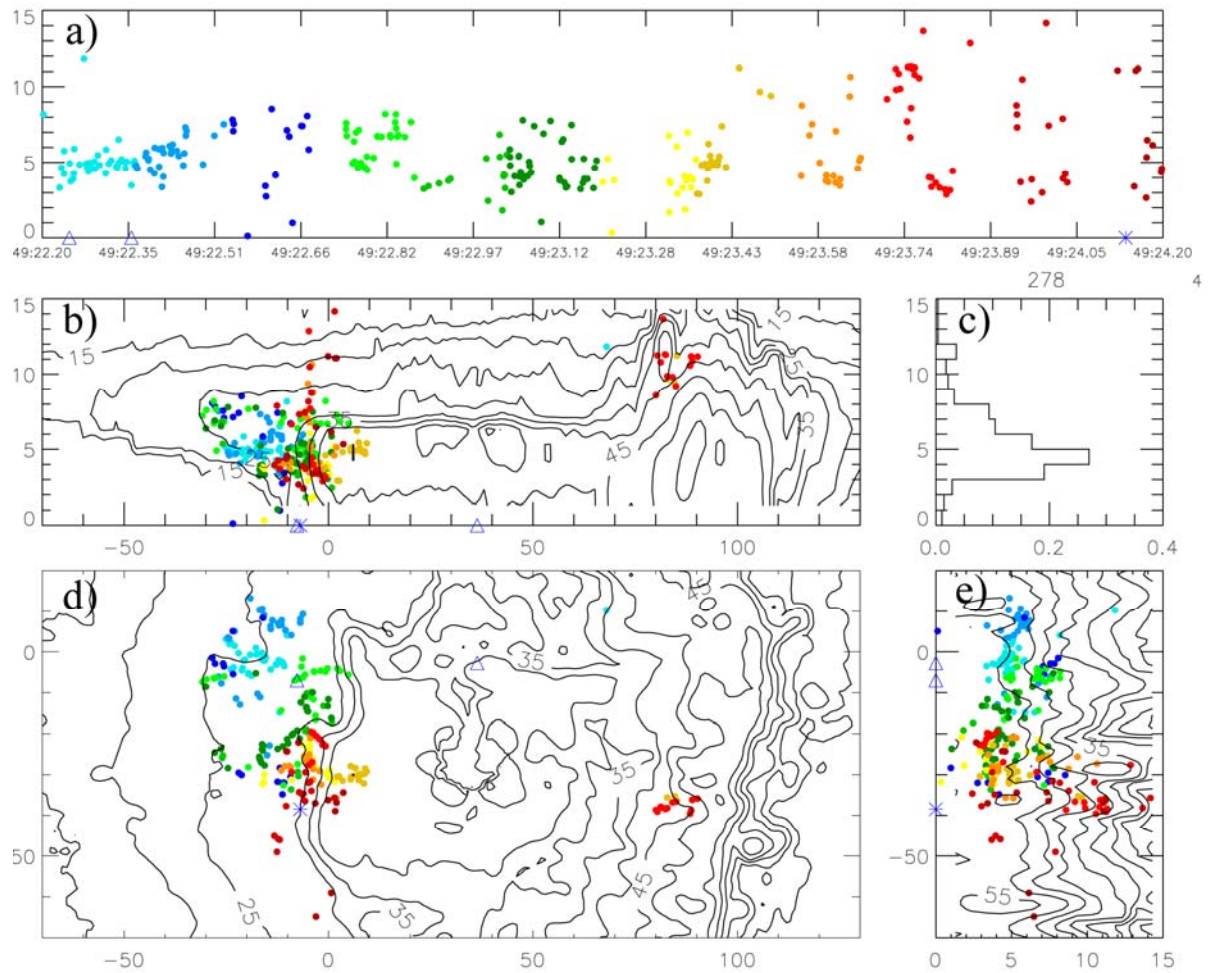


FIG. 3.41: Same as Fig. 3.29 except with a +CG flash originating from the stratiform region at 12:49 UTC. Triangles indicate negative CG strokes while *s indicate positive CG strokes.

4. DISCUSSION

Many MCSs have passed within range of the Houston LDAR network since its deployment. On 31 October 2005 and 21 April 2006, two LLTS MCSs evolved as they traversed the network and showed significant development of the stratiform region. The total lightning and radar reflectivity characteristics of the evolving convective and stratiform regions of both MCSs are presented. The objective is to improve our knowledge regarding total lightning structure and charging processes in the trailing stratiform region and their relationship to radar structure and precipitation properties. The radar and lightning properties of these two MCSs will now be discussed.

Both MCSs show a remarkably similar evolution of the lightning pathway between the convective and stratiform regions. In early stages, the VHF source density showed a lightning pathway extending horizontally rearward for 40 - 50 km from the top of the convective region at 9 to 12 km altitude into the stratiform region. This initial stage of the lightning pathway has not been observed in previous studies. As the MCS matures and the stratiform region intensifies, the lightning pathway evolves into the slanted structure with more lightning sources occurring at and above the bright band at lower levels (i.e., 4-7 km) (Figs. 3.8, 3.28). Toward the end of the analysis time period, by 23:32 (12:41) UTC in the October (April) MCS, the line-normal lightning pathway observed shows similar characteristics of a mature LLTS MCS seen in previous studies (Carey et al. 2005, Dotzek et al. 2005) and is associated with the conceptual model presented in FIG. 1.13.

Small ice crystals that are ejected from the top of the convective line during the early stages are assumed to have negligible fall speeds. These ice crystals, due to the non-inductive charging mechanism by rebounding collisions by ice particles, are expected to carry positive charge (e.g., Rutledge and MacGorman, 1988). As these particles travel toward the stratiform region they remain positively charged and any lightning activity that taps into this charged region will propagate straight rearward and show a structure similar to the first LDAR source density plot (Figs. 3.8, 3.28). The early stages of the lightning structure appear similar to the conceptual model of charge densities presented by Stolzenburg et al. (1998) (Fig. 1.11), which has charge layers extending horizontally rearward in the stratiform region. The soundings that formed the basis of this model may have been from developing MCSs or in portions of the MCS without a developed stratiform region. The slanting lightning pathway may be explained by lightning continuing to tap into the charge of the falling and growing ice particles. The strengthening mesoscale updraft increases the presence of supercooled water and, in combination with the enlarged ice particles, produces an active mixed phase region, which can result in non-inductive collisional charging (e.g., Rutledge et al. 1990, Williams et al. 1994, Schuur and Rutledge 2000a,b).

The slanting pathway may also be confirmed by the lowering of mean flash VHF source heights. As the systems matured, the flash heights lowered. A decrease of overall MCS VHF lightning from upper (7-11.5 km) to lower (2-5 km) levels was also observed by Lyons et al. (2003) in their study of two maturing MCSs. A similar transition is seen in positive CG flashes in this study, along with a lowering of all

stratiform flashes seen in these two MCSs. Lyons et al. (2003) found that an increase of sprite production coincided with lowering of the flash heights as MCSs mature.

Although no sprite observations are available for this study, flash heights are seen to decrease with time for both MCSs and therefore, positive CGs could be more effective producers of sprites as the MCSs matured (Figs. 3.15, 3.35). Along with the lowering of flash heights and slanting lightning pathway, the stratiform region also experienced an increase in flashes. The total flash rates double in time and the percentage of flashes originating in the stratiform region increased from 10 - 20 % to 50 – 60% in both stratiform regions of the MCSs (Figs. 3.11, 3.12, 3.31, 3.32).

The observed evolution in radar reflectivity in the time series plots and CFADs may partially explain the changes in the lightning pathway, source heights, and increased electrical activity in the stratiform region. In both cases, the stratiform mean reflectivity at low levels (Figs. 3.5a, 3.25a) increased with time while the mean reflectivities in the convective region (Figs. 3.5b, 3.25b) decreased. This may be explained by the Carey et al. (2005) conceptual model (Fig. 1.3) where small ice particles are advected from the top of the convective clouds into the stratiform region by the storm relative front-to-rear flow. As the ice particles fall, they grow by deposition and aggregation in the mesoscale updraft. Upon reaching the melting level, they begin to melt, creating the radar bright band. Thus, increasing stratiform reflectivity implies strengthening of the mesoscale updraft, which further implies increased in-situ charging and lightning generation (e.g., Rutledge et al., 1990; Petersen and Rutledge, 1994). The mean reflectivity near the melting level increases significantly from 26 dBZ to 34 dBZ in the 31 October 2005

MCS (Fig. 3.6) and from 32 dBZ to 38 dBZ in the 21 April 2006 MCS (Fig. 3.26). The areas of the analyzed stratiform regions also increased, quadrupling in both cases.

As the stratiform regions of the two MCSs are developing, the convective region is weakening. The mean reflectivities at all heights decrease (Figs. 3.5b, 3.25b) along with its area (Figs. 3.6, 3.26). Biggerstaff and Houze (1991) found that the most intense convective cells are responsible for the most intense stratiform precipitation to due particle projection paths. The lag relationship between peak reflectivities of the two regions is thought to be due to the time it takes the particles ejected from the convective line to be carried by the front-to-rear flow into the stratiform region and grow while falling through the mesoscale updraft. This lag relationship is also seen in the difference in the rainfall totals between the convective and stratiform regions of both MCSs in this study. As the convective line weakened, rain totals dwindle in both MCSs. On the other hand, as the stratiform regions intensified, rain totals increased. Rutledge and MacGorman (1988) found that the peak rainfall rates in the stratiform region corresponded to peak positive CG flash rates, which is also seen in both MCSs observed in this study. In agreement with their study, the positive CG flash rates continued to rise in the stratiform region as its rainfall rate increased (Figs. 3.17, 3.37). Both MCSs also experienced an evolving lightning pathway, lowering flash heights, increasing stratiform flash rate, and an increasing percentage of flashes originating in the stratiform region during the same time period of stratiform growth and development.

The increased stratiform electrification could possibly be explained by developing charge layers. Schuur and Rutledge (2000a) found charge transitions near

the melting level and near the -12°C isotherm in the stratiform region of a symmetric MCS. Melting driven charging mechanisms are thought to be the cause of the charge transition near the melting level (e.g., Shepherd et al. 1996). While non-inductive collisional charging may also play a role in charging near the melting level, it is speculated to play a more significant role in the charge transitions near the -12°C level (Schuur and Rutledge 2000a,b). The mean stratiform flash heights occurred in a layer between 6 - 8 km, which is just above the -12°C isotherm (6 km) (Figs. 3.15, 3.35). Both in-situ charging (melting and collisional) mechanisms would enhance the charging in and above the melting layer and play a role in both the horizontal extent of the lightning pathway after its descent into the stratiform region and the increased flash rate in the stratiform region, along with increased flash initiation. Charge advection is also likely to increase stratiform electrification, especially at higher levels (e.g., Stolzenburg 1994). The advection of charged particles played a primary role, with a secondary contribution from in-situ NIC charging, in a modeling study by Schuur and Rutledge (2000b). They also noted extensive layering of charge over the radar bright band that was associated primarily with in-situ charging. The slanted charge layer, along with layering of charge over the bright band is consistent with the slanting lightning pathway seen in this study (Figs. 3.4d, 3.28d).

Charge advection and in-situ charging mechanisms likely both play a role in the charge structure conducive to increased production of stratiform CGs. A majority, 19 of 26 (73%), of flashes originating in the analysis domain with a NLDN identified positive ground stroke in the stratiform region, originate in the convective or transition regions

and propagate into the stratiform region before descending to the earth in the April MCS. The remaining seven positive ground flashes originate in the stratiform region. These numbers are comparable to those seen in Lang et al. (2004) and indicate that charge advection may be an important factor in positive CG production in the stratiform region of LLTS MCS. However, only 5 of 11 (45 %) flashes with a positive stroke originated from the convective region in the October MCS. Positive stratiform CG production, which is initiated in both the stratiform and convective regions, increases after 23:15 (12:07) UTC in the October (April) MCS, as radar reflectivity in the stratiform region increases. Of all the LDAR flashes associated with NDNLN positive CGs, 70% occurred after 12:07 UTC in the April MCS and 82% occurred after 23:15 UTC in the October MCS (Tables 3.1, 3.2). Consistent with the modeling study of Schuur and Rutledge (2000b), results suggest that both charge advection and in-situ charging mechanisms likely play a role in stratiform charging. However, in-situ charging is likely the cause of greater positive peak currents associated with stratiform flashes. In initial time periods, the positive peak currents found in the stratiform region are comparable to those in the convective regions. However, later times indicate higher positive peak currents found in the stratiform region over the convective region as the mesoscale updraft increases and the stratiform region develops and becomes more intense. Also, the positive peak currents of flashes originating in the stratiform region are higher than those originating in the convective region and propagating into the stratiform region then to ground (Tables 3.1, 3.2). This may be due to the high density positive charge normally found above the melting level once the bright band is developed (Schuur and Rutledge 2000a,

Shepherd et al. 1996). As the stratiform region gains intensity, more positive ground flashes originate in both the convective and stratiform regions, overall flash rate increases in the stratiform region, and the lightning pathway, which extends from the convective line rearward into the stratiform region, evolves from extending horizontally rearward to a slanted rearward and downward pathway.

5. CONCLUSIONS

MCSs are some of the largest convective systems and produce a wide variety of weather including damaging winds, hail, tornadoes, and flooding. They are also prolific producers of lightning, which is the second most fatal weather related event. This study examines the total lightning and radar reflectivity structure of two MCSs, occurring on 31 October 2005 and 21 April 2006, that traversed Houston within the effective range of the LDAR network in Houston, TX. The lightning characteristics of both MCSs evolved with intensification of their stratiform regions and weakening of their convective regions. In summary:

- The lightning pathway from the convective to the stratiform region initially extends horizontally rearward from the top of the convective region into the stratiform region. As the MCS matures, the pathway slants rearward ~ 50 km and downward by ~ 6 km into the stratiform region and levels off near the bright band just above the melting level. The slanting feature of the lightning pathway could be the result of positively charged ice particles advected from the convective region into the stratiform region and in-situ processes.
- The evolution of the lightning pathway may also be related to the development of the stratiform region and the radar bright band. The stratiform areas quadrupled in area and mean stratiform reflectivity increased significantly at all heights, especially near the melting level.
- Stratiform flash rates and the percentage of flashes originating in the stratiform region increase while mean flash heights decrease as the stratiform

region develops and the lightning pathway slants down toward the melting level. The lowering of flash heights could have been indicative of the production of sprites as these MCSs matured. Charge advection and in-situ charging (NIC melting and collisional charging) as the mesoscale updraft develops are suggested to cause enhanced charge layers and the increased electrical activity.

- CGs also increase as the stratiform region intensifies. Positive CG currents found in the stratiform are generally higher than those found in the convective region and increase in time. Also, stratiform region flashes originating in the stratiform region produce higher positive CG currents than those originating in the convective region and propagating into the stratiform and then to ground.

Although these two MCSs have similar evolving lightning structure and radar characteristics, further studies are needed to establish charging mechanisms and charge layers in the stratiform region. These studies should focus on the stratiform charge distributions and the microphysical conditions favorable for charging by simultaneous Electric Field Meter (EFM) launches and collection of in-situ microphysical data during the evolution of a MCS. Also, a more in depth look at the detailed charge structure indicated by individual flashes from both the convective and stratiform regions depicted by lightning mapping systems could also refine our knowledge of the charge structure in the stratiform region (Lang and Rutledge 2007). Studies should also build on the discussion of whether stratiform region positive CG flashes originate in the stratiform

region or in the convective region and propagate downward through the stratiform region and finally to the earth. Finally, it would be interesting to investigate whether sprite producing positive CG flashes in the stratiform region are initiated primarily locally (i.e., in the stratiform region) or remotely (in the transition zone or convection). In our study, the mean VHF lightning heights for both types of stratiform region positive CG flashes lower as the MCS matures, which could be indicative of a greater possibility of sprites (Lyons et al. 2003).

REFERENCES

- Anagnostou, E.N., C.A. Morales, and T. Dinku, 2001: The use of TRMM precipitation radar observations in determining ground radar calibration biases. *J. Atmos. Ocean Tech.*, **18**, 616 – 628.
- Aufdermaur, A.N., and D.A. Johnson, 1972: Charge separation due to riming in an electric field. *Q. J. Roy. Meteor. Soc.*, **98**, 369-382.
- Baker, M.B., and J.G. Dash, 1994: Mechanism of charge transfer between colliding ice particles in thunderstorms. *J. Geophys. Res.*, **99**, 10621-10626.
- Biggerstaff, M.I., and R.A. Houze, Jr., 1991: Kinematic and precipitation structure of the 10-11 June 1985 squall line. *Mon. Wea. Rev.*, **119**, 3034 -3065.
- Blanchard, D.O., 1990: Mesoscale convective patterns of the southern High Plains. *Bull. Amer. Meteor. Soc.*, **71**, 994-1005.
- Bluestein, H.B., and M.H. Jain, 1985: Formation of mesoscale lines of precipitation: Severe squall lines in Oklahoma during the spring. *J. Atmos. Sci.*, **42**, 1711-1732.
- , G.T. Marx, and M.H. Jain, 1987: Formation of mesoscale lines of precipitation: Non-severe squall lines in Oklahoma during the spring. *J. Atmos. Sci.*, **115**, 2719-2727.
- Boccippio, D. J., 2002: Lightning scaling relations revisited. *J. Atmos. Sci.*, **59**, 1086-1104.
- Brown, R.A., V.T. Wood, and D. Sirmans, 2000: Improved WSR-88D scanning strategies for convective storms. *Weather Forecast*, **15**, 208-220.
- Carey, L.D., and S.A. Rutledge, 2003: Characteristics of cloud-to-ground lightning in severe and non-severe storms over the central United States from 1989-98. *J. Geophys. Res.*, **108**, NO. D15, 4483, doi:10.1029/2002JD002951.
- , M.J. Murphy, T.L. McCormick, and N.W.S. Demetriades, 2005: Lightning location relative to storm structure in a leading-line, trailing-stratiform mesoscale convective system. *J. Geophys. Res.*, **110**, doi: 10.1029/2003JD00437.
- Chauzy, S., and S. Soula, 1999: Contribution of the ground corona ions to the convective charging mechanism. *Atmos. Res.*, **51**, 279-300.

- Coleman, L.M., T.C. Marshall, M. Stolzenburg, T. Hamlin, P.R. Krehbiel, W. Rison, and R.J. Thomas, 2003: Effects of charge and electrostatic potential on lightning propagation. *J. Geophys. Res.*, **108**, 4298, doi:10.1029/2002JD002718.
- Cressman, G.P., 1959: An operational objective analysis system. *Mon. Wea. Rev.*, **87**, 367-364.
- Crum, T.D., R.L. Alberty, and D.W. Burgess, 1993: Recording, archiving, and using WSR-88D data. *Bull. Amer. Meteor. Soc.*, **74**, 645-653.
- Cummins, K.L., R.O. Burnett, W.L. Hiscox, and A.E. Pifer, 1993: Line reliability and fault analysis using the National Lightning Detection Network, *Precise Measurements in Power Conference*, Arlington, VA., October 27 – 29.
- , M.J. Murphy, E.A. Bardo, W.L. Hiscox, R.B. Pyle, and A.E. Pifer, 1998: A combined TOA/MDF technology upgrade of the U.S. National Lightning Detection Network, *J. Geophys. Res.*, **98**, 9035-9044.
- , J.A. Cramer, C.J. Biagi, E.P. Krider, J. Jerauld, M.A. Uman, and V.A. Rakov, 2006 : The U.S. National Lightning Detection Network: post-upgrade status. *2nd Conf. Met. Applications of Lightning Data*, Atlanta, AMS.
- Curran, E.B., R.L. Holle, and R.E. Lopez, 2000: Lightning casualties and damages in the United States from 1959 to 1994. *J. Climate*, **13**, 3448-3464.
- Dotzek, N., R.M. Rabin, L.D. Carey, D.R. MacGorman, T. L. McCormick, N. W. Demetriades, M. J. Murphy, and R. L. Holle, 2005: Lightning activity related to satellite and radar observations of a mesoscale convective system over Texas on 7-8 April 2002, *Atmos. Res.*, **76**, 127-166.
- Drake, J.C. 1968: Electrification accompanying the melting of ice particles. *Q.J.R. Meteor. Soc.*, **94**, 176-191.
- Ely, B.L., R.E. Orville, and L.D. Carey, 2006: Houston LDAR network performance, data usage, and first results. *Second Conference on the Meteorological Applications of Lightning Data.*, Atlanta, AMS.
- , R. E. Orville, L. D. Carey, and C. L. Hodapp, 2007: Evolution of the total lightning structure in a leading-line, trailing-stratiform mesoscale convective system over Houston, Texas. *J. of Geophys. Res.*, **in revision**.
- Fritsch, J.M., R.J. Kane, and C.R. Chelius, 1986: The contribution of mesoscale convective weather systems to the warm-season precipitation in the United States. *J. Climate Appl. Meteor.*, **25**, 1333-1345.

- Gaskell, W., and A.J. Illingsworth, 1980: Charge-transfer accompanying individual collisions between ice particles and its role in thunderstorm electrification. *Quart. J. Roy. Meteor. Soc.*, **106**, 841-854.
- Goodman, S.J., and D.R. MacGorman, 1986: Cloud-to-ground lightning activity in mesoscale convective complexes. *Mon. Wea. Rev.*, **114**, 2320-2328.
- , T. Blakeslee, H. Christian, W. Koshak, J. Bailey, J. Hall, E. McCaul, D. Buechler, C. Darden, J. Burks, T. Bradshaw, and P. Gatlin, 2005: The north Alabama lightning mapping array: Recent severe storm observations and future prospects, *Atmo. Res.*, **76**, 423-437.
- Holle, R.L., A.I. Watson, R.E. Lopez, D.R. MacGorman, and R. Ortiz, 1994: The life cycle of lightning and severe weather in a 3-4 June 1985 PRE-STORM mesoscale convective system. *Mon. Wea. Rev.*, **122**, 1798-1808.
- , R.E. Lopez, L.J. Arnold, and J. Endres, 1996: Insured lightning caused property damage in three western states. *J. Appl. Meteor.*, **35**, 1344-1351.
- Houze, R.A., Jr., S.A. Rutledge, M.I. Biggerstaff, and B.F. Smull, 1989: Interpretation of Doppler weather radar displays of midlatitudes mesoscale convective systems. *Bull. Amer. Meteor. Soc.*, **70**, 608-619.
- , B.F. Smull, and P. Dodge, 1990: Mesoscale organization of springtime rainstorms in Oklahoma. *Mon. Wea. Rev.*, **118**, 613-654.
- , 2004: Mesoscale Convective Systems. *Rev. Geophys.*, **42**, RG4003, doi: 10.1029/2004RG000150.
- Illingsworth, A.J., 1985: Charge separation in thunderstorms: Small scale processes. *Quart. J. Roy. Meteor. Soc.*, **90**, 6026-6032.
- Jayaratne, E.R., C.P.R. Saunders, and J. Hallett, 1983: Laboratory studies of the charging of soft-hail during ice crystal interactions. *Quart. J. Roy. Meteor. Soc.*, **109**, 609-630.
- Keith, W.D., and C.P.R. Saunders, 1990: Charging of aircraft-high-velocity collisions. *J. of Aircraft*, **27**, 218-222
- Krehbiel, P.R., 1986: The electrical structure of thunderstorms. *The Earth's Electrical Environment*, National Academy Press, Washington, DC, 90-113.
- , R. J. Thomas, W. Rison, T. Hamlin, J. Harlin, and M. Davis, 2000: GPS-based mapping system reveals lightning inside storms, *Eos Trans.*, **81**, 21-25.

- Krider, E.P., R.C. Noggle, A.E. Pifer, and D.L. Vance, 1980: Lightning direction finding systems for forest fire detection. *Bull. Amer. Meteor. Soc.*, **61**, 980 – 986.
- Lang, T.J., S.A. Rutledge, and K.C. Wiens, 2004: Origins of positive cloud-to-ground lightning flashes in the stratiform region of a mesoscale convective system. *Geophys. Res. Lett.*, **31**, L10105, doi:10.1029/2004GL019823.
- Loehrer, S.M., and R.H. Johnson, 1995: Surface pressure and precipitation life cycle characteristics of PRE-STORM mesoscale convective systems, *Mon. Wea. Rev.*, **123**, 600-621.
- Lopez, R.E., R.L. Holle, T.A. Heikamp, M. Boyson, M. Cherington, and K. Langford, 1993: The underreporting of lightning injuries and deaths in Colorado. *Bull. Amer. Meteor. Soc.*, **74**, 2171-2178.
- MacGorman, D. R., and W. D. Rust, 1998: *The Electrical Nature of Storms*, Oxford Univ. Press, New York, 422 pp.
- Maddox, R.A, 1983: Large-scale meteorological conditions associated with midlatitudes mesoscale convective complexes. *Mon. Wea. Rev.*, **111**, 1475-1493.
- Marshall, T.C., and W.D. Rust, 1993: Two types of vertical electrical structures in stratiform precipitation regions of mesoscale convective systems. *Bull. Amer. Meteor. Soc.*, **74**, 2159-2170.
- Mazur, V., and W.D. Rust, 1983: Lightning propagation and flash density in squall lines as determined with radar. *J. Geophys. Res.*, **88**, 1495-1502.
- McCormick, T.L., 2003: Three-dimensional radar and total lightning characteristics of mesoscale convective systems. M.S. Thesis, Dept. of Marine, Earth, and Atmos Sci., North Carolina State University
- Moore, C.B., B. and Vonnegut, 1977: The thundercloud. *Lightning*, Academic Press, New York, NY, 51-98.
- Orville, R.E., R.W. Henderson, and L.F. Bosart, 1988: Bipole patterns revealed by lightning locations in mesoscale storm systems. *Geophys. Res. Lett.*, **15**, 129-132.
- , 1991: Lightning ground flash density in the contiguous United States-1989. *Mon. Wea. Rev.*, **119**, 573-577.
- , and G.R. Huffines, 2001: Cloud-to-ground lightning in the United States: NLDN results in the first decade. *Mon. Wea. Rev.*, **129**, 1179-1193.

- Oye D., and M. Case, 1995: REORDER: A program for gridding radar data. Research Data program, Atmospheric Technology Division, National Center for Atmospheric Research, Boulder, CO.
- Parker, M.D., and R.H. Johnson, 2000: Organizational modes of midlatitude mesoscale convective systems. *Mon. Wea. Rev.*, **128**, 3413-3436.
- Pasko, V.P., U.S. Inan, and T.F. Bell, 1997: Sprites produced by quasi-electrostatic heating and ionization in the lower ionosphere. *J. Geophys. Res.*, 102, 4529 – 4561.
- Petersen, W.A., and S.A. Rutledge, 1992: Some characteristics of cloud-to-ground lightning in tropical northern Australia. *J. Geophys. Res.*, **97**, 11553-11560
- Rakov, V.A., and M.A. Uman, 2003: *Lightning*, Cambridge University Press,, New York, NY, 687 pp.
- Rinehart, R.E., 2004: *Radar for meteorologists*, Rinehart Publications, Columbia, MO, 482 pp.
- Rison, W., R.J. Thomas, P.R. Krehbiel, T. Hamlin, and J. Harlin, 1999: A GPS-based three-dimensional lightning mapping system: Initial observations in central New Mexico, *Geophys. Res. Lett.*, **26**, 3573-3576.
- Rust, W.D., D.R. MacGorman, and W.L. Taylor, 1985: Photographic verification of continuing current in positive cloud to ground flashes. *J. Geophys. Res.* **90**, 6144-6146.
- Rutledge, S.A., and R.A. Houze, 1987: A diagnostic modeling study of the trailing-stratiform region of a mid-latitude squall line. *J. Atmos. Sci.*, **44**, 2640-2656.
- , R.A. Houze, M.I. Biggerstaff, and T. Matejka, 1988: The Oklahoma-Kansas mesoscale convective system of 10-11 June 1985: Precipitation structure and single Doppler radar analysis. *Mon. Wea. Rev.*, **116**, 1409-1430.
- and D. R. MacGorman, 1988: Cloud-to-ground lightning activity in the 10-11 June 1985 mesoscale convective system observed during the Oklahoma-Kansas PRE-STORM project. *Mon. Wea. Rev.*, **116**, 1393-1408, 1988.
- , C. Lu, and D.R. MacGorman, 1990: Positive cloud-to-ground lightning in mesoscale convective systems. *J. Atmos. Sci.*, **47**, 2085-2100.

- and W.A. Petersen, 1994: Vertical radar reflectivity structure and cloud-to-ground lightning in the stratiform region of MCSs: Further evidence of in situ charging in the stratiform region. *Mon. Wea. Rev.*, **122**, 1760-1776.
- Sartor, D., 1954: A laboratory investigation of collision efficiencies, coalescence and electrical charging of simulated cloud drops. *J. Meteor.*, **11**, 91-103.
- Saunders, C.P.R., W.D. Kieth, and R.P. MMitzeva, 1991: The effect of liquid water on thunderstorm charging. *J. Geophys. Res.*, **96**, 11007-11017.
- , 1993: A review of thunderstorm electrification processes. *J. Appl. Meteor.*, **32**, 642-655.
- , 1994: Thunderstorm electrification laboratory experiments and charging mechanisms. *J. Geophys. Res.*, **99**, 10773-10779.
- Schuur, T.J., B.F. Smull, W.D. Rust, and T.C. Marshall, 1991: Electrical and kinematic structure of the stratiform precipitation region trailing an Oklahoma squall line. *J. Atmos. Sci.*, **48**, 825-842.
- , and S.A. Rutledge, 2000a: Electrification of stratiform regions in mesoscale convective systems. Part 1: An observational comparison of symmetric and asymmetric MCSs. *J. Atmos. Sci.*, **57**, 1961-1982.
- , and S.A. Rutledge, 2000b: Electrification of stratiform regions in mesoscale convective systems. Part 2: Two-dimensional numerical model simulations of a symmetric MCS. *J. Atmos. Sci.*, **57**, 1983-2006.
- Shao, X.M., and P.R. Krehbiel, 1996: The spatial and temporal development of intracloud lightning. *J. Geophys. Res.*, **101**: 26641-26668.
- Shepherd, T.R., W.D. Rust, and T.C. Marshall, 1996: Electric field and charges near 0°C in stratiform clouds. *Mon. Wea. Rev.*, **124**, 919-938.
- Simpson, G.C. 1909: On the electricity of rain and snow. *Proc. Roy. Soc. London*, **A83**, 392-404.
- Skamarock, W. C., M. L. Weisman, and J. B. Klemp, 1994: Three-dimensional evolution of simulated long-lived squall lines. *J. Atmos. Sci.*, **51**, 2563-2584.
- Smull, B.F., and R.A. Houze, Jr., 1985: A midlatitudes squall line with a trailing region of stratiform rain: Radar and satellite observations. *Mon. Wea. Rev.*, **113**, 117-133.

- Standler, R.B., and W.P. Winn, 1979: Effects of corona on electric fields beneath thunderstorms. *Quart. J. Roy. Meteor. Soc.*, **105**, 285-302.
- Steiner, M., R.A. Houze, and S.E. Yuter, 1995: Climatological characterization of three-dimensional storm structure from operational radar and rain gauge data. *J. Appl. Meteor.*, **34**, 1978 – 2007.
- Stolzenburg, M., T.C. Marshall, W.D. Rust, and B.F. Smull, 1994: Horizontal distribution of electrical and meteorological conditions across the stratiform region of a mesoscale convective system. *Mon. Wea. Rev.*, **122**, 1777-1797.
- , W.D. Rust, and T.C. Marshall, 1998a: Electrical structure in thunderstorm convective regions. 1. Mesoscale convective systems. *J. Geophys. Res.*, **103**, 14059-14078.
- , W.D. Rust, and T.C. Marshall, 1998b: Electrical structure in thunderstorm convective regions. 3. Synthesis. *J. Geophys. Res.*, **103**, 14097-14108.
- Takahashi, T., 1978: Riming electrification as a charge generation mechanism in thunderstorms. *J. Atmos. Sci.*, **35**, 1536-1548.
- Uijlenhoet, R., M. Steiner, and J.A. Smith, 2003: Variability of raindrop size distributions in a squall line and implications for radar rainfall estimation. *J. Hydrometeor.*, **4**, 43 – 61.
- Uman, M.A., 1987: *All about lightning*. Dover Publications, New York, NY, 167 pp.
- Vonnegut, B., 1963: Some facts and speculations concerning the origin and role of thunderstorm electricity. *Severe Local Storms, Meteor. Monogr.*, No. 27, Amer. Meteor. Soc., 224-241.
- Wacker, R.S., and R.E. Orville, 1999: Changes in measured lightning flash count and return stroke peak current after the 1994 U.S. National Lightning Detection Network upgrade; Part 1: Observations. *J. Geophys. Res.*, **104**, 2151 – 2157.
- Wallace, J.M., and P.V. Hobbs, 1977: *Atmospheric science, an introductory survey*. Academic Press Inc., San Diego, 467 pp.
- Weisman, M.L., and J.B. Klemp, 1982: The dependence of numerically simulated convective storms on vertical windshear and buoyancy. *Mon. Wea. Rev.*, **110**, 504-520.
- Williams, E.R., and R.M. Lhermitte, 1983: Radar tests of the precipitation hypothesis for thunderstorm electrification. *J. Geophys. Res.*, **88**, 10984 – 10992

- , M.E. Weber, and R.E. Orville, 1989: The relationship between lightning type and convective state of thunderclouds. *J. Geophys. Res.*, **94**, 13213-13220.
- , Zhang, R., and D.J. Boccippio, 1994: Microphysical growth state of ice particles and large-scale electrical structure of clouds, *J. Geophys. Res.*, **99**, 10787-10792.
- , 1995: Comment on "Thunderstorm electrification laboratory experiments and charging mechanisms." *J. Geophys. Res.*, **100**, 1503-1505.
- Wilson, C.T.R., 1929: Some thundercloud problems. *J. Franklin Inst.*, **208**, 1-12.
- Yuter, S.E., and R.A. Houze Jr., 1995: Three-dimensional kinematic and microphysical evolution of Florida cumulonimbus. Part II: Frequency distributions of vertical velocity, reflectivity, and differential reflectivity. *Mon. Wea. Rev.*, **123**, 1941-1963.
- Zipser, E.J., 1982: Use of a conceptual model of the life cycle of mesoscale convective systems to improve very-short-range forecasts. *Nowcasting*, Academic Press, New York, NY, 191-204.

VITA

Charles Lee Hodapp was born in San Angelo, Texas, to two wonderful parents, Chuck and Gayle Hodapp. He graduated from San Angelo Central High School in the spring of 2001 and entered Texas A&M University that fall. After four years of study, he graduated with a B.S. degree in meteorology in the spring of 2005. He spent the following two years working towards his M.S. degree, which he received in December 2007 in Atmospheric Sciences. His current address is:

3401 Tanglewood

San Angelo, TX 76904